Study Of Higher Moments Of Net-Electric Charge & Net-Proton Number Fluctuations In Pb+Pb Collisions At $\sqrt{s_{NN}}$=2.76 TeV In ALICE At LHC

Submitted in partial fulfillment of the requirements

of the degree of

Doctor of Philosophy

by

Nirbhay Kumar Behera

(Roll No. 08412901)

Supervisor

Prof. Basanta K. Nandi

Department of Physics

INDIAN INSTITUTE OF TECHNOLOGY, BOMBAY, INDIA

2014

Dedicated To

My Parents

Abstract

Lattice QCD predicts that at extreme temperature and energy density, QCD matter will undergo a phase transition from hadronic matter to partonic matter called as QGP. One of the fundamental goals of heavy ion collision experiments to map the QCD phase diagram as a function of temperature (T) and baryo-chemical potential (μ_B). There are many proposed experimental signatures of QGP and fluctuations study are regarded as sensitive tool for it. It is proposed that fluctuation of conserved quantities like net-charge and net-proton can be used to map the QCD phase diagram. The mean (μ), sigma (σ), skewness (S) and kurtosis (κ) of the distribution of net charge and net proton are believed to be sensitive probes in fluctuation analysis. It has been argued that critical phenomena are signaled with increase and divergence of correlation length. The dependence of n^{th} order higher moments (cumulants, c_n) with the correlation length ξ is as $c_n \sim \xi^{2.5n-3}$. At LHC energy, the phase transitoin is a crossover and the crossover transition line will appear close to the freeze-out line. The various order of cumulants of conserved quantities are also directly proportional to respective order of susceptibilities. So the higher moments analysis of fluctuations of conserved quantities like net charge and net baryon (proton) will allow to compare the experimental results directly with lattice QCD predictions. Moreover, recent theoretical developments suggest that the ratio of cumulants are useful to quantify the freeze-out parameters at LHC.

The data analysis is carried out using the Pb+Pb collisions at $\sqrt{s_{NN}}$ = 2.76TeV data of ALICE experiment of 2010 run at LHC. The analysis methodology and different methods of statistical error estimations are discussed. Toy model study is carried out to understand the behavior of higher moments results with detector and statistics effects. Various methods for detector efficiency correction for higher moments are discussed with the help of this toy model. The higher moments of net-charge and net-proton distributions are calculated and compared with HIJING and HIJING+GENAT results. The systematic uncertainties are estimated and the pseudorapidity dependence of net-charge and net-proton higher moments also studied. The baseline estimation from Poissonian and Negative Binomial Distributions are also compared with the data.

Keywords : QGP, QCD phase diagram, lattice QCD, Higher moments, Freeze-out parameters.

Thesis Approval

Thesis entitled **Study Of Higher Moments Of Net-Electric Charge & Net-Proton Number Fluctuations In Pb+Pb Collisions At $\sqrt{s_{NN}}$=2.76 TeV In ALICE At LHC** by **Nirbhay Kumar Behera** is approved for the degree of Doctor of Philosophy.

Examiners

(1)— — — — — — — — — — —

(2)— — — — — — — — — — — Ajit M. Srivastava

Supervisor

— — — — — — — — — — —

Chairman

— — — — — — — — — — —

Date : 14/01/2015

Place : IIT Bombay

ii

Declaration

I declare that this written submission represents my ideas in my own words and where others' ideas or words have been included, I have adequately cited and referenced the original sources. I also declare that I have adhered to all principles of academic honesty and integrity and have not misrepresented or fabricated or falsified any idea/data/fact/source in my submission. I understand that any violation of the above will be cause disciplinary action by the Institute and can also evoke penal action from the sources which have thus not been properly cited or from whom proper permission has not been taken when needed.

Nirbhay Kumar Behera

Nirbhay Kumar Behera

Roll No. 08412901

Date : 14/01/2015

Place : IIT Bombay

Contents

List of Figures

List of Tables

Chapter 1

Introduction

The beauty and complexity of Mother Nature has amazed human being. The twinkling stars, the deep sea, the rain, the biodiversity, everything around him, whatever he saw, a most fundamental question always disturbed him: ‘where are we all from?’ The sky touching rocky mountain, the singing fountain, the invisible soothing wind, the burning sun, the blue-green algae to the most intellectually developed primate: human, ‘what they are made up of?’ When he saw the blooming flower, the rising sun, the sprinkling cloud, the running river, he asked himself, ‘who governs them?’ From the very early time of human civilization, he has been searching the answers for his questions by unfolding the mystery of Nature. From the very tiny particle to the vast Cosmos, from the hardest to the deepest into the vacuum, he saw, he observed and he realized, may be we are all from a common singular point, made up of some **fundamental constituents** and are governed by some **fundamental forces**. Many civilizations came and went, this question must have been scratched by many ideas, grown up in many thoughts, but there was no such history of discovery of knowledge on fundamental forces or may have remained buried. Probably, Nature was so in details that she was in search of a mind where her every action will be treated as the formula for the fundamentals behind its complexity. The milestone of one revelation of secret of Nature was laid in the seventeenth century by a British mathematician, philosopher and physicist, Sir Isaac Newton (1642 - 1727). He was the first to discover one of the fundamental forces: **Gravitational force**. He was the first in seventeenth century to formulate the basics of Gravitational force in the language of mathematics postulating about the motion of objects and planets. His powerful postulation rules this macroscopic world; scientific community refers it as ‘Classical Physics’ or ‘Newtonian Physics’.

The ghost stone attracting small iron piece, the electric fish and the sparking thunder in sky gave birth to the thought to human being about new kinds of forces: electric and magnetic forces. The electric and magnetic phenomena had been realized even in B.C. and many philosophers had mentioned about them afterwards, but in eighteenth century, there were many scientist-philosophers who tried to understand about it in a different way rather than taking it as ‘ghostly’ phenomena. Laws for both Electricity and Magnetism were made by various scientists namely, Henry Cavendish, C.A. Coulomb, Alessandro Volta, Georg Simon Ohm and Micheal Faraday. James Clerk Maxwell (1831-1879) was also among them who explained both that electricity and magnetism are manifestation of one single force and termed it as **Electromagnetic force**.

But some unexplained and anomalies in Newtonian physics and classical Electromagnetic theories compelled the physicists to think beyond classical approach towards the understanding of Nature. In the beginning of twentieth century, Max Planck (1858-1947) made a revolutionized, breakthrough discovery, which is called as ‘Quantum Physics’. His interpretation of light (photon) as a discrete packet of energy (quantum) to explain the Blackbody radiation paved the way for countless discoveries in modern world. Albert Einstein (1879-1955), the ‘genius of the millennium’, related the mass with energy by famous $E=mc^2$ equation using his special theory of relativity. He also gave totally a new figure to Newtonian Gravitational force relating space, time and geometry, which is called as General Theory of Relativity (GTR). Erwin Schrödinger’s wave equation, Luis de Broglie’s theory of wave-particle duality and Werner Heisenberg’s uncertainty principle profounded the quantum mechanics. Dirac’s relativistic approach to Quantum mechanics made it a more powerful and complete theory. Relativistic quantum mechanics and Electromagnetic theory could successfully explain the interactions at microscopic or atomic level of any matter, about its phase and its dynamics also. In the mean time, fundamental particles like electron and proton were discovered in the late nineteenth century and early twentieth century. After discovery of neutron in 1932 by James Chadwick, electromagnetic theory failed to explain the composition of a nucleus. Soon after that, **Strong force** was postulated to explain the nuclear phenomena. This Strong force is responsible for binding protons and neutrons together into a nucleus, which were believed to be the building blocks of our material Universe. Enrico Fermi in 1933 put forward the theory of **Weak force** and proposed the existence of another fundamental particle, called ‘neutrino’, to explain energy spectrum of beta-decay. This weak force can explain the energy source of burning sun. Afterwards, many theoretical postulations and experimental findings by many great scientists have enriched our knowledge in understanding the fundamental forces and fundamental constituents of matters.

A brief history of discoveries of fundamental forces down the time is discussed. It is realized that the secret of Nature is encrypted in fundamental particles. With the help of powerful technologies, he probed into the smallest possible length scale and more and more fundamental laws of physics were digged out. Without going into the details, let us emphasize our introduction on fundamental forces and fundamental constituents: the most fundamental in nature and mother of all scientific discoveries. So far according to our knowledge, quarks and leptons are the most fundamental particles with no other substructure and four types of fundamental forces are governing the whole Universe obeying certain conservation laws. Whatever we see and whatever we even can’t see, but feel its presence, it may be matter or may be in the form of energy, can be classified under two fundamental groups of particles obeying certain laws of statistics. These are fermions and bosons. Fermions are particles with half-integral spin which follows Pauli’s exclusion principle and Fermi-Dirac statistics. Similarly, bosons are particles with integral spin which obey Bose-Einstein statistics. Any particle under any type of forces interact with each other by some intermediating particles, which are called as force carriers. And more interesting is that those force carriers are again fundamental particles or elementary particles. A thorough investigation of all the forces reflects that they are different from each other in terms of the ranges and their own characteristic ways of interactions among the particles. Meanwhile, speculation of unification of all forces among themselves has been done by saying that at a certain scale of energy or time, all the forces merge into a single one. James Clerk Maxwell, a Scottish physicist, was the first man who talked about the unification of electric and magnetic field and together called it as Electromagnetic force. Later in 1979, Abdus Salam, Sheldon Glashow and Steven Weinberg successfully unified Electromagnetic force to the Weak force and termed it as Electroweak force for which they were awarded the Nobel Prize. The unification theory of Electromagnetic, Weak and Strong interaction is known as Grand Unified Theory (GUT), which is not yet verified because of the complexity of the theory itself. The theory of unifying Gravity with other three forces is called as the **Theory of Everything**. Many theoretical works are going on and to test it we need also very high-energy scale called as Planck scale which is beyond the reach of today's technology. But this noble endeavor will be continued for the quest of knowledge. Detailed discussions about all four types of interactions are beyond the scope of this thesis. For the sake of completeness, a comparison of relative strength, their ranges and the force carriers of the four types of interactions are given in Table 1.1.

Table 1.1: Four fundamental forces: their force carriers, relative strength and range

Interaction	**Force carrier**	**Relative Strength**	**Range(m)**
Strong	Gluons	10^{38}	10^{-15}
Electromagnetic	Photon	10^{36}	∞
Weak	W and Z bosons	10^{25}	10^{-18}
Gravitation	Gravitons (not detected yet)	1	∞

Today, we have many theories on these topics, but the Standard Model of particle physics proposed by many scientists all over the world is the most well tested and established theory, which is discussed briefly in the following section.

1.1 Standard Model

Electromagnetic, Weak and Strong force all together are studied in a very comprehensive model known as **Standard Model**[1]. In Standard model, all particles and their interactions are classified in a very smart way. The studies are carried out using the language of mathematics and certain physics nomenclatures called as 'quantum numbers' like charge, spin, parity etc. and the theory is called as quantum field theory. The Standard model particles are shown in Figure 1.1. In Standard model, quarks and leptons are divided into three generations according to their hierarchy in mass. Leptons participate both in

Electromagnetic and Weak interactions and with exception, only neutrinos are weakly interacting particles. All charged particles can have Electromagnetic interactions. Up (u), charm (c) and top (t) quarks have +2/3 unit of charge, down (d), strange (s) and bottom (b) quarks have -1/3 unit of charge. Quarks can have all three types of interactions. Strong interaction is mediated by gluons and Electromagnetic interaction is mediated by photons. Both gluon and photon are massless, charge neutral, having unit spin. Weak interaction is mediated by $W^{\pm}$ and Z^0 which are massive and of spin one. Quarks and leptons are fermions and all the force carriers are bosons.

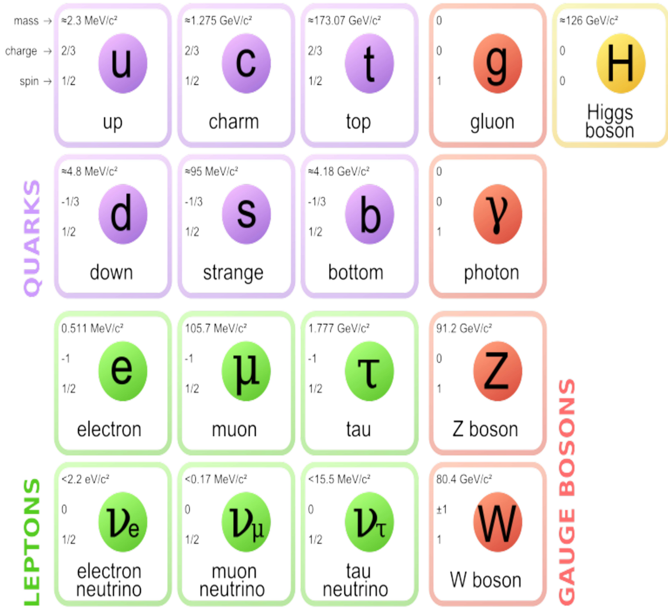

Figure 1.1: The Standard model of elementary particles with three generations of matter, the gauge bosons and the Higgs boson.

Standard Model incorporates another interesting phenomenon called as 'symmetry', which is also another fundamental property of Nature. The symmetry of all these three interactions implies that their Lagrangian is invariant under certain transformations. This is studied by gauge theory and the field is known as gauge field and the quantum of gauge field is called as gauge bosons: the force carriers. In the language of mathematics, Standard Model is a non-abelian gauge theory with $U(1)\times SU(2)\times SU(3)$ symmetry group with twelve gauge bosons (photon, three weak bosons and eight gluons). Symmetry of these groups implies that the gauge bosons should be massless. But after the discovery of W and Z bosons as massive in 1973, Higgs mechanism was adopted to explain about the origin of mass. Higgs mechanism and Higgs Boson were proposed in 1964 by Peter Higgs and five other scientist to overcome Goldstone's theorem limitation and to explain the non-zero mass of gauge bosons in spontaneous symmetry breaking. Then it was incorporated by Steven Weinberg and Abdus Salam in electro-weak unification. This was the one of the most essential theory to answer how the quarks and leptons got mass in Standard Model. According to Higgs mechanism, particle acquires mass from the interaction with Higgs field [2, 3]. Search for the existence of Higgs boson, famously known as 'God particle', was an essential need to validate or reject the Standard Model. With one of the main goal in search of the Higgs Boson, the most expensive experiment in particle physics to date, the Large hadron Collider (LHC) experiments were built and in March 2013, ATLAS (A Toroidal LHC ApparatuS) and CMS (Compact Muon Solenoid) confirmed the discovery of a Higgs boson like particle with mass 125.3$\pm$0.4(stat)$\pm$0.5(sys) GeV/c^2. For this great discovery, F. Englert and Peter Higgs were awarded the Nobel Prize in 2013. LHC experiments also do search and will verify many other extensions of Standard Model predictions, e.g. exotic particles, extra dimensions, supersymmetries and existence of dark matter and dark energy.

In the context of Standard model, all these three types of interactions are equally important. However, a special emphasis is put on Strong interaction keeping in mind its relevance with the work of this thesis and is discussed below.

1.1.1 Strong Interaction

The smallest unit of all matter is an atom and the nucleus at the center of the atom composed of protons and neutrons; gives 99.9999% mass of atom. Proton and neutrons are called as nucleons, are bound together by Strong force. Strong force is the strongest of all the forces, short range in nature and demands conservation of all quantum numbers. Strong force is important in making the building blocks of all matter. Nucleons are not the elementary particles. Inside the nucleons, there are also other sub-structures exist called as quarks and was confirmed in 1968 by deep inelastic scattering (DIS) experiment at Stanford Linear Accelerator (SLAC) [4]. Quark model was proposed by Murray Gell-mann and George Zweig with six flavours of quarks (up, down, strange, charm, top and bottom). After the discovery of particles, like Δ^{++} (uuu), Ω^{-} (sss), to explain its quark composition, another quantum number called as 'color charge' was assigned to the quarks. There are three types of color: red, green and blue. Like electric charge is the cause of electromagnetic interactions, here the color charge is responsible for Strong interaction. All hadrons are composed of quarks and divided into two groups: Baryons and Mesons. Baryons are made up of three quarks and mesons of two quarks called as valency quarks. Inside the nucleons, quarks are bound with each other by Strong force and gluons are the mediator of Strong force. Taking all combination of colors, there are eight types of gluons exist. Both quarks and gluons together called as partons. Theory of Strong interaction is known as Quantum Chromodynamics (QCD). Mathematically it is studied under a non-abelian SU(3) gauge group. The Strong interaction can be expressed by the QCD Lagrangian as follows.

$$\mathcal{L}_{\mathfrak{QCD}} = \bar{\psi}_i \left(i \left(\gamma^{\mu} D_{\mu} \right)_{ij} - m\delta_{ij} \right) \psi_j - \frac{1}{4} G^{a}_{\mu\nu} G^{\mu\nu}_{a} \tag{1.1}$$

where ψ is the space-time quark field, γ^{μ} is the Dirac matrices. $D_{\mu} = \partial_{\mu} + ieA_{\mu}$ is gauge covariant derivative. $G^{a}_{\mu\nu} = \partial_{\mu} A^{a}_{\mu} - \partial_{\nu} A^{a}_{\mu} + gf^{abc} A^{b}_{\mu} A^{c}_{\nu}$; represents the gauge invariant gluon field strength tensor with A^{a}_{μ} as the covariant four-potential of Strong force. The interaction strength among the partons is determined by strong coupling constant. The most interesting and peculiarity in the QCD coupling constant which is known as running coupling constant α_s is that, it is energy dependent. The expression for α_s is given below in the equation 1.2.

$$\alpha_s \left(Q^2 \right) = \frac{\alpha_s \left(\Lambda^2 \right)}{1 + \frac{\alpha_s(\Lambda^2)}{4\pi} \left(11 - \frac{2N_f}{3} \right) ln \frac{Q^2}{\Lambda^2}} \tag{1.2}$$

Here Q is the momentum exchanged, Λ is the QCD scale parameter and N_f is the number of flavours. The values of α_s calculated from QCD and measured in various experiments at different momentum range are given in Figure 1.2. From the Figure 1.2, it is clear that at very large momentum transfer or conversely at very short distance, the coupling strength decreases logarithmically. This implies that, at very high-energy regime, quarks and gluons will behave like free. This phenomenon is know as 'asymptotic freedom'. 'Asymptotic freedom' was discovered by Frank Wilczek, David Gross [5] and David

Politzer [6] in 1973 and for which they were awarded the Nobel prize in 2004. This fantastic idea changed the fate of the QCD theory. It was a very successful theory to explain many perturbative nature of QCD at high energy, e.g. (i) the evolution of parton distribution function at low Bjorken x, (ii) the production of jet in elementary collision, (iii) the properties of charmonium and bottomonium bound states. As we see, in the high momentum transfer region, perturbative QCD (pQCD) can be applied successfully to predict the phenomena. However, on the other hand, at low momentum transfer region, where $\alpha_s \sim 1$ ($Q^2 \sim 1$ GeV/c^2), the $\Lambda_{QCD}^{-1} \sim 1fm$; perturbative QCD (pQCD) can not be used to describe the hadronic spectrum because of highly non-linear nature of Strong force. This is the regime where quarks bind together to form hadrons [7]. To overcome this issue, Lattice-Gauge theory was proposed by K. Wilson in 1974.

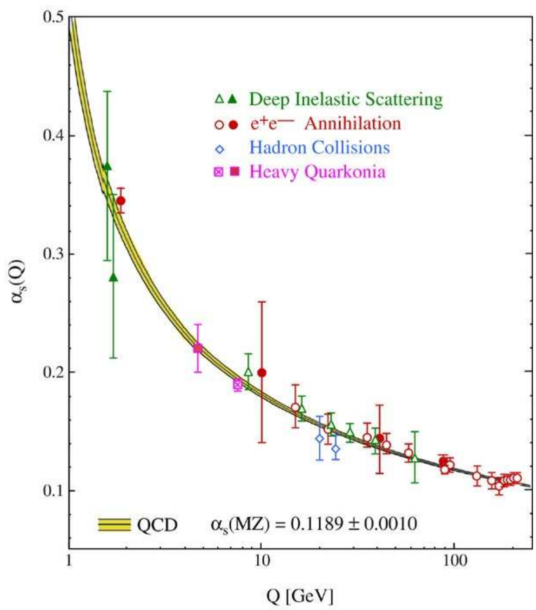

Figure 1.2: The summary of measurement of running coupling constant (α_s) as a function of respective scale of momentum transfer Q. Open and filled symbols are from NLO and NNLO QCD calculations, respectively. The curves are obtained from QCD predictions for the combined world average value of $\alpha_s(M_{z^0})$, in 4-loop approximation and using 3-loop threshold matching at the heavy quarks pole masses M_c = 1.5 GeV and M_b = 4.7 GeV. [8].

1.1.1.1 Lattice Gauge Theory

In the forbidden region of pQCD, there were many questions to be explained by QCD theory, like hadron masses, hadron structures and other nuclear properties. There were many effective models developed, but the Lattice Gauge theory was the most successful theory. It is commonly known as Lattice QCD which provides a non-perturbative tool to calculate the hadronic spectrum and to address the mechanism of confinement and chiral symmetry breaking and many others on a discretized Euclidean space time grid [9]. In lattice QCD, quarks are placed in the lattice site with finite lattice spacing "a" and are connected by the gauge fields (gluons). The advantage of lattice QCD formulation is that it can be regularized and renormalized by putting some finite value of "a", hence, ultra-violate divergence is avoided in the non-perturbative approach. As it involves many numerical computations using Monte Carlo methods, so it has limitation over choosing the value of "a". More smaller the value of "a", more the computational resources are needed and today this is done by super computers and results are extrapolated to a = 0. Lattice QCD can be solved numerically where strong coupling constant and the bare masses of quarks are the input parameters; which are again the most fundamental parameters in the theory of QCD. Hence, it should be emphasized that the predictions of lattice QCD became the most crucial demand to match the experimental findings to validate the theory of QCD, if it is a correct theory of Strong interaction at all.

Lattice QCD framework is based on Feynman's path integral approach to avoid the involvement of operators to make it possible for numerical simulation. As it uses the path integral formulation of quantum field theory, it enables to establish the connection with statistical mechanics. That is why, it can also explain the thermodynamics, equation of state and phase diagram of QCD matter in terms of state variables like temperature, energy density, entropy etc [10]. Temperature and baryo-chemical potential (μ_B) are used as control parameters to observe the response of other observables in Lattice QCD calculation to understand the phase diagram of QCD matter. There are many interesting results from lattice calculation on QCD matter at extreme conditions. One of the lattice QCD calculation predicts a spectacular transition of QCD matter at high temperature and vanishing μ_B [11] which is shown in Figure 1.3. In Figure 1.3, the variation of energy

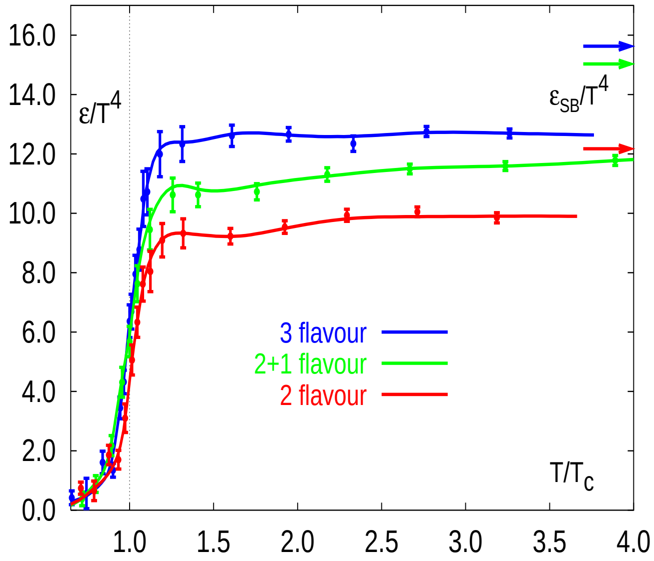

Figure 1.3: Variation of energy density as a function of temperature of hadronic matter at zero baryo-chemical potential from the lattice QCD calculation at finite temperature. Figure is taken from [11].

density (can be scaled with pressure also) with respect to temperature of QCD matter for different flavours is given. From Figure 1.3, it is observed that there is a strong and abrupt change of energy density (ϵ) from the low hadronic value to almost 80$\%$ of the ideal gas limit at a critical temperature T$_c$ and then saturates above the value of 2T$_c$. At the temperature T_c, the energy density below the ideal gas limit implies that there is still substantial interaction among the quarks and gluons in that phase. The change of energy density also depends on the number of flavours taken in lattice calculation. This is a clear indication of phase transition of hadronic colorless phase to a de-confined phase where quarks and gluons are basic degrees of freedom. This phase is known as Quark-Gluon Plasma (QGP) phase. The temperature and energy density corresponds to this de-confinement transition suggested from lattice QCD calculation is $\sim$170 MeV and 0.7 GeV/fm^3, respectively [11]. This QGP phase is treated as a noble state of matter because it is believed that Universe was at this phase of matter just after few micro-second of the Big-Bang and now at the core of neutron stars. Today, the prediction of lattice QCD and hence, the study of QGP keeps special importance to understand the early time evolution of universe and in search of fundamental properties of nature. A brief description of QGP, its experimental realization in connection to this thesis is discussed in next sections.

1.2 Quark-Gluon Plasma and Heavy-ion Collision Experiment

At extreme environment, like high temperature and (or) energy density, normal hadronic matter undergoes a phase transition to a plasma phase where the color singlet state dissociates, quarks and gluons are no longer confined inside bound state hadrons (de-confinement) and they become the basic degrees of freedom in this phase. This is the implication of theory of asymptotic freedom, which tells that, at sufficiently large momentum transfer and very small space-time intervals, the coupling strength becomes weak and quarks and gluons move asymptotically free. As pointed earlier, QGP is believed to be existed just after few micro-second of Big-Bang where the temperature was very high and at the core of neutron stars where the nuclear density is very high because of its strong gravitational pull. Therefore, study of QGP will shed some light on the theory of evolution of Universe like how the phase transition is resulted in relics of gravity waves, formation of nuclear matter and baryon density inhomogeneities in the cosmic fluid [12, 13]. To answer these questions, in late 1970, particle and nuclear physicist thought of heavy-ion collision experiment to recreate a situation in laboratory to study the QCD matter at extreme conditions. To meet this noble goal, collider experiments, like Super Proton Synchrotron (SPS) at CERN, Relativistic Heavy Ion Collision (RHIC) at BNL and Large Hadron Collider (LHC) at CERN, are built. In this collider experiments, heavy nuclei, like Au, Pb, are collided at relativistic energies to recreate the condition just after the Big Bang, known as little Big Bang or micro Big Bang (Note that all the conditions in heavy-ion collisions are not similar to the Big Bang).

Here is a carton shown in Figure 1.4 to understand the scenario of a typical heavy-ion collision. In Figure 1.4, two heavy nuclei are moving at relativistic speed, approaching towards each other, look like thin discs due to the Lorentz contraction in the center of mass frame. When they collide with each other, a large fraction of transverse energy is deposited in the reaction zone producing a very high energy density region and very

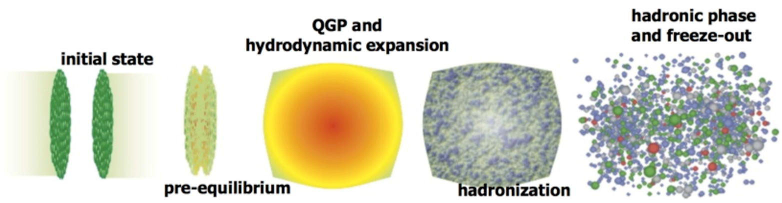

Figure 1.4: Various stages of a typical heavy-ion collision event. Figure is taken from [14].

high temperature [15]. The reaction zone is called as fireball and just after the collision the fireball expands and cools down to hadronize via the process of many types of particle production. During this brief time of creation and expansion of fireball, depending upon the energy of colliding system, the degree of interaction among the particles decides the faith of it, like, the life time, its bulk properties, the composition and spectra of produced particles. During the evolution of the fireball and the hadronization process, it comes across two freeze-out boundaries: chemical freeze-out and kinetic freeze-out. After chemical freeze-out, the inelastic scattering among the particles stops and there will be only elastic scattering. The particle numbers or the chemistry of the system is fixed after this. When system cross the kinetic freeze-out boundary, the mean free path of the particles is comparable to the system size, so the elastic scattering among the particles also stops, only particles are left as stable hadrons (proton, neutron, pion and kaon), photons and leptons (mostly muons and electrons). They come out as the end product of the reaction and hit the detector. Many sophisticated detectors are installed in these experiments to record the events to study the matter produced in the collision. The study is carried out through those end products where there is a chance of washout of the early stage information. So far there is no such smoking gun signature for the study of the QGP. However, there are some proposed theoretical signatures used to probe the QGP, which are potentially sensitive to the dynamics of QGP and can retain the memory of early stage even after the hadronization. Some of them are discussed below briefly with the recent experimental findings.

1.2.1 Jet Quenching and Parton Energy Loss

At large momentum transfer, hard scattering process among the partons produces two or more outgoing final state partons. They subsequently radiate gluons and (or) split into quark-antiquark pairs. Such process happens in a branching fashion and its probability can be described in a perturbative way by DGLAP equations [16–18]. At the end, those produced partons fragments in non-perturbative way to a set of collimated spray of hadrons called as jets. In heavy-ion collision, the production and propagation of jets are different than those in elementary collision because of the presence of hot and dense partonic medium. Bjorken first suggested that there would be a significant energy lose of the partons passing through the medium. Later more theoretical studies suggested that the partons will lose energy via gluon radiation [19]. The energy loss (ΔE) of the partons basically governed by two mechanisms: radiative and collisional, and can be expressed in a following empirical way [20, 21].

$$\Delta E \sim \alpha_s \times C_R \times \hat{q}(\rho_g) \times L^2 \tag{1.3}$$

where α_s is the strength of strong interaction, C_R is the color charge factor, $\hat{q}$ is the transport co-efficient which depends on the gluon density (ρ_g) of the QGP medium and L is the thickness of the medium. From equation 1.3, it is clear that gluons will lose more energy than quarks due to its color charge factor (QCD color Casimir factor of gluon C_A/C_F=9/4 times higher than quark). Heavy quarks will lose less energy in comparison to light quarks due to the dead-cone effect [22]. The consequences due to energy loss of the partons in the colored dense medium will be observed in the fragmentation of partons and results in the reduced production of hadrons. This phenomenon is known as jet quenching. Jet quenching is a final state effect and it can provide the information like opacity, diffusion constant and transport co-efficient of the medium produced in the collision. The first observation of jet quenching was reported in the di-hadron correlation study in the azimuthal plane at RHIC in Au+Au collision at $\sqrt{s_{NN}}$=200 GeV [23–26].

Figure 1.5 shows the results from p+p, d+Au and Au+Au collisions by STAR experiment [23]. The correlation is measured as a function of difference of azimuthal an-

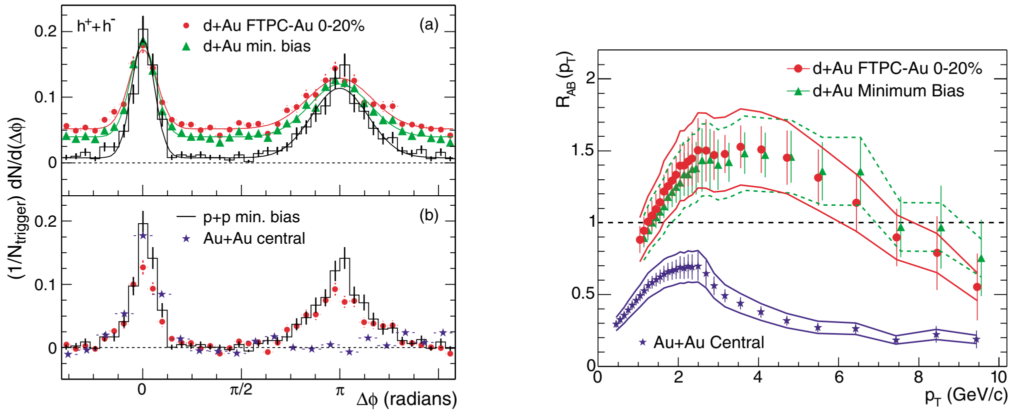

Figure 1.5: Left hand figure:(a) The two-particle azimuthal distributions for minimumbias and central d+Au collisions and for p+p collisions, (b) Comparison of two-particle azimuthal distributions for central d+Au collisions to p+p and central Au+Au collisions. Right hand side figure: Nuclear modification factor as a function of p_T for minimum bias and central d+Au collisions and central Au+Au collisions [23].

gle $\Delta\phi$ for a high p$_T$ trigger particles with respect to low p$_T$ associated particles where $\Delta\phi = \phi_{associated} - \phi_{trigger}$. Both in p+p and d+Au, the azimuthal correlations show a clear double peak, which represents a di-jet event. In Au+Au collisions data, one of the peaks is strongly suppressed. In an explicit way, one of the jet is fragmented outside the medium gives the near-side peak at $\Delta\phi = 0$ and the other one is passed through the medium, lost its energy and fragments into hadrons giving the heavily suppressed away-side peak at $\Delta\phi = 180^0$. This observation is in contrast to p+p collision where medium is absent and can be inferred in a simpler way in terms of nuclear modification factor. The nuclear modification factor (R_{AA}) is defined as,

$$R_{AA} = \frac{d^2N/dp_T d\eta}{T_{AA} d^2\sigma^{pp}/dp_T d\eta} \tag{1.4}$$

where $\frac{d^2N}{dp_T d\eta}$ is the differential yield per event in Au+Au collision, $T_{AA} = \frac{<N_{bin}>}{\sigma^{pp}_{inel}}$ describes the nuclear geometry of the collision and $\frac{d^2\sigma^{pp}}{dp_T d\eta}$ is the differential cross section in p+p. In the absence of medium effect, the value of R_{AA} should be 1. But the plot in the right panel of Figure 1.5, indicates a clear suppression of high p$_T$ hadrons in Au+Au data. This implies that the jet quenching is a final state effect and it is a clear indication of energy loss of hard-scattered partons due to interaction with a colored dense medium.

However, more experimental evidence is needed to confirm about the QGP formation. More studies are going on in this area at RHIC and LHC energies. Current results from LHC in Pb+Pb collisions at $\sqrt{s_{NN}}$ = 2.76 TeV show R_{AA} value around 50$\%$ less than the RHIC results in the range of p_T = 6-7 GeV/c. The rise of R_{AA} value at around $p_T = 8$ GeV/c is consistent with models. However, the magnitude of predicted slope varies from model to model [27].

1.2.2 Collective Flow

The medium produced in heavy-ion collision undergoes hydrodynamical expansion because of large pressure gradient created in the collision process. During this expansion, the constituents of the medium interact among themselves via the momentum transfer to achieve local thermal equilibrium. Particularly in non-central collision, when the impact parameter is non-zero, the spatial anisotropy in the reaction zone is converted into momentum anisotropy in the transverse momentum space after sufficient interaction among the partons and a collective flow is built up. There will be more pressure gradient along the minor axis than major axis and the reaction zone will attain symmetry during expansion. But the initial state information will be encrypted in the hadrons after freeze-out and will be reflected in the transverse momentum spectra of the produced particles. As the anisotropic flow is a self-quenching in nature, non-trivial results of it can be a unique tool to probe the early stage and hints about the degree of thermalization. Experimentally, it is measured by the transverse momentum distribution of particles with respect to reaction plane [28]. Reaction plane is defined as the plane spanned by the impact parameter and beam direction. The momentum anisotropy can be expressed by the Fourier expansion co-efficient of triple differential invariant distribution of produced particles as follows.

$$E\frac{d^3N}{d^3p} = \frac{1}{2\pi}\frac{d^2N}{p_T dp_T dy}[1 + 2\sum_n v_n cos[n(\phi - \Psi_n)]], n = 1, 2, 3, ... \tag{1.5}$$

where v_n are the flow harmonics and Ψ_n are the angle of the initial state spatial plane of symmetry. The first term of the right hand side of the equation measures the radial flow, which is isotropic in nature and it gives a blue shift in the transverse momentum spectra of the produced particles. The first term of the flow harmonics, v_1, and second harmonics, v_2, is referred as directed flow and elliptic flow, respectively. It is believed that, v_2 is sensitive to the early stage evolution, freeze-out conditions and equation of state (EoS) of the medium created [29]. Theoretically it can be connected with the shear viscosity to entropy ratio (η/s) using ADS/CFT correspondence [30] and can tell about the bulk properties of the medium. First evidence of collectivity was observed in heavy-ion collision experiments at AGS and SPS energies [31, 32]. Later the anisotropic flow measurements were done in more extensive ways with much higher energies at RHIC. STAR collaboration reported first results on various order of flow harmonics by measuring the anisotropy of azimuthal distribution of particles at $\sqrt{s_{NN}} = 200$ GeV in Au+Au collisions [33]. The most interesting finding of this measurement was the scaling of v_2 with the number of constituent quarks, which implies the partonic level of collectivity and possible formation of a QGP medium. The RHIC results on v_2 in comparison with different hydrodynamic and hybrid model signals a strongly interacting matter and appears to behave like an almost perfect fluid [34]. Now measurement of v_2 has drawn special attention at LHC energy. The energy dependence study of v_2 from RHIC to LHC shows an increasing trend suggesting that more hotter with longer life time partonic phase is created in Pb-Pb collision [35]. Because of higher multiplicity at LHC energy, the v_2 measurement at LHC energy will give more precision measurement of η/s to nail down the contribution from a partonic fluid. Other higher order harmonics, like v_3, v_4 and v_5, also can be used to put constraint on the theoretical models and will help for better understanding of the matter created.

1.2.3 Quarkonia Suppression

Suppression of heavy quarkonia as one of the signature of deconfinement was first proposed by Matsui and Satz in 1986 [36]. Quarkonia, like J/Ψ and Υ, are bound state of $c\bar{c}$ and $b\bar{b}$ pairs, respectively. A non-relativistic model for interaction potential for quarkonia spectrum in vacuum can be described by Cornell potential as follows.

$$V(r) = \sigma r - \frac{\alpha}{r} \tag{1.6}$$

where r is the inter-quark distance, σ is the string tension and α is a constant ($\sim$ 0.411). In the relativistic heavy-ion collision, because of the high energy density, light quarks anti-quarks are produced. In the mean time, $c\bar{c}$ and $b\bar{b}$ quark pairs are produced via gluon fusion process. So the interaction potential of quarkonia will be heavily affected and will be screened by the presence of other free color charges in the medium as the electromagnetic Debye screening happens in the plasma. Then a screening constant will arise in the potential and it is a function of temperature of the medium. If the bound state radius r_B ($r_B = \frac{1}{\alpha m_q}$, m_q is mass of the quark) is greater than the Debye screening distance, then the quarkonia states will melt down and inhibits the production. This phenomenon is called as quarkonia suppression. As r_B is dependent on the mass of the quarkonia mass, so the degree of suppression of various quarkonia states represents the thermometer for the medium. Experimentally, first anomalous J/Ψ suppression was observed in NA50 experiment at SPS [37]. Later in RHIC, detailed studies have been done on the formalism of nuclear modification factor by taking the invariant yield of Au+Au, d+Au collisions with respect to p+p collisions [38–40]. However, suppression of J/Ψ observed in d+Au collision which accounts for the cold nuclear matter (CNM) effects [41]. So it is difficult to interpret the J/Ψ suppression as the signal of QGP. There are many theoretical arguments suggest that there will be a J/Ψ enhancement because of recombination process in the hadronization stage at higher energy [42, 43]. Pb+Pb collisions data at LHC have already reported less suppression in comparison to SPS and RHIC. This provides a hint in favor of recombination process [44]. So, more precise measurement and theoretical understanding of the quarkonia production is needed for a definitive conclusion. Meanwhile, upcoming results from p+Pb collision at LHC, the J/Ψ and open charm elliptic flow will help to determine the degree of thermalization of the medium.

1.2.4 Chiral Symmetry Restoration

We know that chiral symmetry is a symmetry of QCD Lagrangian in vacuum (where m_q=0). But at low temperature and large distance ($\sim 1fm$), at non-zero or finite value of quark masses, chiral symmetry is broken, quarks are confined to form hadrons, and this is the phase of QCD where we live in. The basic observables of chiral properties of QCD is known as chiral condensate or quark condensate ($\langle\psi\bar{\psi}\rangle$) and for a spontaneously broken chiral symmetry, it has non-zero value. So in summary,

$$\langle\bar{\psi}\psi\rangle \begin{cases} = 0, & T > T_c, \\ > 0, & T < T_c. \end{cases} \tag{1.7}$$

where T_c is critical temperature for the phase transition and this transition is known as chiral phase transition [45]. The breaking of chiral symmetry because of non-zero quark masses can be understood with an example of phase transition of paramagnetism to ferromagnetism in the presence of external magnetic field as follows. In paramagnetic material, the spins are aligned in a random manner such way that the resultant spin is zero and hence the symmetry is maintained. But when external magnetic field is applied, all the spins are aligned along the direction of applied magnetic field. So the net spin will be nonzero, which is a case of ferromagnetism. Due to this preferential alignment, there is a breaking of symmetry of spin alignment. With an analogy to it, we can think of that chiral symmetry is broken because of non-zero quark masses.

Chiral phase transition has been studied in Lattice QCD and it suggests that at the limit of zero baryo-chemical potential and high temperature, hadronic matter will show a phase transition to de-confinement and chiral symmetry will be restored. In the de-confinement (QGP) phase, because of screening, the effective mass of the quark will be zero and chiral symmetry will be restored. But, there was a speculation that whether the de-confinement phase transition and chiral phase transition where chiral symmetry is restored, occur at same temperature?

To answer this, the behavior of Polyakov loop susceptibility (χ_L) and chiral susceptibility (χ_m) are studied as a function of coupling (β ~T) which is shown in Figure 1.6. Polyakov loop susceptibility is related to the de-confinement at pure gauge limit ($m_q \rightarrow \infty$) and chiral susceptibility is related to chiral symmetry breaking in the chiral limit ($m_q \rightarrow 0$). Interestingly, rapid change in the Polyakov loop order parameter ($\langle L\rangle$) and chiral order parameter ($\langle\psi\bar{\psi}\rangle$) are observed at a particular temperature. In other way, both the susceptibilities attain their maxima corresponding to the same critical temperature. Therefore, the de-confinement and chiral symmetry restoration will happen at

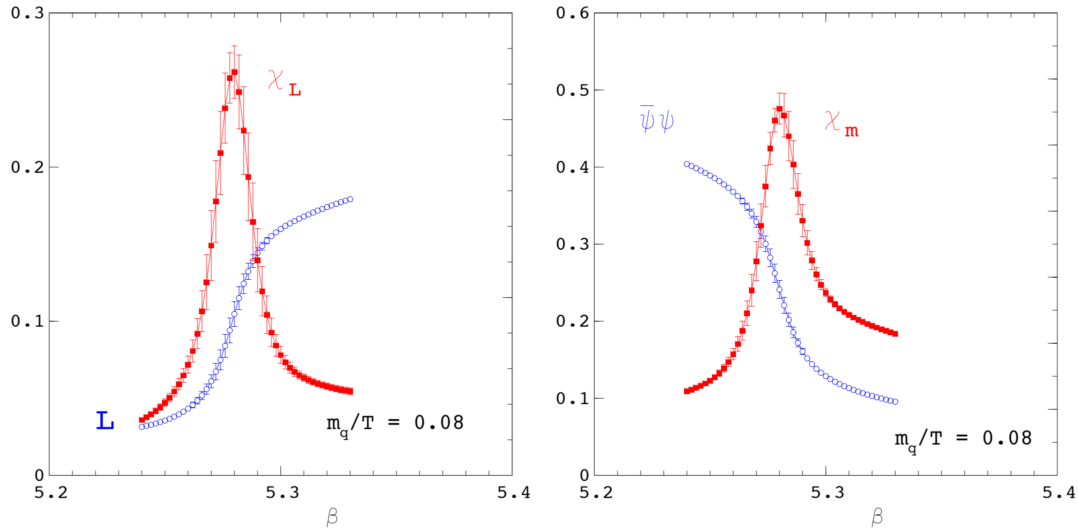

Figure 1.6: Deconfinement and chiral symmetry restoration in 2-flavour QCD: $\langle L\rangle$ is the order parameter for deconfinement in the pure gauge limit ($m \to \infty$) (left plot). $\langle\psi\bar{\psi}\rangle$ is the order parameter for chiral phase transition in the chiral limit ($m_q \to 0$) (right plot). The Polyakov susceptibility (χ_L) and chiral susceptibility (χ_m) are also shown in right and left figure, respectively as a function of coupling $\beta = 6/g^2$ [45].

same transition temperature. There are also many lattice calculations done at non-zero baryo-chemical potential to understand the phase diagram of QCD matter.

The physical observables of chiral symmetry restoration in the light meson spectrum are (i) formation of massive Goldstone bosons (pion, kaon) and (ii) degenerate state of scalar and pseudo-scalar, vector and axial vector meson [46]. Experimentally, it can be observed from the spectral function of ρ, ω and ϕ mesons. Many theories suggest that the masses of the ρ and a_1 meson may merge with mixing of their spectral functions and will show similar strength at both the masses, or there may be a smearing of spectral function over the entire range of mass. The mass shift and in-medium width modification of ρ meson can give a signature of chiral symmetry restoration. This can be done studying the di-lepton continuum [47]. This has been studied by CERES experiment at SPS energies and also has been continuing at RHIC and LHC energies. However, the thermal di-leptons are the main backgrounds for this study. So more model study is needed to interpret the data.

1.2.5 Correlation and Fluctuation

It is proposed that correlation and fluctuations are sensitive to the phase transition and to the thermodynamical properties of matter created [48–51]. One of the scientific breakthrough in the measurement of correlations and fluctuations of the cosmic microwave background radiation (CMBR) [52] carried out by COBE [53] and WMAP [54], which revealed the interesting correlations due to Big-Bang. The anisotropies in the temperature spectrum of WMAP experiment come from the quantum fluctuations during the epoch of very early inflation as described in the Big Bang model. In a similar fashion, heavy-ion collision experiment aims at the creation of little Big Bang in the laboratory and to study the phase transition of QGP to hadronic matter using correlations and fluctuation as a tool. Here some of the basics of the correlations and fluctuation measurements in heavy-ion collision experiments are discussed.

1.2.5.1 Correlation

Basically two types of correlations studies are done in heavy-ion collision experiments. One is, Fourier transformation of two particles Bose-Einstein correlation measurement in momentum space, which is used to determine the space-time structure of the fireball. This method is based on the Hanbury-Brown-Twiss (HBT) effect, which was used to determine the size of distant star. Although HBT effect arises after the freeze out of the strong interaction, but the measured correlation function contains the contribution from all the time during the fireball expansion. So one has to be careful about the collective behavior at partonic and hadronic level to interpret the result [55].

Similarly, second one is the di-hadron correlation of high p_T particles in pseudorapidity and azimuthal space. These are studied to address the in-medium modification of jet fragmentation function which is believed to be a direct manifestation of parton energy loss in the medium [56, 57]. This is called as jet-like correlation and the correlation function is defined with respect to azimuthal angle difference ($\Delta\phi = \phi_{trigger} - \phi_{associated}$) and pseudorapidity difference ($\Delta\eta = \eta_{trigger} - \eta_{associated}$) as follows.

$$C(\Delta\phi, \Delta\eta) = \frac{1}{N_{trig}} \frac{d^2 N_{associated}}{\Delta\phi \Delta\eta} \tag{1.8}$$

These types of di-hadron correlation results are studied in two ways: azimuthal correlation and pseudorapidity correlation. Quenching of the away side peak of azimuthal correlation is accounted for energy loss of the parton inside the medium and the away side broadening is interpreted as collective mode of medium in the form of a wake of lower energy gluons with Mach cone type angular emissions. Mach cone are created by a Mach shock of the supersonic recoiling parton traversing the medium and emission of secondary partons from the plasma in a preferential direction [58–60]. Similarly, the near-side "ridge" in pseudorapidity correlation is an indication of long range correlation and is a contribution from bulk matter, not from the jet fragmentation. However, still many debates are going on this to explain the origin of "ridge". Moreover, Ref [61] suggests that medium-modification of the parton shower can result in significant changes in the jet hadrochemistry. This can be observed via di-hadron correlation of identified particles. The ratio of yield of baryon to meson in between heavy-ion and p-p collision both in bulk and jet region counts for the radial flow and coalescence or recombination mechanism [62]. Recently, in ALICE, di-hadron correlation of proton and pions are studied and compared with PYTHIA. But no significant change is observed [63].

1.2.5.2 Fluctuation

Whenever we talk about fluctuation of a variable, it implies the deviation of its value from the mean value. Fluctuation can be statistical or dynamical. Due to finite number of particles, there will be always a statistical fluctuation in the medium. Dynamical fluctuations are related to the dynamics of the system. In heavy-ion collisions, there is a trivial fluctuation arises due to volume which directly depends on the number of particles. So fluctuation study of those variables are done which are volume independent. Event-by-event measurement of mean p_T fluctuations, particle ratio fluctuations and specially fluctuation of conserved quantities, like net-charge, net-baryon, can be unique signature of QGP [64, 65]. Recent result on net charge fluctuation measurements shows some deviation from hadron resonance gas and more towards the theoretically predicted QGP value [66]. Moreover, there are many theoretical predictions about higher moments of conserved quantities, like net-charge, net-baryon distributions which will signal the location of critical point in the QCD phase diagram [67]. The higher moments of the distribution of conserved quantities are directly related to the correlation lengths. So the higher moments will tell about the nature of the phase transitions and will help to quantify the freeze out parameters on the QCD freeze-out curves. In short, this is the motivation of doing higher moments of net-charge and net-baryon study in heavy ion collision. In the next section, a comprehensive introduction to higher moments of conserved quantities in connection to map the QCD phase diagram is given.

1.3 Higher moments of conserved quantities

In day-to-day life, we see matters transform from one phase to another, like melting of ice, an iron rod becomes magnet when a magnetic material placed nearer to it, etc. The response of matter with respect to applied external agents like temperature, pressure, magnetic fields are studied in terms of a diagram called as phase diagram. In a similar fashion, according to lattice QCD predictions, under extreme conditions, QCD matter exhibits its phase transition from colorless hadrons to a quark-gluon soup and the phase diagram of QCD is studied by temperature versus baryo-chemical potential. As it is discussed earlier, study of QCD matter always has been subject of interest, challenging and motivated for the quest of fundamental knowledge. Lattice QCD has predictions about the phase diagram and the nature of phase transition with respect to different quark flavours at zero as well as non-zero baryo-chemical potential. So first, let's have a tour on the QCD phase diagram and then a connection of higher moments of conserved quantities with it will be shown.

1.3.1 The QCD Phase Diagram

From the lattice QCD point of view, the QCD phase diagram can be understood in the following ways.

1.3.1.1 At vanishing baryo-chemical potential limit ($\mu_B = 0$):

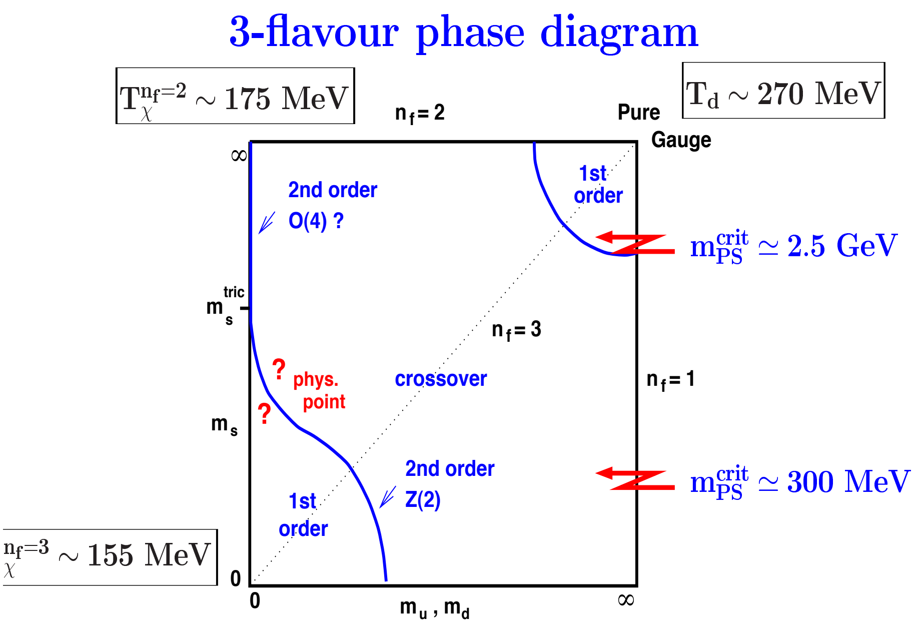

Figure 1.7: 3-flavour QCD phase diagram at $\mu_B = 0$ from lattice QCD calculations for degenerated u and d quark [45].

Lattice QCD is successfully implemented in study of the QCD at $\mu_B = 0$. At this limit, phase transition of QCD depends on number of quark flavours (n_f) and their masses. Then the most obvious question arises that at what temperature the transition occurs to the plasma phase and what is the nature of the phase transition. This can be answered in terms of global symmetry of QCD Lagrangian, which exists at either vanishing or infinite quark masses. A qualitative picture of QCD can be drawn on the basis of universality argument for the symmetry breaking in the heavy as well as light quark mass regime. As discussed in section 1.2.4, the transition temperature can be evaluated by lattice QCD both for heavy and as well as light quark mass limit using Polyakov limit and chiral condensate limit, respectively [45]. Remaining question is the order or nature of the phase transition. According to universality argument, the phase transition is of first order in the infinite quark mass limit. For the light quark mass limit, Pisarski and Wilczek formulation is used to find out the quark mass and number of flavour dependence on the order of phase transition [68]. According to it, the transition is of first order for $n_f \geq 3$ and is of second order for $n_f = 2$ which is shown in Figure 1.7. It is also evident from the figure that the transition temperature is decreasing with increase of n_f and chiral symmetry is restored in the vacuum above a critical numbers of flavours. The most interesting observation from this figure is that the occurrence of a second order phase transition line as a boundary of first order phase transition in the light quark mass regime. The transition on this line is controlled by an effective 3-dimensional theory with global Z(2) symmetry, which is not a symmetry of the QCD Lagrangian. Here neither Plyakov loop nor the chiral condensate will be the order parameter. That is why it is the most important for the critical or crossover behavior of QCD at realistic quark mass limit. According to Ref [45], the critical exponent, α, is positive for the 3-d Z(2) symmetry models, whereas it is negative for O(4) model. This will induce a large density fluctuation in the vicinity of chiral critical point. Therefore, it is important to determine the location of the physical point (the chiral critical point) in the QCD phase diagram.

1.3.1.2 At finite baryo-chemical potential limit ($\mu_B \neq 0$):

The finite temperature QCD phase diagram of the world we live in is of non-vanishing μ_B and with physical quark mass is more complicated and interesting. Figure 1.8 represents the QCD matter in a three dimensional plane of temperature, physical quark mass and μ_B [69]. As discussed earlier, at vanishing light quark mass, the QCD matter undergoes a phase transition corresponds to a temperature called as critical temperature (T_c) where chiral symmetry is restored. But for non-zero value of light quark masses, the chiral phase transition is a crossover transition and it is characterized by pseudo-critical temperature T_{pc}. Meanwhile, for non-vanishing quark mass, the first order transition ending at the vanishing quark mass in T_{tri} will end at a point called as critical point (CP) corresponds to temperature T_{cp} and chemical potential μ_{cp} [69]. A lattice simulation with 2+1 flavours by Ref [71] has given some evidence of existence of this CP in T-μ_B plane. Moreover, in Ref [71] it is argued that CP has much richer structure instead of point like.

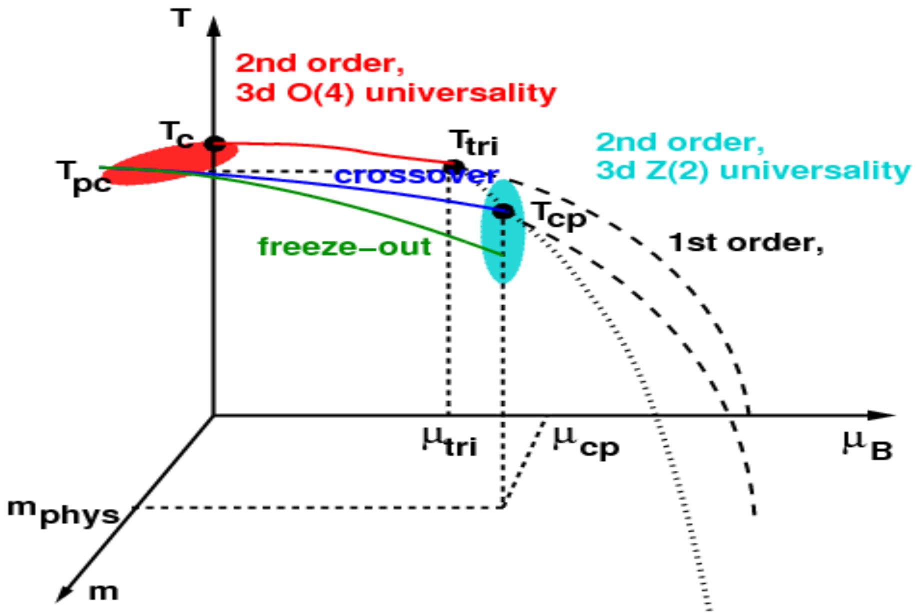

Figure 1.8: Three dimensional QCD phase diagram in the temperature, baryo-chemical potential and physical quark mass space [69, 70].

There is another line in Figure 1.8 which is called as the chemical freeze-out line. In heavy-ion collision experiment, it is characterized by the temperature and μ_B at which the expanding fireball forms hadrons. This is a parameterized line obtained by comparing particle ratios of hadrons with hadron resonance gas (HRG) model. It is seen that, for small value of μ_B, the freeze-out temperature and T_{pc} with physical light quark masses are more close to each other and the difference increases with increasing value of μ_B. In Ref [69], it is suggested that the freeze-out curve will remain close enough to the QCD critical point at T_{cp} which is yet to be established.

Figure 1.9 is the theoretically sketched most simpler and widely accepted QCD phase diagram in T-μ_B plane. It represents phases of QCD matter at different μ_B and T. As can be seen, a first order phase transition line separates the QGP phase and hadron gas phase and prediction of presence of critical point at the end of first order phase diagram. At very high temperature and very small μ_B, there will be crossover. Similarly, at very high μ_B and low temperature, there will be QGP phase which is believed to be the conditions at the core of neutron stars where color superconductivity may arise. Like critical point in other phase diagram in most common condensed matter, locating this CP in QCD phase diagram is interesting and challenging too. Lattice QCD has been used to study

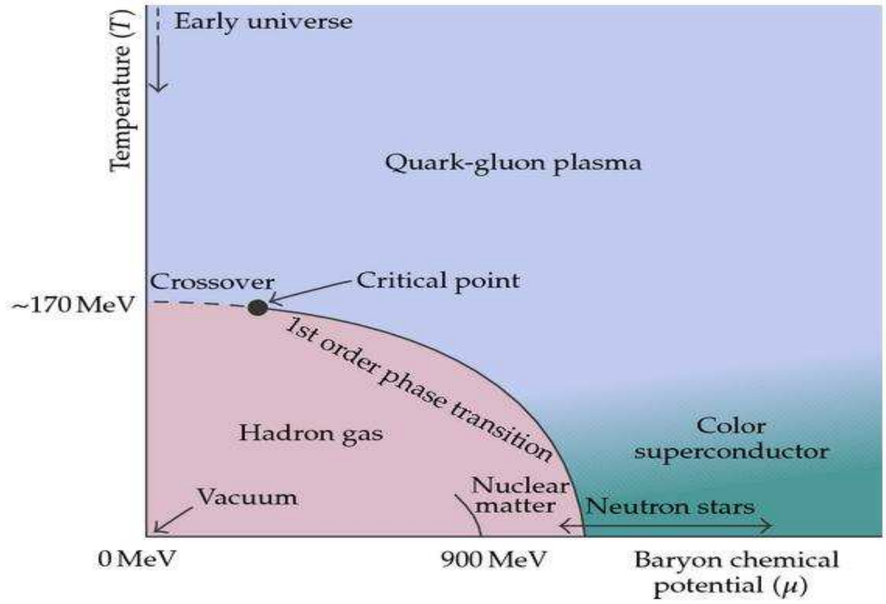

Figure 1.9: QCD phase diagram [72].

the phase diagram extensively at finite T with $\mu_B = 0$. However, at $\mu_B > 0$, because of severe fermion sign problem, study of QCD phase transition is prohibited in lattice QCD. There are many efforts tried to deal with this sign problem, Taylor expansion in μ_B is one of the method to circumvent this sign problem [73–75]. By this method, various order of derivatives of pressure are calculated at $\mu_B = 0$ and plugged into the Taylor series expansion. These derivatives are defined as quark number susceptibilities

$$\chi_q^n = \frac{\partial^n [p(T, \mu)/T^4]}{\partial(\mu_q/T)^n} \tag{1.9}$$

The divergence of quark number susceptibilities as a function of temperature will signal about the critical behavior on the QCD phase diagram. However, there are certain limitation and theoretical complication in this type of lattice simulation. So, how this gap can be overcome by the experimental measurements is discussed in the next section.

1.3.2 Higher Moments of Conserved Quantities As a Probe for QCD Phase Transition and Freeze-out Condition In Heavy-ion Collisions

In this course of discussion, there are two most fundamental questions to be answered on the QCD phase diagram, which are given below:
(1) The co-ordinate of the critical point (CP) in the T-μ_B plane.
(2) Determination of freeze-out parameters in the vicinity of chiral cross-over transition line.

Beyond certain limitation of lattice QCD calculation, according to theoretical suggestions, the common answer to the above questions can be drawn by fluctuation analysis of conserved quantities, like net-charge, net-baryon and net-strangeness. It is argued that, in the vicinity of critical point, various thermodynamical quantities will show large fluctuations and divergence in the correlation length. The higher moments of the multiplicity distributions of conserved quantities are directly related to the correlation length (ξ). The variance (σ^2), the second order central moment, varies with ξ as $\sigma^2 \sim \xi$. The skewness (S), which is the ratio of third order central moment to cube of σ, varies with ξ as S $\sim \xi^{4.5}$. Similarly, kurtosis (κ), is the ratio of fourth order to square of second order of central moments, varies with ξ as $\kappa\xi^7$. As the higher moments and their products have larger dependence on ξ, that is why, they are treated as most sensitive tool to locate the QCD critical point. In heavy-ion collision experiment, the measurement of higher moments of net-charge and net-protons can be used to determine the critical point. This can be done by varying collision energy ($\sqrt{s_{NN}}$) to scan the QCD phase diagram. The non-monotonic behavior of the higher order moments with respect to $\sqrt{s_{NN}}$ will signal the location of critical point. First experimental results on net-proton higher moments at RHIC did not see any indication of CP by their measurements based on three different energies: 19.6 GeV, 62.4 GeV and 200 GeV. However, they don't rule out the possibility of existence of CP for the entire region in QCD phase diagram of μ_B below 200 GeV [76]. The search for QCD critical point is going on by RHIC beam energy scan (BES) program to investigate the range of μ_B from 100 MeV to 550 MeV using this higher moments analysis of conserved numbers, like net-charge, net-baryon (net-proton) and net-strangeness (net-kaon).

On the other hand, the determination of freeze-out parameters is also important to localize the freeze-out boundary in the QCD phase diagram. In heavy-ion collision experiments, the temperature and baryo-chemical potential at which chemical freeze-out occurs are called as freeze-out parameters (T$_f$ and μ_B^f) [77]. The determination of this freeze-out parameters are done by measuring the particle yield ratios and then comparing with them with thermal statistical model like Hadron Resonance Gas (HRG) model. This HRG models are very successful in describing the QCD thermodynamics in the hadronic phase [78, 79]. In this model, they use the thermal parameters T$_f$ and μ_B^f which corresponds to the last interaction of the hadrons participating in the collective expansion and cooling of the hot and dense medium. It is observed that, at $\mu_B = 0$ and physical quark mass value, the chemical freeze-out seems to occur at very near to the QCD transition region. But at larger values of μ_B/T, some discrepancy between the slope of the freeze-out curve and current lattice QCD results is observed on the chiral phase transition line. The limitation of HRG model is that neither it exhibits any critical behavior nor it accounts for the sudden change of the degrees of freedom during the transition of hadronic to partonic phase. This can be accomplished by experimental measurements of higher order moments or cumulants (in chapter 3, a detail discussion on moments, cumulants and their relationships are discussed) of net-charge and net-proton number fluctuations at RHIC and LHC. At top RHIC energy and at LHC energy, we are at the chiral limit, where the μ_B value is very small. It is the crossover region in the QCD phase diagram as shown in Figure 1.8. According to Ref. [80], the chiral crossover transition line will appear close to the freeze-out line. It is proposed that there will be non-trivial behavior of higher order cumulants of net-charge and net-baryon multiplicity distributions, which will appear because of O(4) criticality. In lattice QCD, the observation is made through the various order of quark number susceptibility (χ_q^n) which can be directly connected to the respective order of cumulants of the probability distribution of net-charge and net-baryon. The sign change and ratio of those cumulants are suggested as sensitive probe for the critical behavior and rapid change of degrees of freedom. According to Ref [80], “If freeze-out occurs close to

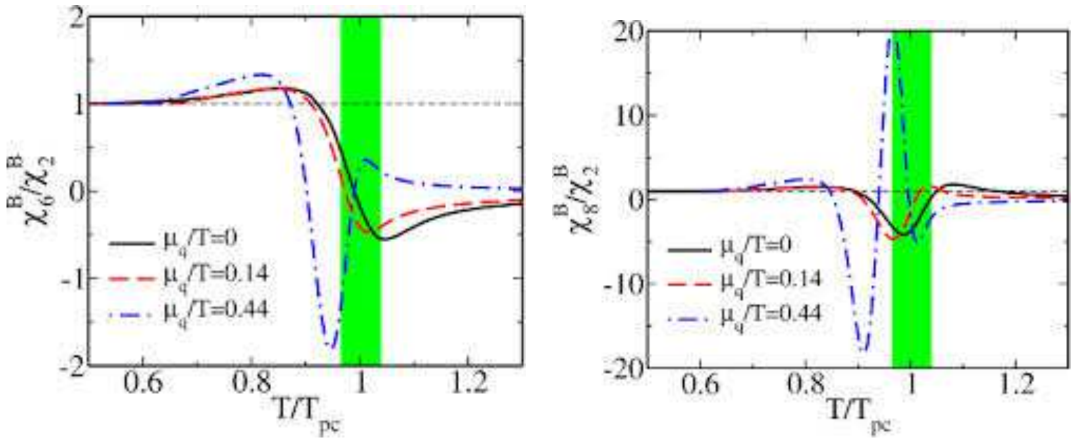

Figure 1.10: Temperature dependence of ratio χ_8^B/χ_2^B (right) and χ_6^B/χ_2^B (left figure) are calculated for different μ_B/T corresponding to values at chemical freeze-out in heavy ion collisions in the Polyakov loop extended quark meson (PQM) model with functional renormalization group (FRG) approach. The shaded area indicates the region of the chiral crossover transition at $\mu_B/T = 0$ [80].

the chiral crossover temperature the sixth order cumulant of the net baryon number fluctuations will be negative at LHC energies as well as for RHIC beam energies $\sqrt{s_{NN}} \gtrsim$ 62.4 GeV, corresponding to $\mu_B/T \lesssim 0.5$. This is in contrast to hadron resonance gas model calculations which yields a positive sixth order cumulant”. It means, the 6^{th} order cumulant of net-baryon will be negative in the vicinity of pseudo-critical temperature for chiral symmetry restoration and ratio of sixth to second order cumulants of net-baryon (χ_B^6/χ_B^2) will be negative for freeze-out at LHC and RHIC high energy runs.

Table 1.2: Freeze-out conditions obtained from ratio of various order cumulants of net-charge and net-baryon for the case that freeze-out appears well in the hadronic phase (third row) or in the vicinity of chiral crossover temperature T_{pc} (fourth row) using lattice QCD calculation. Second row gives the result from HRG model calculations [80].

Freeze-out conditions	χ_4^B/χ_2^B	χ_6^B/χ_2^B	χ_4^Q/χ_2^Q	χ_6^Q/χ_2^Q
HRG	1	1	~ 2	~ 10
QCD:$T^{freeze-out}/T_{pc} \le 0.9$	≥ 1	≥ 1	≥ 2	~ 10
QCD:$T^{freeze-out}/T_{pc} \simeq 1$	~ 0.5	< 0	~ 1	< 0

Figure 1.10 shows the temperature dependence of ratio of higher order cumulants calculated at different μ_B/T corresponding to values at chemical freeze-out in heavy-ion

collisions at RHIC. Moreover, it also predicts about the freeze-out conditions in comparison to HRG model and lattice using the ratio of cumulants which is given in Table 1.2.

In addition to this, ratio of cumulants can be used to determine the freeze-out parameters which are as follows [81].

- **Even-odd ratios of cumulants are good observables to determine the value of the baryon chemical potential at freeze-out.**
- **Even-even ratio of cumulants especially of the net-charge will allow to determine the freeze-out temperature.**

From the above discussion, here is the summary of the key motivation for measuring the higher moments of net-charge and net-proton multiplicity distribution at LHC. The higher order moments of conserved quantities, like net-charge and net-baryon multiplicity distribution, can be directly connected with various quark number susceptibilities, which allows the comparison of lattice QCD results directly with experiemntal measurements. At LHC energy, where there is a prediction of crossover, the freeze-out curve will be close to the chiral phase transition. Thus, freeze-out parameters can be determined independent of any model by taking the ratio of higher order cumulant of conserved number fluctuations and their sign will reflect about the chiral crossover transition which will allow to map the QCD phase transition and freeze-out curve at LHC energy.

1.4 Scope and organisation of thesis

The main motivation of the work in this thesis is to measure the higher moments of net-charge and net-proton number fluctuations in Pb+Pb collision data of ALICE at LHC. This study will help to explore the QCD phase diagram at very high temperature and small μ_B, which will allow to compare the experimental findings with the lattice QCD predictions and determination of freeze-out parameters in model independent way.

This thesis is organized as follows. In Chapter 2, a brief introduction to LHC experiment, ALICE detector, the online and offline analysis framework of ALICE are discussed.

In Chapter 3, an introduction to higher moments is given and its connection to lattice QCD observables is drawn. Meanwhile, a brief description about lattice QCD, hadron resonance gas model and baseline methods are discussed. Then the analysis methodology of higher moments, like centrality bin-width correction, central limit theorem, statistical error estimation, are discussed. Chapter 4 is devoted to simulation study to understand the dependence of higher moments results on event statistics, detector effects and contamination. Then two methods on efficiency correction for higher moments are discussed using toy model. The analysis results are presented in Chapter 5. In this chapter, the event selection, track selection, higher moments measurement and comparison of the results with HIJING are discussed. Then net-charge and net-proton higher moments, the systematic error estimation and comparison of data with baseline values are done. At the end the evolution of higher moments results with pseudorapidity coverage is discussed. In Chapter 6, a summary of the analysis and outlook for future study are described.

Chapter 2

Experimental Facilities

"In the matter of physics, the first lessons should contain nothing but what is experimental and interesting to see. A pretty experiment is in itself often more valuable than twenty formulae extracted from our minds." -Albert Einstein

In late sixty of twentieth century, European Organization for Nuclear Research (CERN) was established after eminent Noble laureate Louis de Broglie put the first official proposal for it [82]. It started its first run in 1957 with the first 900 MeV SynchroCyclotron (SC), a begin of new era, an endeavor in experimental nuclear and particle physics. It was a leap of human mankind to a new world of knowledge towards the search of basic fundamental laws of Universe. Thereafter, its journey still continues not only limited for basic science but also all kind of services to mankind starting from medical science to information technology. Today, CERN stands at the edge of the most advanced technology the modern world has. It is one of the mega science projects and the biggest collider experiment all over the world.

2.1 The Large Hadron Collider

In December 1994, CERN council released its approval for the Large Hadron Collider (LHC) and decided to convert and reuse the Large Electron-Positron (LEP) tunnel for LHC experiment[83]. The LHC tunnel of circumference 26.7 km is situated 170 meter under the ground of French-Swiss border near Geneva. Inside the tunnel, there are two separate beam pipes surrounded by superconducting dipole magnets operating below 2K and are enclosed in a single cryogenic system(vessel) by "twin-bored" design [84]. Dipole magnets, which are used to bend the beam can provide a maximum of 8.33T of magnetic field. There are total 1232 numbers of dipole magnets with several quadrupoles and sextupole-dipole corrector magnets made up of NbTi superconducting coil accommodated inside the LHC tunnel. Superfluid helium is used to keep all the magnets below 2K for smooth operation at such high magnetic field. RF cavities are also used to accelerate, to keep beam focused and to compensate synchrotron radiation loss of the accelerating beam. A cross-sectional view of cryo-dipole containing two beam pipes, superconducting coil and other accessories with support structures is shown in Figure 2.1.

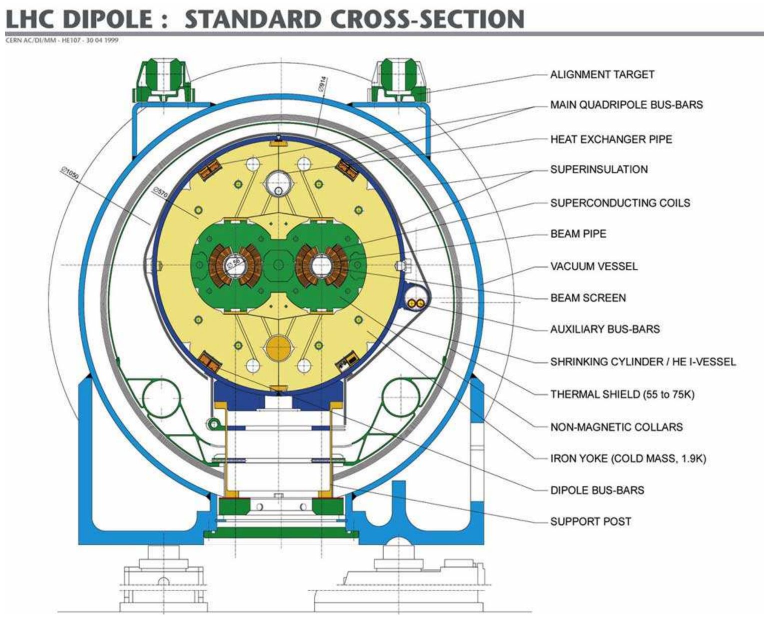

Figure 2.1: Cross section of LHC dipole with its support structures [83].

With the present setup, LHC is capable of colliding both proton beam as well as ion beam (Pb^{82+}) at maximum center of mass energy 7 TeV and 2.76 TeV, respectively. The schematic view of LHC ring and CERN facilities for beam production to beam injection is shown in Figure 2.2. Injection procedures for proton beam and Pb ion beam to the main LHC ring involve multi-stage process, which are discussed herewith.

Proton beams are produced by stripping hydrogen atoms at Linear Accelerator (LINAC -2) and then injected to BOOSTER. BOOSTER injects the beam to Proton Synchrotron

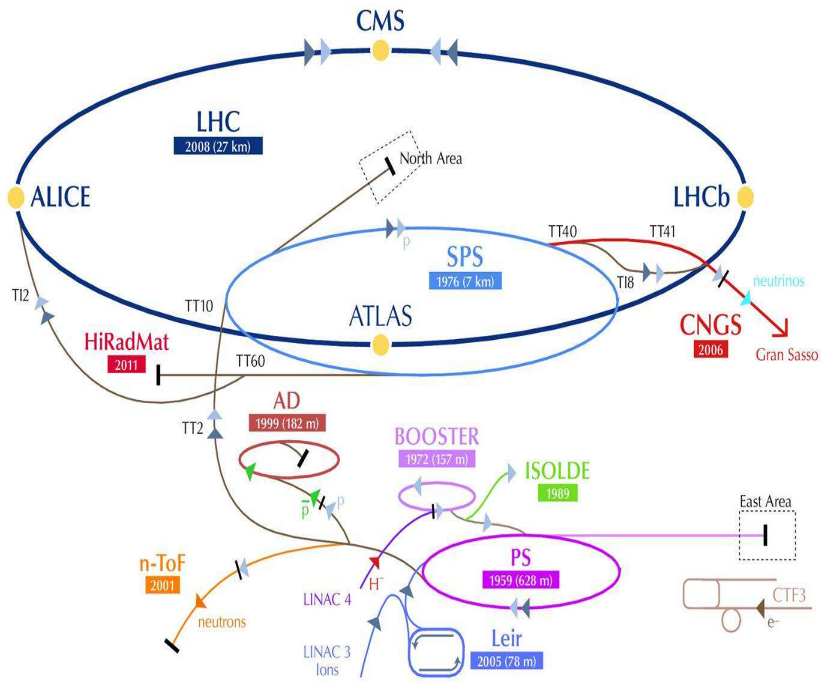

Figure 2.2: The LHC complex at CERN.

(PS) and then PS to Super Proton Synchrotron (SPS). In SPS ring, they are accelerated up to 450 GeV and then injected to main LHC ring for a 7 TeV p+p collisions where they are further accelerated to 99.999$\%$ of speed of light. Each proton beam has 2808 bunches with bunch spacing 25 ns and each bunch consists of 1.15×10^{11} protons to provide a nominal luminosity of $10^{34} cm^{-2} s^{-1}$ [83].

Producing Pb ions are little bit complex than proton beam. The Pb atoms are produced by vaporizing pure lead sample when it is heated up to 550^{0}C. After that lead vapor is initially ionized by passing electrical current. Now these ions are accelerated in LINAC 3 and then passed through carbon foil for further stripping of electrons to make Pb^{54+}. After it, they follow the same path as the proton beam. Before injecting to PS, Pb^{54+} are accelerated to 72 MeV per nucleon in Low Energy Ion Ring (LIER). In the PS ring, final stripping of electrons are done to make Pb^{82+} and again accelerated to 5.9 GeV per nucleon. SPS accelerates the beams to 177 GeV per nucleon before injecting to the LHC ring. In Pb beam, there are 592 bunches with each bunch consisting of 7.0×10^{7} ions to give a nominal luminosity $1.0 \times 10^{27} cm^{-2} s^{-1}$ [83].

The beams from SPS are injected and circulated clock-wise and counter clock-wise in the LHC ring. The circulating beams are made to collide at 4 main interaction points. At each interaction point, depending upon the physics goal, detector facilities are established to record the collision data. A Toroidal LHC ApparatuS (ATLAS) and Compact Muon Solenoid (CMS) are two high luminosity experiments situated diametrically opposite in LHC ring at Point 1 and Point 5, respectively. They are mostly designed for p+p collision to address the standard model predictions: the Higgs Boson. Apart from Higgs Boson search, they also look for physics beyond Standard Model like Super-symmetry (SUSY) particle and extra dimensions. However, ATLAS and CMS are also capable of taking Pb+Pb collision data. Large Hadron Collider beauty (LHCb) experiment is built at Point 8, which takes data only during p+p collisions. This is a small dedicated experiment to deal with matter anti-matter puzzle in the Universe. A Large Ion Collider Experiment (ALICE) is located at Point 2. ALICE can take data both for p+p and Pb+Pb collisions. It is a dedicated experiment for Pb ion collisions to study matter which is believed to have existed after one micro-second of Big Bang: the Quark-Gluon Plasma. The design and purpose of ALICE detector and its sub-detectors are described in the next section.

2.2 A Large Ion Collider Experiment (ALICE)

Towards the end of 1990, the idea of making a general purpose heavy-ion detector was conceived in a workshop sponsored by ECFA [85]. The dream of building ALICE came into a reality when it was approved in 1997. Today what we see the ALICE detector is a contribution from its collaborators counting over 1000 physicists and engineers from 105 institutes in 30 countries across the world. ALICE experimental facilities are setup inside the old L3 LEP cavern. Although ALICE is a slower detector in comparison to ATLAS and CMS, it is optimized for high multiplicity environment. It is also well known for its versatility among all LHC experiments. It can be operated for p+p, p+Pb and Pb+Pb collisions to cover a wide range of physics topics. It has excellent tracking and particle identification (PID) capabilities over a wide range of momenta to address both soft and high p_T physics (e.g. jet physics). ALICE has total 18 sub-detectors assembled in central barrel part and in the forward region; together accounts overall dimensions $16 \times 16 \times 26$

m^3 and weight of approximately 10,000 tons [86]. In Figure 2.3, various sub-detectors in ALICE are shown.

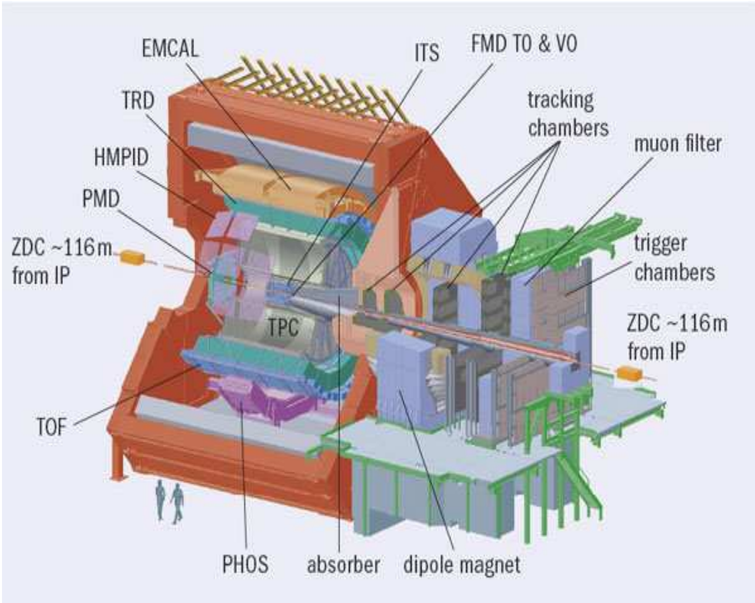

Figure 2.3: Schematic view of ALICE detector.

In this section, the descriptions of various sub-detectors are given by grouping them in central region and then the forward region according to their position in ALICE.

2.2.1 The Central Barrel

The central barrel extends from -0.9 to 0.9 in pseudorapidity with full azimuthal coverage covering polar angles from 45^0 to 135^0. It consists of Inner Tracking System (ITS), Time Projection Chamber (TPC), arrays of Time Of Flight (TOF), Ring Imaging Cherenkov (HMPID), Transition Radiation detector (TRD), Photon Spectrometer (PHOS) and Electromagnetic Calorimeter (EMCAL). All detectors have full azimuthal coverage around the beam pipe except HMPID, PHOS and EMCAL. The design and primary physics objectives of each detector will be discussed according to their geometrical position starting from interaction point in radially outward direction.

2.2.1.1 Inner Tracking System (ITS)

ITS is also known as vertex detector and is comprised of 6 cylindrical layers formed by 3 groups of silicon detectors having 2 layers each located in between 4 cm to 43 cm covering rapidity range of $|\eta| < 0.9$. Only the first layer is extended up to $|\eta| < 1.98$ together with the Forward Multiplicity Detectors (FMD) for continuous measurement of charged-particle multiplicity. ITS has relative momentum resolution better than 2% for pions within the transverse momentum 100 MeV/c to 3 GeV/c [87]. It can detect simultaneously more than 15,000 tracks having spatial resolution of the order of few tens of μm.

The two innermost layers are called Silicon Pixel Detector (SPD). It is made up of hybrid silicon pixels consisting of two-dimensional matrix of silicon detectors diodes operating in reverse-biased mode. Its readout chips are mixed signal ASIC developed in an IBM 0.25 μm CMOS processor having high radiation-tolerant design. It is used for the determination of position of primary vertex and measurement of impact parameter of secondary tracks coming from weakly decaying particles, like strange baryons (Λ, Ξ and Ω) and D-mesons. SPD is relatively radiation hard and can handle track density as high as 50 tracks/cm^2. SPD has the best spatial resolution which is 12 μm.

The two intermediate layers of the ITS are called Silicon Drift Detectors (SDD) made up of 300 μm homogenous high-resistivity Neutron Transmutation Doped (NTD) silicon. Three types of ASICs, namely PASCAL, AMBRA and CARLOS, are used in its front-end electronics. Its working principle is like a gaseous drift chamber. When a charged particle passes through it, it creates electron-hole pairs. The drifting electrons are collected by the readouts and from the drifting time, its spatial position is determined. SDD has spatial precision of 35 μm. It also provides energy-loss information which is used for particle identification.

The two outermost layers of ITS are made from double sided Silicon Strip Detectors (SSD). The detection module consists of one sensor of 300 μm thick each. SSD provides two-dimensional measurement of track position with spatial precision 20 μm and is crucial for matching the TPC tracks with ITS. Both SDD and SSD have analog readout to provide dE/dx measurement for which ITS can identify the low momentum particles [86].

2.2.1.2 Time Projection Chamber (TPC)

TPC is the main tracking device in the central barrel region and also known as the heart of the ALICE detector system [88]. It has full azimuthal coverage and with pseudorapidity coverage from $|\eta| < 0.9$. TPC is designed with a cylindrical shape surrounding the ITS. The longitudinal length of TPC is 5 m and its inner and outer radii are 0.85 m and 2.5 m, respectively. It is a gaseous detector of volume 90 m^3 filled with mixture of Ne, CO_2 and N_2 in 90:10:5 proportions. The schematic view of TPC is shown in Figure 2.4.

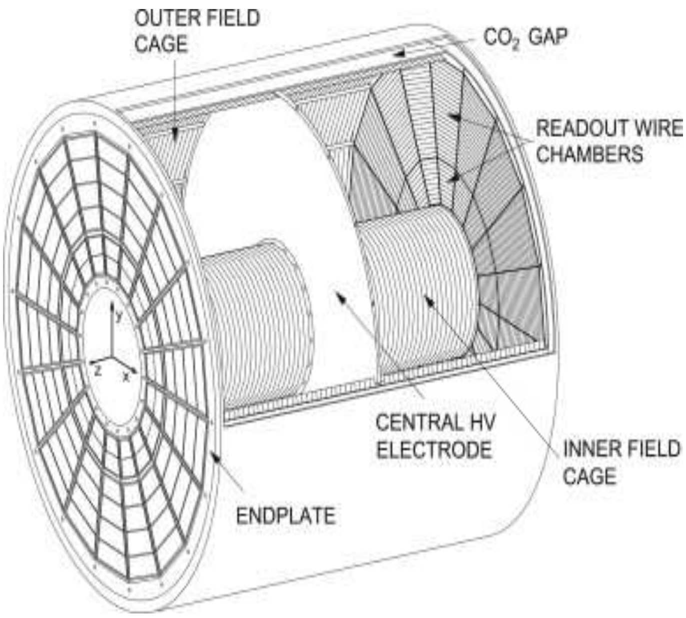

Figure 2.4: Three dimensional view of TPC.

The central electrode is kept at 100 kV and the field cage is operated at high voltage gradient of 400 V/cm. Whole TPC is provided with an uniform magnetic field of 0.5 T along the z-direction by the L3 magnet. Maximum drift time of TPC is 90 μs which defines the limiting factor for TPC to handle maximum luminosity and trigger rate. TPC trigger rates for p-p events and Pb-Pb events are 1kHz and 300Hz, respectively [88]. Becuase of this, pile up events are expected. For example, at luminosity of about $5 \times 10^{30} cm^{-2} s^{-1}$ in p-p collision with interaction rate 350 kHz, 30 p+p interactions are recorded with triggered events. Those pile-up tracks are removed during reconstruction by applying suitable vertex cuts.

When a charged particle passes through the gaseous medium, it ionizes the gas producing electrons. The liberated electrons drift from central electrode to the cathode pad readouts at each end plate, which are made up of Multi-Wire Proportion Chambers (MWPC). Each end plate has 18 sectors in azimuth and again each sector is segmented into 2 chambers radially. There are about 560,000 readout pads mounted in inner and outer chambers. Readout chambers are closed by gating grid to prevent space charge due to positive ions from drifting back from multiplication region of non-triggered and background interactions. Laser systems are provided for precise position inter-calibration and online monitoring of temperature and space charge distortion at the order of few mm. The digitization and signal processing is done by a chip called ALTRO (ALice Tpc ReadOut) which can handle 16 channels. Typical event size is about 30 MB at d$N_{ch}/d\eta$ = 2500.

Typically a track can have maximum 160 measured clusters. These measured clusters provide the information about the energy loss (-dE/dx) of the particle passing through the gaseous volume. Particle identification (PID) is done using this information based on the theoretical expectation obtained by famous Bethe-Bloch energy loss formula,

$$\langle\frac{dE}{dx}\rangle = \frac{4\pi Ne^4}{m_e c^2}\frac{Z^2}{\beta^2}\left(ln\frac{2m_e c^2\beta^2\gamma 2}{I} - \beta^2 - \frac{\delta\left(\beta\right)}{2}\right) \tag{2.1}$$

where m_e is the rest mass of electron, Z is the charge of the particle, N is the number density of electrons in the gas medium, I is the mean excitation energy of the atom and β is the velocity of the charged particle (ALICE uses a parametrized form of Bethe-Bloch formula proposed by ALEPH experiment [89]). TPC can identify charged particles of transverse momentum from 0.1 GeV/c to 100 GeV/c. The momentum resolution is $\sim$6% below 10 GeV/c and the dE/dx resolution is better than 5% for isoloated tracks [88]. TPC can give a 3-dimensional information of charged particle tracks which is done by Kalman filtering. The TPC only tracking efficiency saturates around 90%. The azimuthal resolution and longitudinal resolution are within 1110 to 1250 μm. So TPC is referred as a 3D camera. TPC, in conjunction with other detectors, is also used for vertex determination and generation of fast online High-Level Trigger (HLT) for the selection of rare events.

2.2.1.3 Transition Radiation Detector (TRD)

Transition Radiation detector is installed in between TPC and TOF at radial position of 2.9 m to 3.68 m from interaction point in the central barrel region. It has pseudorapidity coverage $-0.84 < \eta < 0.84$ and 2π azimuthal coverage. It has 18 super modules and each one consists of 30 modules arranged in five stacks along z-direction and 6 layers in radius. Each individual layer consists of a radiator, a drift chamber and MWPC with readout electronics. The radiator is composed of different inhomogeneous materials [90]. The drift chamber contains Xe+CO_2 (85:15) as counting gas. The readout electronics are realized as ASICSs.

The physics goal of TRD is to identify electrons from pion of momentum above 1 GeV/c to study the light and heavy meson resonances and dilepton continuum both in p+p as well as in Pb+Pb collisions. Electron-pion disentangling is done by transition radiation mechanism. When a charged particle passes through a medium of different dielectric constants, transition radiation occurs in terms of soft X-ray photons. The number of photon creations is directly proportional to the Lorentz factor γ of that charged particle. For example, a charged particle of p = 1GeV/c, the ratio of γ factor for electron to pion is 2000/7. This X-ray photons in turn produce electron clusters in the gas volume of the detector and after amplification it induces signal in the readout. Depending on the pulse height and average drift time, pions and electrons are separated [91]. At 90% efficiency of electron identification, only 1 pion out of 100 is misidentified as electron.

Using the tracklet information from its 6 layers, TRD is also used as a tracker to improve the momentum resolution in the central barrel. TRD uses L1 trigger to increase the yield for Υ and high p_T J/ψ produced directly from B-decay [92].

2.2.1.4 Time of Flight (TOF)

Time of Flight detector is made up of Multi-gap Resistive Plate Chambers (MRPC) technology [93]. TOF is cylindrical in design placed after TRD with inner and outer radii 370 cm and 390 cm, respectively. It covers the pseudorapidity range of $-0.9 < \eta < 0.9$ and full azimuthal space in the central barrel region. It has 18 sectors in ϕ with 5 segment in z-direction. Each sector has one module, which counts in total 90 modules. The active elements of TOF detector are 10-gap doubly-stacked MRPC strips which are placed inside each module (15 in the central, 19 in the intermediate and external modules) in a tilted manner to minimize the traversed path of the charged tracks through the chamber strips and to minimize the dead area. The tilting angle of those strips with respect to axis of the cylinder increases from 0^0 (central part) to 45^0 (most peripheral modules). These MRPC strips are enclosed inside the modules with a gas mixture of $C_2H_2F_4$ (90%), i-C_4H_{10} (5%) and SF_6 (5%) at atmospheric pressure. The MRPC strips are connected with the readout electronics. So in total 1638 MRPC strips have 157248 numbers of readout pads. The intrinsic time resolution is 40 ps and with other uncertainties, its overall time resolution is 150 ps and efficiency is close to 100% [86].

The MRPC are kept in high and uniform electric filed. When a charged particle passes through the gas volume, it produces avalanche immediately, which are collected by the readouts as signal with almost zero drift time. The particle identification is done by the time of flight technique. If t is the time of flight and L is the particle trajectory length, then mass of the charged particle can be calculated as,

$$m^2 = \frac{p^2}{c^2}\left(\frac{c^2t^2}{L^2} - 1\right) \tag{2.2}$$

Then two charged particles of unequal masses of m_1 and m_2 with same track length and same momentum p can be identified from the number of standard deviations in the time of flights difference as shown in equation 1.3.

$$n_\sigma = \frac{t_1 - t_2}{\delta t} \tag{2.3}$$

where

$$t_1 - t_2 = \frac{L}{2c}\left(\frac{m_1^2c^2 - m_2^2c^2}{p^2}\right) \tag{2.4}$$

and δt is the time resolution of the TOF detector. The basic physics goal of TOF in ALICE is to provide good PID capability in the intermediate momentum range. Using TOF information, pions to kaons and kaons to protons can be separated better than 3σ below 2.5 GeV/c and 4 GeV/c, respectively. ITS, TPC and TOF all together also used for vertex reconstruction and for dE/dx measurement below 1 GeV/c. This helps to study open heavy-flavor physics and vector meson resonances, like ϕ meson and ω meson.

2.2.1.5 High-Momentum Particle Identification Detector (HMPID)

The High-Momentum Particle Identification Detector (HMPID) has only acceptance of 5% in the central barrel region. It has only 5 modules which extends from 1.2^0 to 58.8^0 in azimuthal angle and has only pseudorapidity coverage of $-0.6 < \eta < 0.6$. HMPID working principle based on Ring Imaging Cherenkov radiation. A 15 mm thickness of liquid perfluorohexane (C_6F_6) is used as radiator. When a fast moving charged particle passes through the radiator it emits Cherenkov photons and these photons are detected by thin layer of CsI deposited onto the cathode pads of a MWPC. In between radiator and the MWPC, CH_4 is used as detector gas. The main goal of HMPID is to enhance PID capability beyond the momentum range attainable by ITS, TPC and TOF [94]. It can discriminate π/K and K/p on track-by-track basis up to 3 GeV/c to 5 GeV/c [86]. Its geometry is optimized for particles with large opening angle required for two-particle correlation measurements. HMPID can be used to identify high momenta light nuclei (^{3}He, α) also.

2.2.1.6 PHoton Spectrometer (PHOS)

PHoton Spectrometer (PHOS) is a single-arm high resolution electromagnetic spectrometer with high granularity. Its geometrical position is 460 cm from the interaction point and is placed at bottom part of ALICE detector. It covers $-0.12 < \eta < 0.12$ and up to 100^0 in azimuthal angle. It has two parts, one is highly segmented electromagnetic calorimeter (PHOS) and other one is a Charged particle Veto (CPV) plane. There are 5 modules of PHOS and each module has 3584 detection cells arranged in a 56$\times$64 matrix. The detection cells are made up of lead-tungstate crystal ($PbWO_4$) coupled to Avalanche Photo-Diode (APD). The CPV is a MWPC with cathode-pad readout placed on the top of PHOS module. CPV has better than 99% of charged particle detection efficiency. PHOS readout concept is adopted from TPC. The time resolution is about 2 ns at energies above 1.5 GeV [86][95].

PHOS is used for the measurements of neutral mesons, like π^0 and η, via their decayed photons. Direct photon measurements are done against decay photons by doing shower shape analysis. It also helps to study jet quenching and γ-jet correlations.

2.2.1.7 ElectroMagnetic Calorimeter (EMCAL)

The ElectroMagnetic CALorimeter (EMCAL) is a large Pb-scintillator sampling calorimeter with cylindrical geometry. It is placed $\sim$4.5 m from the beam line. The position of EMCAL is opposite to PHOS in azimuth and adjacent to HMPID. Its construction started in 2008 and its design is heavily influenced by its location within ALICE L3 magnet. It covers $|\eta| \leq 0.7$ and $\delta\phi = 107^0$. EMCAL is used to measure the neutral energy components of jet for full jet reconstruction in all collision systems. It also provides L0 and L3 trigger [96].

2.2.1.8 ALICE Cosmic Ray Detector (ACORDE)

ALICE Cosmic Ray DEtector (ACORDE) is an array of 60 plastic scintillators placed on the upper surface of L3 magnet. The azimuthal coverage is $-60^0 < \phi < 60^0$ and pseudorapidity coverage $-0.13 < \eta < 0.13$. ACORDE provides a fast L0 trigger to ALICE Central Trigger Process when atmospheric muons pass through the ALICE detectors. It is mainly used for calibration, alignment and performance of tracking detectors like ITS, TPC, TOF and HMPID. ACORDE can measure atmospheric muons which allow to analyze the muon momentum spectra from 100 GeV to 2 TeV with very high precision [86].

2.2.2 The Forward Detectors

There are some specialized small detector systems installed in the forward region of ALICE. They are used for triggering or to determine global event characteristics like collision time, collision vertex, centrality and event plane. These detectors are namely, ZDC, PMD, FMD, V0 and T0.

2.2.2.1 Zero Degree Calorimeter (ZDC)

There are two sets of hadronic ZDCs located at 116 m away from both side of the interaction point (IP). Each ZDC has two set of distinct detectors: one for spectator neutron (ZN) placed with almost 0^0 angle relative to LHC beam axis, other one is for spectator protons (ZP). ZP is placed externally to the outgoing beam pipe because the protons will be deflected by the magnetic element of beam pipe. This hadronic beam pipe is quartz fibres sampling calorimeter. When a particle passes through the dense absorber, it produces Cherenkov radiation in the quartz fibres. The signal is collected by optical readouts and fed to PMT and further to counting room. There are also two electromagnetic calorimeters (ZEM) used to compliment ZDC. A combination of signals coming form ZDC and ZEM provides three L1 triggers meant for event classification (central, semi-central and minimum bias events) [86].

2.2.2.2 Photon Multiplicity Detector (PMD)

The Photon Multiplicity Detector (PMD) is ingeniously developed by the Indian group. It is placed in the forward pseudorapidity region of $2.3 < \eta < 3.7$. The active element of the detector is made up of large array of honeycomb structured gas proportional counters installed in two planes perpendicular to the beam pipe. Each plane of PMD has 24 modules and each module is populated by 4608 numbers of honeycomb cells. One of the plane is called Charge Plane Veto (CPV) and another one is called preshower. In between the two planes, a lead converter of thickness 1.5 cm is kept. A charged particle is distinguished from photon by its shower size. Generally a charged particle does not produce any shower and it affects only one cell but when a photon passes through the lead converter it produces a shower of electrons and affects many cells of the pre-shower plane. By using the information from CPV and preshower plane, photon identification is done. PMD measures photon multiplicity on event-by-event basis which is used for the study of many physics topics, like limiting fragmentation, disoriented chiral condensates and fluctuations of global observables. PMD is also used to determine the event plane [97].

2.2.2.3 Forward Multiplicity Detector (FMD)

Forward Multiplicity Detector (FMD) consists of 5 rings and classified into three according to their position (FMD1, FMD2 and FMD3). FMD2 and FMD3 consist of both an inner and an outer ring. These are installed on either side of ITS detector. FMD1 is placed at 320 cm away from IP. FMD2 and FMD3 have same coverage in pseudorapidity in either side of IP (FMD2: $1.7 < \eta < 3.68$ and FMD3: $-1.7 > \eta > 3.68$). FMD1 covers pseudorapidity range $3.68 < \eta < 5.03$. Each inner detector ring is mounted by 10 and outer ring by 20 silicon strips. The signals from each silicon strip are collected and processed. ALTRO chips are used as Analog-to-Digital Converter (ADC). FMD plays a big role in providing a continuous multiplicity distribution in the forward region. FMD also allows to measure reaction plane required for azimuthal anisotropic measurement within the FMD's pseudorapidity coverage [86].

2.2.2.4 V0 detector

Two scintillator counters V0A and V0C are together called as V0 detector. V0A expanses over pseudorapidity range $2.8 < \eta < 5.1$ and is located 340 cm from IP on the opposite side of Muon spectrometer. V0C is situated at 90 cm from IP with pseudorapidity coverage $-3.7 < \eta < -1.7$. The scintillating materials consist of BC404. V0 serves as minimum-bias triggers provider to the central barrel detectors both in p+p and Pb+Pb collisions.

2.2.2.5 T0 detector

T0 detector consists of two arrays: T0-A and T0-C. Each array has 12 Cherenkov counters. The Cherenkov counters are made from Photo-multiplier tube, PMT-187. T0-C has pseudorapidity range $-3.28 < \eta \leq -2.97$ and T0-A has $4.61 \leq \eta \leq 4.92$. T0 is a very fast detector with dead time less than 25 ps. The main objective of T0 is to generate a start time for TOF detector. It can determine vertex position with a precision of $\pm$1.5 cm. It also provides L0 triggers and sends an early 'wake-up' signal to TRD prior to L0 trigger [86].

2.2.3 The Muon Spectrometers

Muon spectrometer is specially designed for muon detection and is installed in the C side of ALICE. It consists of an absorber to absorb hadrons and photons, 10 planes of high granular tracking system, a large dipole magnet, a passive muon-filter wall and four planes of trigger chambers. The 4.13 m length front absorber of radiation length $\sim 60X_0$ is placed inside the solenoid magnet 503 cm away from IP in negative z-direction. There are total 5 tracking stations to provide two-dimensional hit information with spatial resolution about 100 μm. Out of them, two are placed before dipole magnet, one inside and one outside the dipole magnet. Each tracking system had two chambers; each chamber has again two cathode planes. An iron wall of 1.2 m is used as muon filter. There are also two trigger detectors placed in two planes each made from RPC modules. Each trigger plane has 18 RPC modules. The dipole magnet is placed outside the L3 magnet at -z = 9.94 m from IP to allow reconstruction of muons momentum.

Muon Spectrometer can measure muon in the pseudorapidity region $-4.0 < \eta < -2.5$. This allows us to study vector meson resonances like ϕ meson to quarkania, i.e. J/Ψ, Υ and $\Upsilon^{'}$ through their μ^{+} and μ^{-} decay channels. It also allows to study the unlike sign di-muon continuum up to masses 10 GeV/c^2. Taking measurement of electrons from TRD and muons from Muon Spectrometer, e-μ coincidence study can also be done in ALICE [86].

2.3 ALICE Online systems

During data taking, the main role of ALICE online systems is to select physics events in an efficient way and finally to archive them to permanent data storage for later analysis. ALICE online system can be divided into four subsystems: Data Acquisition (DAQ), Central Trigger Processor (CTP), High Level Trigger (HLT) and Control Systems. Below, their working principle is discussed briefly how they accomplish the ALICE experiment.

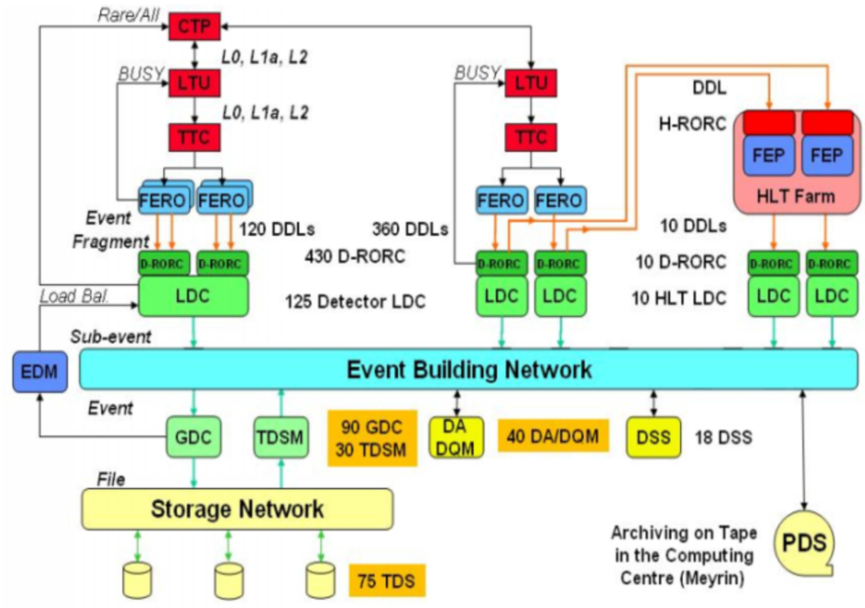

Figure 2.5: Schematic architecture of ALICE DAQ with interface to HLT [86].

2.3.1 Data AcQuisition (DAQ)

The main role of DAQ is to collect the collision data from different sub-detectors and save it to tape. ALICE uses several triggers to collect data, which use a large fraction of total data acquisition bandwidth. So the ALICE DAQ has to be really efficient to handle the demand of large data flow. A schematic architecture of DAQ system is shown in Figure 2.5. When a detector receives a trigger signal from CTP through a dedicated Local Logical Unit (LTU), it starts collecting data. The Fron-End Read-Out (FERO) electronics of detectors are interfaced with the Detector Data Links (DDL). Local Data Concentrators (LDCs) receive event fragments via DDL and then assemble them logically into sub-events. LDC decides the destination of each sub-event. The Event-Destination Manager (EDM) informs the LDCs about the availability of Global Data Collectors (GDCs). Then LDCs send the sub-events to GDCs where the full event building is done with appropriate trigger. The event building is managed by Event Building and Distribution System (EBDS) whose role to synchronise all LDCs and their destination GDC to balance the loads on different GDCs. Once event building is done and after a fixed size of data is obtained, GDCs archive the data in Transient Data Storage. These GDCs produced files are registered by AliEn and then TDS mover export them to CERN Computing Center

(CCC) to record them in Permanent Data Storage (PDS). DAQ comunicate with its various elements via TCP/IP protocol. The software used for DAQ is Data Acquisition and Test Environment (DATE), which uses UNIX system tools and its configuration is realized with MySQL. Monitoring Of Online Data (MOOD) is used to monitor the quality and visualisation of data created by ALICE detectors. MOOD is interfaced with DATE and it can handle online and offline data streams available on LDCs and on GDCs. DAQ framework has also Automatic Monitoring Environment (AMORE) to monitor the data quality by checking against some reference. If any data quality does not meet the desired reference, it gives alrams and initiates automatic recovery. ALICE DAQ has capability to process data at 1.25GB/s in Pb-Pb collisions.

2.3.2 Central Trigger Processor (CTP)

ALICE Central Trigger Processor (CTP) is designed to select events satisfying the requirements of physics demand and conditions imposed by the DAQ. CTP has broadly two categories of trigger levels. The first category is known as ‘fast’ part used for those detectors which have GASSIPLEX front-end chip. This ‘fast’ part has two levels: Level 0 (L0) and Level 1 (L1). L0 signal reaches detectors in 1.2 μs and receives all trigger inputs very fast. L1 signal is delivered after 6.5 μs and it picks all the remaining fast inputs. The second category of trigger is final level of trigger: Level 2 (L2). At high luminosity environment, event pile-up is a common issue. To make events reconstructable, ALICE uses a past-future protection circuit. Past-future protection circuit rejects events if any other event occurs within a specified time window. The time window depends on detectors response time. TPC is the slowest one with response time 88μs. So L2 trigger has to wait for the end of past-future protection interval (88μs) to verify whether an event can be recorded or not. The trigger signals are sent to the detectors using Local Trigger Unit (LTU). CTP has seven different types of 6U VME boards which mediate the trigger signals. There are 50 trigger classes and 60 trigger inputs (24 L0, 24 L1 and 12 L2) for ALICE. Triggers inputs are provided by various trigger detectors and synchronized to LHC clock cycles. Trigger class is defined by some logical conditions demanded for inputs from a set of detectors required for readout. A maximum of six combinations (called as detector clusters) can be defined at a time.

CTP also records several types of data related to its operations. For each accepted event, it sends information about orbit number, bunch crossing number, trigger information in L2 accept (L2a) message to detectors. It also records scalers and checks at regular intervals to check the correct information of triggers. To avoid any loss of rare events, all trigger classes are grouped into two groups: those corresponding to rare processes and those corresponding to common processes. At the initial stage, all trigger classes are activated and can generate triggers. When a temporary storage exceeds some predefined maximum limit, DAQ sends signal to disable the common classes to make available the band width for rare classes. Again when the temporary storage has gone below some corresponding minimum limit, the common classes are again enabled by DAQ.

2.3.3 High Level Trigger (HLT)

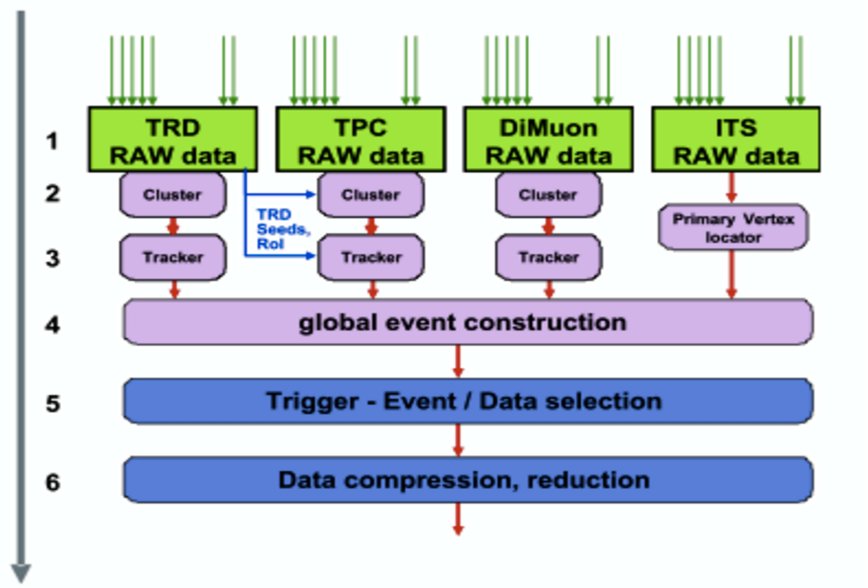

Figure 2.6: The six architectural layers of HLT [86].

High Level Trigger (HLT) does online analysis for event analysis and data compression to face the data volume. A single central Pb+Pb collision produces data of 75 MB and after all detectors information and trigger selection, the data flow rate becomes 25 GB/s. But in real, physics content is very small. So for a better management and compression of collision data, HLT follows a six layers of architecture which is shown in Figure 2.6. All detectors are connected with HLT by Detector Data Links (DDLs) and there are such 454 DDLs in ALICE. In the layer 1, raw data is collected via these DDLs. The Calibration, hit and clusters information extraction are done in layer 2. Individual reconstruction of events for each detector are done in third layer. Assembling of all detectors information and full event building is done in layer 4. In layer 5, selections of events are done based on the run specific physics selection criteria. At the end, data compression is done in sixth layer.

To perform this online analysis of events, HLT needs huge computing resources. This demand is met by a PC farm (located in the counting room in ALICE at Point2) of up to 1000 multi-processor computers running in parallel on the nodes. In order to keep inter-nodes traffic minimum, data processing is done in a hierarchical structure. Raw data processing is done directly on the Front-End Processors hosted by HLT-REadout Receiver Card (H-RORC) and the Global data processing is done in the computing nodes. HLT output DDLs are the mediator to send the trigger decision, Event Summary Data (ESD) of reconstructed events and compressed data to DAQ for data recording and archiving.

2.3.4 Control System

The main goal of ALICE Control System is to ensure safe, smooth and correct operation of the experiment. It has the ability to take pre-programmed decisions and automatic actions with least human intervention. Configuring, monitoring and controlling of both hardware and software equipments are done through a user interface from ALICE Control Room (ACR). It has two parts: Detector Control System (DCS) and Experiment Control System (ECS), which are discussed briefly below.

2.3.4.1 Detector Control System (DCS)

DCS checks the experimental environment, like cooling, water leakage and temperature in the experimental area. There are 8 sub-detectors, which has gas systems with their associated control system. DCS checks regularly those parameters and warns if it shows any anomaly. DCS has interlocks systems, which provides protection to the sub-detectors by switching of the electronics equipment, for example, when high temperature is detected on its electronics board. DCS also exchanges information with LHC machine about the magnet control system and other primary services.

2.3.4.2 Experiment Control System (ECS)

As we know there are several online systems in ALICE (DAQ, CTP, HLT, DCS), which work independently, as well as concurrently in partition during an experimental run. But during the commissioning phase, each detector is tested and debugged independently. This testing mode is called as 'standalone mode'. The role of ECS to coordinate the operations of online systems by receiving and sending commands to them through interfaces based on Finite-State-Machines (FSM). The major components of ECS are Detector Control Agent (DCA), Partition Control Agent (PCA), Detector Control Agent Human Interface (DCAHI) and Partition Control Agent Human Interface (PCAHI). DCA handles the standalone data acquisitions for the detectors running alone and it receives commands from the human interface (DCAHI). PCA job is to handle data acquisition runs using all the detectors active in the partition. PCA receives command from human interface PC-AHI and can exclude/include any detector from a partition. For a overall coordination among all the online systems, there interfaces like DCS/ECS, ECS/DAQ, ECS/HLT and ECS/TRG are provided.

2.4 ALICE Offline Analysis Framework

The data recorded during the experiment are stored in the permanent storage by the online systems for later analysis to explore the physics topics for respective experiment. The goal of ALICE offline analysis framework to process those data in various steps to extract the physics content. For that, ALICE Offline framework does various task such as simulation, reconstruction, calibration, alignment and visualization. The amount of computing resources required for data processing is huge which is not possible to do in a concentrated single place. Therefore, distributed computing facilities are made available around the world and this is coordinated by the Worldwide LHC Computing Grid

(WLCG) project. For an end-user to access the experimental data, a middleware for ALICE user is developed to connect with the Grid network called as Alice Environment (AliEn). AliRoot (Alice Root) is the framework on which the data analysis is carried out. A brief description of ALICE Grid, AliEn is given in next paragraph.

All the collision data are stored at large computing center called Tier-0. The large regional computing centers are called Tier-1, where the bulk jobs are done in organized way. There are also smaller computing centers all over the world called Tier-2, which are basically cluster around the Tier-1 facilities in a logical way. The end-user's jobs and simulation jobs are done in Tier-2. Data processing is done in a hierarchal manner. During data taking, data delivered from DAQ is moved to CERN Advance Storage (CASTOR) tapes (Tier-0) and first pass processing like reconstruction, calibration and alignment is done in CERN Analysis Facilities (CAF). This analysis is sometime called Quasi-online operation. During the first phase of reconstruction, a first set of Event Summary Data (ESD) files are generated. These data files contain the information of reconstructed tracks and global events properties. After data collection, a copy of raw data is stored at CERN and second copy is shared among the Tier-1 centers across the globe by Grid network. Second stage analysis, data reduction and Monte Carlo productions are done in all Tiers. Alien plays a very vital role as a Middleware for the user to interact with the distributed computing environment. AliEn is built on Open Source components and it uses web services and standard network protocols.

AliRoot framework is used for simulation, reconstruction, calibration and analysis of experimental data which was developed in 1998. It is based on Object-Oriented techniques for programming and ROOT is used as supporting framework. All frameworks are written in C++ language and AliEn system compliments it for access to Grid computing. Out of all jobs of AliRoot, only simulation and reconstruction framework are briefly discussed below.

2.4.1 Event Simulation

The offline event simulation framework is developed for efficient simulation for p-p and nucleus-nucleus collisions and the transport of particles through detectors to study the detector response. Different event generators, like PYTHIA [98], HIJING [99] with and without parameterized η and p_T distribution are used for simulation. Sometimes 'After-burners' are used to introduce user-defined particle correlation. The detector response simulation is done by different transport Monte Carlo packages, like GEANT3 [100], GEANT4 [101] and FLUKA [102]. They are interfaced with AliRoot and ROOT via Virtual Monte Carlo interface where signal processing in terms of summable digits are done. The geometry of all detectors, absorbers, beam pipe, solenoid and dipole magnets are described in a parameterized form in those packages.

2.4.2 Reconstruction Framework

The raw data is stored in terms of digital signals (ADC counts or summable digits) with the time information. The reconstruction framework uses digits from the detectors, module numbers, readout channel number, time bucket number, etc. as input for event reconstruction. The reconstruction involves these steps: cluster finding for each detectors, primary vertex reconstruction, track reconstruction and secondary vertex reconstruction. After reconstruction is done the output is written in Event Summary Data (ESD) files with the name of AliESDs.root. Later on depending on the requirements of different Physics Working Group (PWG), events are filtered and stored in Analysis Object Data (AOD) files. The AOD files (AliAODs.root) are smaller in size and very specific with respect to analysis type which is more user friendly and also takes less computing time.

Chapter 3

Higher Moments Analysis Methodology

In day-to-day life, we come across many events, whose observations are studied through probability theory and statistical methods. A collection of samples, e.g. marks secured by students in a class, demography of human population, economical growth rate etc. always has a distribution. Most widely used terms in interpretation of a distribution are mean and standard deviation; the mean (μ) of the distribution represents average value or expected value of the sample, standard deviation (σ) indicates the variation or dispersion of the sample from the average value. Mathematically, μ is the first moment of the distribution, whereas σ are the square root of second moments of the distribution. Apart from these two moments, we can also have other higher moments of a given distribution, which are more sensitive towards the nature of the distribution and regarded as miniature probe for the samples under study. These higher moments play very important role in every sector of human life, e.g. industrial, economics, Biology and most remarkably in Physics. As discussed in Chapter 1, many models having statistical background are successful in describing the heavy-ion collision system. Here, the discussion of higher moments will be done with a specific physics interest as pointed out in the introduction chapter. In this chapter, details of the analysis method will be done by giving mathematical introduction for higher moments and then a connection between the higher moments and the observables of lattice QCD is drawn. Then the interpretation of higher moments of conserved quantity in a heavy-ion collision system in Hadron Resonance Gas (HRG) model along with some baseline study is given. In section 3.6, various methodologies of higher moments analysis are discussed.

3.1 Mathematical Background

If 'x' is a real-valued random variable and $f(x)$ is the probability density function of x, then the n^{th} raw moment (m'_n) is given as,

$$m'_n = \int_{-\infty}^{+\infty} x^n f(x)dx \Rightarrow m'_n = \langle x^n \rangle \tag{3.1}$$

Alternatively, moment generating functions are used in place of probability density function to find out the moments of a random variable. In terms of moment generating function $M_x(t)$,

$$M_x(t) = \langle e^{tx} \rangle, t \in \mathbb{R} \tag{3.2}$$

the n^{th} order raw moments can be found out in the following way,

$$m'_n = \frac{d^n M_x(t)}{dt^n}|_{t=0} \tag{3.3}$$

provided the expectation value of $M_x(t)$ exists.

Cumulants are also treated as alternative to the moments. The relation between cumulant generating function, $g(t)$, and moment generating function, $M_x(t)$, is

$$g(t) = \log[M_x(t)] \tag{3.4}$$

and the n^{th} order cumulants can be obtained as the n^{th} derivative of the cumulant generating function evaluated at $t = 0$.

$$c_n = \frac{d^n g(t)}{dt^n}|_{t=0} \tag{3.5}$$

3.1.1 Relation Among Various Order Moments and Cumulants

Using Equation 3.3 and 3.5, one can find the relation among the various order moments and cumulants. Here are few examples given below.

$$m'_1 = c_1 \tag{3.6}$$

$$m'_2 = c_2 + c_1^2 \tag{3.7}$$

$$m'_3 = c_3 + 3c_2c_1 + c_1^3 \tag{3.8}$$

$$m'_4 = c_4 + 4c_3c_1 + 3c_2^2 + 6c_2c_1^2 + c_1^4 \tag{3.9}$$

$$m'_5 = c_5 + 5c_4c_1 + 10c_3c_1^2 + 15c_2^2c_1 + 10c_2c_1^3 + c_1^5 \tag{3.10}$$

$$\begin{aligned} m'_6 = {} & c_6 + 6c_5c_1 + 15c_4c_2 + 10c_3^2 + 60c_3c_2c_1 + 20c_3c_1^3 + 15c_2^3 + 45c_2^2c_1^2 \\ & +45c_2^2c_1^2 + 15c_2c_1^4 + c_1^6 \end{aligned} \tag{3.11}$$

Conversely, relation among cumulants and moments can be written by a recursion formula,

$$c_n = m'_n - \sum_{m=1}^{n-1} \binom{m-1}{n-1} c_m m'_{n-m} \tag{3.12}$$

So far raw moments or non-central moments and their relation with cumulants are discussed. Central moments are computed with respect to deviation from the mean, whereas non-central moments are calculated with respect to zero. Now the n^{th} order central moments can be written by the following Equation 3.1 as,

$$m_n = \int_{-\infty}^{+\infty} (x-\mu)^n f(x)dx \Rightarrow m_n = \langle (x-\mu)^n \rangle \tag{3.13}$$

where μ is the mean of the distribution. Consequently, the moment generating function and cumulant generating function will change accordingly. The common feature of non-central and central moments is that the zeroth order moment is always one. For central moment, the first order moment is zero. So the relation among central moments and cumulants can be evaluated from Equation 3.6 to 3.10 by putting $c_1 = 0$ as follows.

$$m_1 = 0 \tag{3.14}$$

$$m_2 = c_2 \tag{3.15}$$

$$m_3 = c_3 \tag{3.16}$$

$$m_4 = c_4 + 3c_2^2 \tag{3.17}$$

$$m_5 = c_5 + c_3 c_2 \tag{3.18}$$

$$m_6 = c_6 + 15c_4c_2 + 10c_3^2 + 15c_2^3 \tag{3.19}$$

The second central moment is called as variance and the square root of it is called as

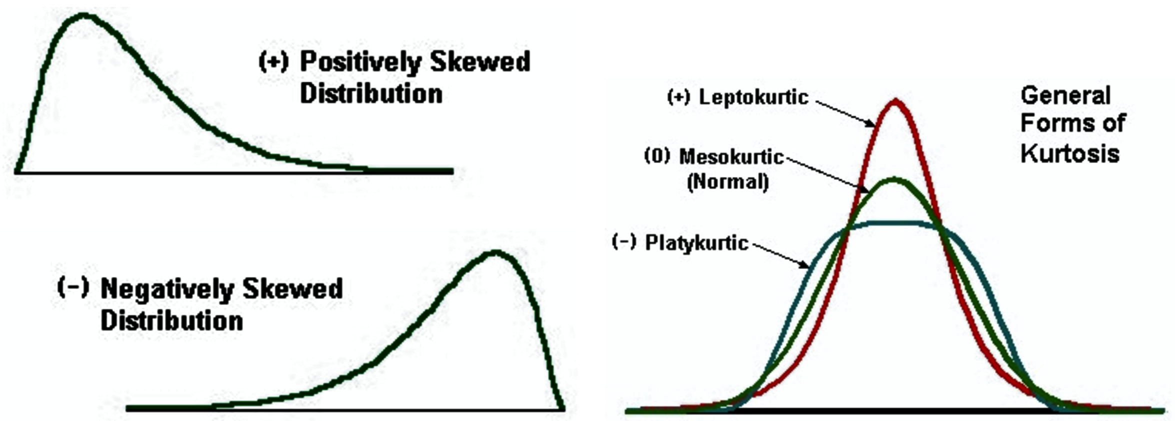

Figure 3.1: The pictorial representation of Skewness and kurtosis.Figures are taken from Ref. [103]

standard deviation and represented as σ. *Skewness (S)*, which is equal to ratio of third order cumulant to cube of σ. The value of skewness represents the asymmetry of the samples in a particular direction. For example, for positive skewness, the distribution has longer tail in right side of it and for negative value, it has longer tail in left side. However, for a symmetric distribution, which may have tail on both sides, then the asymmetries cancel out and gives zero skewness. A typical positive and negative skewed distribution is given in Figure 3.1. Similarly, *kurtosis (κ)* is used to quantify the degree of peakedness of a distribution, which is represented pictorially in Figure 3.1. It is defined by ratio of fourth order cumulant to square of second order cumulant as follow.

$$S = \frac{m_3}{\sigma^3} = \frac{c_3}{c_2^{3/2}} \tag{3.20}$$

$$\kappa = \frac{c_4}{c_2^2} = \frac{m_4}{m_2^2} - 3. \tag{3.21}$$

3.1.2 Properties of Moments and Cumulants

Here some properties of moments and cumulants under mathematical operations are given.

3.1.2.1 Translational invariance

If c_n and m_n are n^{th} order cumulant and moment of the probability distribution function of a random variable *x*, then

- $c_n(x+k) = c_n(x) + k$
- $c_n(x+k) = c_n(x),$ for $n \geq 2$
- $c_n(kx) = k^n c_n(x)$
- $m_n(x+k) = m_n(x) + k$
- $m_n(kx) = k^n m_n(x)$

where k is a constant.

3.1.2.2 Additive property

If $c_n(x)$ and $c_n(y)$ are n^{th} order cumulants of the probability distribution function of random variables *x* and *y*. Similarly, If $m_n(x)$ and $m_n(y)$ are n^{th} order moments of the probability distribution function of random variables *x* and *y*. Then,

- $c_n(x+y) = c_n(x) + c_n(y)$
- $m_n(x+y) = m_n(x) + m_n(y),$ for $1 \leq n \leq 3$

3.2 Lattice QCD In Short

Lattice QCD has been successfully used to test the theory of Strong interaction. Wilson is first to use Euclidean gauge theories in the lattice to study the confinement and work in the non-perturbative regime of QCD. It is based on Feynman path integral techniques for its numerical implementation. It is described by the regular set of space-time grid where quarks are placed at lattice site with finite spacing and they are connected by gauge fields (gluons). The most commonly used terminologies for lattice formulation are: site, link, plaquette. Sites are the lattice points defined by coordinates in the unit of lattice spacing. Link is the shortest distance connecting two sites characterized by coordinates and direction. Plaquette represents the elementary square bounded by four lines having both coordinates and two-dimensional directions. A schematic representation of lattice space is given in Figure 3.2. The basic inputs for the lattice calculations are, lattice spacing, light quark masses and heavy quark masses. The lattice spacing is fixed by equating with bare coupling constant and can be determined by mass of hadron. The *u, d* and *s* are treated as light quark with the sense of $m_{u,d,s} < \Lambda_{QCD}$, whereas, *c* and *b* quarks are treated as heavy quarks.

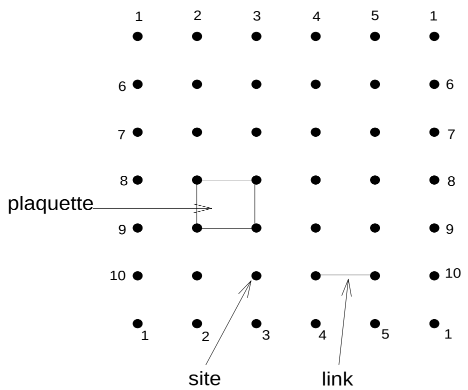

Figure 3.2: Schematic representation of a lattice in two dimensions [104].

The numerical implementation of lattice QCD is done in the following steps [10]:

1. Discretization of space-time grid: The possible ways are hypercubic, body-centered cubic and random lattice.

2. Transcription of the gauge and fermion degrees of freedom: The transcription of

field variables like the quark field is represented by anti-commuting Grassmann variables (mathematically constructed) and the fermionic function integral is done by the sum over all possible paths touching each site a maximum of one time. In lattice theory, the symmetry group of continuum theory (Poincare invariance) is reduced to a discrete group. So in addition to local gauge symmetry, the lattice action is invariant under parity, charge conjugation and time reversal.

3. Construction of the action: The lattice action are formulated again in two classes: gauge action and fermionic action. Gauge action can be expressed in terms of closed loops and gauge action for SU(3) are called as Wilson action. There are many ways of formulation of fermionic action, e.g. Wilson fermions, staggered fermions, domain wall fermions etc. Naive Fermionic actions have "doubling" problem while discretization of Dirac action and is partially fixed till now.

4. Definition of the measurement of integration in the path integral and transcription of the operators used to probe the physics

Numerical implementation of lattice QCD is done by evaluating the Euclidean-space partition function. The partition function is defined as [105],

$$Z = \int d[U] \prod_f d[\psi_f] d[\psi'_f] e^{-S_g[U] - \sum_f \psi'_f (D[U]+m_f)\psi_f} \tag{3.22}$$

where ψ and ψ' are Grassmann quark and anti-quark fields of flavour *f*, D$[U]$ is the chosen lattice Dirac operator with m_f the quark mass in the lattice units.

After integrating quarks and anti-quark fileds,

$$Z = \int d[U] e^{-S_g[U]} \prod_f det\left(D[U] + m_f\right) \tag{3.23}$$

As it involves many integration, direct numerical integration is impractical, so it is done by Monte-Carlo techniques. As we know, in any Monte-Carlo methods, one has to compute the ensemble average of a physically relevant observable. Similarly, in lattice QCD, the basic ingredients of calculations are expectation values of multi-local gauge-invariant operators,

$$\langle \mathcal{O}(U,q,\bar{q})\rangle = \frac{1}{Z}\int [dU]\prod_f d[\psi_f]d[\psi'_f]\mathcal{O}(U,q,\bar{q})e^{-S_g[U]-\sum_f \psi'_f\left(D[U]+m_f\right)\psi_f} \tag{3.24}$$

For a 10^4 space-time lattice, there will be approximately 4×10^4 number of links. For SU(3), each link variable is a function of 8 real parameters. Hence, there will be 3,20,000 integrations to be done, which is CPU intensive. To do an effective computing, several algorithms are used, like Metropolis algorithm, Langevin algorithm, Molecular dynamics method, Hybrid Monte Carlo (HMC) algorithm.

Study of QCD both at high and low temperature is important in terms of thermodynamical observables, which can be numerically calculated in the framework of lattice QCD. Finite temperature lattice QCD has made remarkable progress in establishing the ground for the test of theory of QCD and has predicted many interesting QCD phenomena like QCD phase transition and chiral symmetry breaking.

3.3 Higher Moments in Connection With Lattice QCD

A single entity has not much to say about itself. A segregation of single entities has some group characteristics, reflects the bulk nature and hence, entitled to statistical interpretation. For example, a single water molecule (H_2O) has only few physical and chemical properties to be described about. But a collection of Avogadro's number of H_2O forms a medium, has specific boiling and freezing point, has bulk properties like viscosity, conductivity, the temperature of all molecules follows certain statistical distribution etc. Its thermodynamical variables like pressure, temperature and volume can be calculated by certain statistical methods at equilibrium. These variables are called as state variables categorized into two. These are, (i) extensive: scales linearly with the system size (e.g. volume V, particle number N, total energy E, magnetization M) (ii) intensive: independent of system size (e.g. p, T, chemical potential μ). In statistical mechanics, instead of looking properties of individual entity, it provides information of the whole system in an average sense. This is done by considering many copies of the system called as *ensemble*, which may have different possible states. In other words, it is a probability distribution of the state of the system under study. There are three types of ensemble to describe the thermodynamics of a system under statistical equilibrium: micro canonical, canonical and grand canonical ensemble. In micro canonical ensemble, the system is isolated from surrounding so that both the number and energy of the system is fixed. In canonical ensemble, the system can exchange the energy with the surrounding, not the particles. Grand canonical ensemble, the system can exchange both particles and energy with the system. In spite of going details of it, some exemplary exercises are discussed below to articulate the relations between the higher moments of conserved quantities and lattice QCD observables.

As mentioned earlier, in grand canonical ensemble, the numbers are fluctuating between system and surrounding. Then the average number of particles can be found out as follows [106].

$$\begin{aligned}
\langle N \rangle &= \frac{\sum N z^N \mathcal{Q}_N}{\sum z^N \mathcal{Q}_N} && (3.25)\\
&= z\frac{\partial}{\partial z} ln\mathcal{Q}(z,V,T) && (3.26)\\
&= kT\frac{\partial}{\partial \mu} ln\mathcal{Q}(z,V,T), && (3.27)
\end{aligned}$$

where, $\mathcal{Q}(z,V,T) = \sum_{N=0}^{\infty} z^N \mathcal{Q}_N(V,T)$ is the grand canonical partition function, $\mathcal{Q}_N(V,T)$ is the partition function of canonical ensemble, $z = exp(\mu/kT)$ is the fugacity and μ is the chemical potential. Similarly, the mean-square fluctuation will be,

$$\begin{aligned}
\langle N^2 \rangle - \langle N \rangle^2 &= \frac{\sum N^2 z^N \mathcal{Q}_N}{\sum z^N \mathcal{Q}_N} - \left[\frac{\sum N z^N \mathcal{Q}_N}{\sum z^N \mathcal{Q}_N}\right]^2 && (3.28)\\
&= z\frac{\partial}{\partial z} z\frac{\partial}{\partial z} ln\mathcal{Q}(z,V,T) && (3.29)\\
&= (kT)^2\frac{\partial^2}{\partial \mu^2} ln\mathcal{Q}(z,V,T) && (3.30)
\end{aligned}$$

In the left hand side of Equation 3.25 and 3.28 are the first and second order cumulants, respectively. Thus, other higher cumulants of the particle numbers can be evaluated by taking higher derivatives of partition function with respect to chemical potential. Meanwhile, in lattice QCD, the partition function can be numerically calculated as discussed earlier, and then the dimensionless pressure ($\frac{p}{T^4}$) [107],

$$\frac{p(T, \mu_B, \mu_Q, \mu_S)}{T^4} = \lim_{V \to \infty} \frac{1}{VT^3} lnZ(T, \mu_B, \mu_Q, \mu_S, V) \tag{3.31}$$

where Z is the QCD partition function and μ_B, μ_Q, μ_S are the chemical potential of net-Baryon, net-charge and net-strangeness, respectively. Net-Baryon, net-charge and net-strangeness are the conserved quantities. Now the n^{th} order generalized susceptibility of conserved quantities can be calculated by taking the derivative of dimensionless pressure as [107],

$$\chi_q^{(n)}(T, \mu_B, \mu_Q, \mu_S) = \frac{\partial^n (p/T^4)}{\partial(\mu_q/T)^n} \tag{3.32}$$

$$= \frac{1}{VT^3} \frac{\partial^n lnZ}{\partial(\mu_q/T)^n} \tag{3.33}$$

where, $q = Q, B$ or S. Now looking at Equation 3.26, 3.29, and 3.32, the relation among mean and variance to the quark number susceptibility of conserved quantities are,

$$\langle N \rangle = VT^3 \chi_q^{(1)} \tag{3.34}$$

$$\langle N^2 \rangle - \langle N \rangle^2 = VT^3 \chi_q^{(2)} \tag{3.35}$$

In heavy-ion collision experiment, one can measure the net-charge (ΔN), net-proton (Δp) and net-strangeness (ΔS) number event-wise. For a large number of events, various order cumulants of the distributions can be calculated. In lattice QCD, only the quark number susceptibilities are physical observables. Now from above equations, a most generalized relation between quark number susceptibilities to the cumulants can be drawn as follow [107].

$$c_n = VT^3 \chi_q^{(n)} \tag{3.36}$$

The left hand side of Equation 3.3 is experimentally measured quantity and the quantity of right hand side is lattice observable. This is why the study of higher moments (cumulant) of conserved quantities is an excellent tool to compare directly to the lattice QCD predictions with experimental findings.

As measurement of volume of the system in heavy-ion collision experiment is a cumbersome job, the data are most often interpreted as the ratio of cumulants to cancel the volume term or in other way, in lattice QCD, the predictions are done as the ratio of various order of susceptibilities, which are given below.

$$S\sigma = \frac{\chi_q^{(3)}}{\chi_q^{(2)}} \tag{3.37}$$

$$\kappa\sigma^2 = \frac{\chi_q^{(4)}}{\chi_q^{(2)}} \tag{3.38}$$

$$\frac{\sigma^2}{M} = \frac{\chi_q^{(2)}}{\chi_q^{(1)}} \tag{3.39}$$

$$\frac{c_6}{c_2} = \frac{\chi_q^{(6)}}{\chi_q^{(2)}} \tag{3.40}$$

3.4 Hadron Resonance Gas (HRG) Model

Hadron Resonance Gas model has successfully used to explain the thermal abundances of hadrons in heavy-ion collisions at appropriately chosen temperature and chemical potential [108]. Like in lattice QCD, the partition function of HRG model contains all relevant degrees of freedom of the confinement of QCD matter and also includes the interactions which involves formation of resonances. The dimensionless pressure is defined as [109],

$$\begin{aligned} \frac{p^{HRG}(T,\mu_B,\mu_Q,\mu_S)}{T^4} &= \frac{1}{VT^3}\sum_{i\in mesons} lnZ^{mesons}_{m_i}(T,\mu_B,\mu_Q,\mu_S,V) \\ &+ \sum_{i\in Baryons} lnZ^{Baryons}_{m_i}(T,\mu_B,\mu_Q,\mu_S,V) \end{aligned} \tag{3.41}$$

where

$$lnZ^{Baryons/Mesons}_{m_i} = \mp\frac{Vd_i}{2\pi^2}\int_0^\infty dk k^2 ln\left(1 \mp z_i e^{-\varepsilon_i/T}\right) \tag{3.42}$$

with energies $\varepsilon_i = \sqrt{k^2+m_i^2}$, d_i is the degeneracy factor and z_i is the fugacities.

$$z_i = exp(\left(\sum_a X_i^a \mu_{X^a}\right)/T) \tag{3.43}$$

Here X^a is considered as all possible conserved charges. In the Boltzmann approximation, the thermodynamic pressure now can be written as [107],

$$\frac{p}{T^4} = \frac{1}{\pi^2}\sum_i d_i(m_i/T)^2 K_2(m_i/T) \times cosh\left[(B_i\mu_B + S_i\mu_S + Q_i\mu_Q)/T\right] \tag{3.44}$$

Here the summation is taken over stable hadrons and resonances. Looking at Equation 3.31 and Equation 3.45, it can be proved that,

$$\frac{\chi_q^{(3)}}{\chi_q^{(2)}} = 1, \& \quad \frac{\chi_q^{(4)}}{\chi_q^{(2)}} = 1 \tag{3.45}$$

There is an interesting consequence of the HRG model for net-Baryon number, i.e

$$\kappa_B\sigma_B^2 = 1, \& \quad \kappa_B M_B = S_B\sigma_B \tag{3.46}$$

and for $\mu_S = \mu_Q = 0$,

$$S_B\sigma_B = tanh(\mu_B/T) \tag{3.47}$$

This Equation is a good approximation in heavy-ion collisions, the μ_S and μ_Q are much smaller than μ_B. In Figure 3.3, a comparison of HRG model predictions at freeze-out with RHIC results of net-proton number fluctuations is shown. This suggests that the HRG model provides a good description of ratio of different moments of net-proton at RHIC [76]. Similarly, in Table 3.1, the values of ratio of various order moments of net-Baryon and net-charge fluctuations are given for several values of collision energies starting from RHIC low energy to current LHC energy.

However, there are some deviations of HRG model with respect to lattice QCD calculations reported at vanishing baryon chemical potential and for the temperature close to the transition temperature. Like, in lattice QCD, as a consequence of chiral symmetry restoration, all moments (χ_B^n) will diverge for $n \geq 6$ at T_C. Similarly, at $m_q \neq 0$, χ_B^n will be oscillatory in nature. χ_B^6 will vanish at the transition temperature. At the transition region, the value of χ_B^8 will be negative. But on the other hand, in HRG model, all moments of net-baryon are positive. Lattice QCD calculation suggests that, χ_B^6/χ_B^2

Table 3.1: Ratios of the moments of baryon number and electric charge fluctuations calculated in HRG model for RHIC low energy to LHC energy.

$\sqrt{s_{NN}}$	$\chi_B^{(2)}/\chi_B^{(1)}$	$\chi_B^{(3)}/\chi_B^{(2)}$	$\chi_Q^{(2)}/\chi_Q^{(1)}$	$\chi_Q^{(3)}/\chi_Q^{(1)}$
7.7	1.01	0.99	4.18	0.49
11.5	1.05	0.95	5.39	0.39
19.6	1.23	0.81	7.95	0.27
39.0	1.87	0.53	14.25	0.15
62.4	2.75	0.36	21.97	0.09
200.0	8.20	0.12	67.80	0.03
2760	111.1	0.09	922.4	0.02

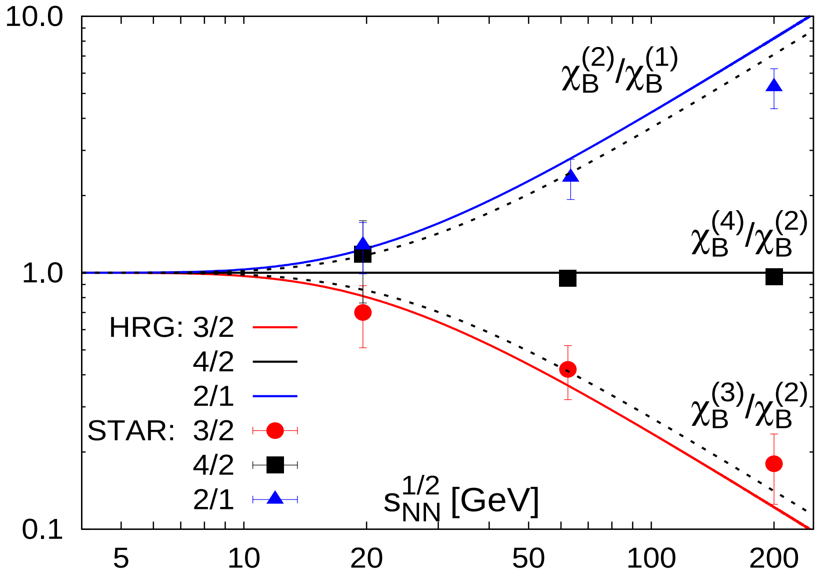

Figure 3.3: Ratios of various order cumulants calculated in the HRG model on the feeze-out curve are compared with RHIC results. Figure is taken from Ref [107].

vanishes at pseudo-critical temperature and rapidly rises for temperature below it contrary to the HRG model where its ratio is one. Ref [107] states that, “ *if the critical point exist in QCD and if the freeze-out occurs within the critical region, then already the second moments of baryon number and electric charge fluctuations should deviate from the HRG model result. The higher order cumulants should exhibit even stronger sensitivity to critical fluctuations showing larger deviations from the model predictions*”. Moreover, they suggests that the higher order moments at LHC energies will reveal the difference between the HRG model and lattice QCD calculations and will help to find the critical behavior at $\mu_B/T \simeq 0$.

3.5 Baseline Study

Before going to experimental measurements on higher moments of charged and proton number fluctuations, there are some baseline studies, which can be done on the mathematical basis with physics reasoning. There are two baseline studies discussed below.

3.5.1 Poissonian Expectation

Assuming the multiplicity distribution of positive and negative charged particles to be Poissonian distribution, then the net number of the conserved charges (electric charge, baryon number of strangeness) can be described by Skellam probability distribution function. This Skellam distribution has been used in HRG models [110, 111]. In probability and statistical language, the resultant distribution of difference between two probability functions of two independent random variables X and Y will be a Skellam distribution. If the probability distribution of positive and negative charged particles are of the Poissonian form:

$$f(n_1;\mu_1) = \frac{\mu_1^{n_1}}{n_1!}e^{-\mu_1}, f(n_2;\mu_2) = \frac{\mu_2^{n_2}}{n_2!}e^{-\mu_2} \tag{3.48}$$

where μ_1 and μ_2 are the mean of the probability distribution of random variables X and Y. Then the probability distribution of $\Delta N = X - Y$ will be a Skellam distribution given by

$$f(k;\mu_1,\mu_2) = e^{-(\mu_1+\mu_2)}\left(\frac{\mu_1}{\mu_2}\right)^{k/2} I_{|k|}(2\sqrt{\mu_1\mu_2}) \tag{3.49}$$

where $I_{|k|}$ is the modified Bessel function and $k = n_1 - n_2$. Now different moments of the Skellam distribution can be found by these simple expressions,

$$\mu = \mu_1 - \mu_2 \tag{3.50}$$

$$\sigma = \sqrt{\mu_1 + \mu_2} \tag{3.51}$$

$$S = \frac{\mu_1 - \mu_2}{(\mu_1 + \mu_2)^{3/2}} \tag{3.52}$$

$$\kappa = \frac{1}{\mu_1 + \mu_2} \tag{3.53}$$

$$S\sigma = \frac{\mu_1 - \mu_2}{\mu_1 + \mu_2} \tag{3.54}$$

$$\kappa\sigma^2 = 1 \tag{3.55}$$

3.5.2 Negative Binomial Expectation

Recently Ref [112] has proposed that Negative Binomial Distribution (NBD) can be used to describe the behavior of the higher moments of net-charge and net-proton distributions in heavy-ion collisions. They argue that, as (negative) binomial distribution (NBD) describes the experimental multiplicity distributions in better way; so it can be used for the baseline study. The negative binomial distribution is also known as the Pascal distribution and it describes the probability of r-1 successes and x failures in $x + r - 1$ trials, and success on the $(x + r)$th trial. The NBD probability density function is

$$P_{r,p}(x) = \binom{x+r-1}{r-1} p^r (1-p)^x \tag{3.56}$$

where p is the probability. Before calculating the cumulants of the net-charge or net-proton distributions, first one has to find the various order cumulants of individual distributions. For a NBD distribution, if μ and σ are the mean and sigma of the individual distribution, respectively, then n^{th} order moments can be calculated as follows.

$$m_1 = \frac{r(1-p)}{p} \tag{3.57}$$

$$m_2 = \frac{r(1-p)}{p^2} \tag{3.58}$$

$$m_3 = \frac{r(p-1)(p-2)}{p^3} \tag{3.59}$$

$$m_4 = \frac{r(1-p)(6-6p+p^2+3r-3pr)}{p^4} \tag{3.60}$$

where $p = \mu/\sigma^2$ and $r = \mu p/(1-p)$. Now accordingly the n^{th} order cumulants of individual distributions can be calculated. Then the generalized expression for n^{th} order cumulants of the resultant distribution will be,

$$c_n = c_{n,+} + (-1)^n c_{n,-} \tag{3.61}$$

where $c_{n,+}$ and $c_{n,-}$ are the n^{th} order cumulants of positive and negative particles distributions, respectively. The variance of NBD is larger than the mean. The Poissonian distributions are the limiting case of NBD where the mean and variance are same.

3.6 Analysis Methodology

In higher moments analysis, here are the methodologies followed throughout the analysis.

3.6.1 Centrality Bin Width Correction

In heavy-ion collision physics, centrality is used as costumed term to characterize the events with different multiplicities. Centrality is directly related to the impact parameter and impact parameter is defined as the distance between the centers of the two colliding nuclei in a plane transverse to the beam axis. The Monte-Carlo simulation of geometrical Glauber model is used to infer the multiplicity distribution and to determine the centrality. The centrality percentile c of an A-A collision with an impact parameter b is defined as,

$$c = \frac{1}{\sigma_{AA}} \int_0^b \frac{d\sigma}{db'} db' \tag{3.62}$$

where σ_{AA} is the total nuclear interaction cross section of A-A collision. In this model, the initial overlap region is expressed by the number of participating nucleons (N_{part}), which have undergone one or more binary collisions with nucleons of the other nucleus. In experiment, the geometrical variables, like impact parameter, N_{part} or N_{coll} can not be measured. In ALICE, the centrality is determined by comparing the Monte-Carlo Glauber model to the multiplicity of the events or from the energy deposited in ZDC detector. But particle multiplicity not only depends on the physics process but also depends on initial geometry. It implies that the particle multiplicity and impact parameter don't have one-to-one correspondent. So there may be fluctuations of particle numbers even for a fixed impact parameter. In experiment, there will be a centrality resolution factor because of the finite detector resolution, as if we look at the smaller centrality bin, the particle multiplicity will be largely reduced. So in an event-by-event measurement, for different impact parameters, the corresponding multiplicity and hence the centrality will be same. This will add extra fluctuations to each centrality and will largely affect the higher moments measurements at wider centrality bin. So to eliminate this bin width effect, centrality bin width correction (CBWC) is done to calculate the various moments for each multiplicity in one wide centrality bin. In this CBWC method, the moments are calculated by weighted average of the number of events in each small centrality bin. The general formula for CBWC is as follows [113].

$$m_n = \frac{\sum_r n_r m_{n,r}}{\sum_r n_r} = \sum_r \omega_r m_{n,r} \tag{3.63}$$

where r is the number of bins within the centrality range under consideration, n_r is the number of events in the r^{th} bin and $m_{n,r}$ is the n^{th} moments measured in r^{th} bin.

3.6.2 Central Limit Theorem

According to the theory of probability, Central Limit Theorem (CLT) states that after sufficiently large number of iterations of independent random variables, each with a well defined expected value (mean) and well defined variance, will lead to a normal distribution, regardless of the underlying distribution. Here two points have to be emphasized; the random variables must be identically distributed and they are independent. As these higher moments analysis of net-charge and net-proton distributions are statistical in nature, CLT can be applied to it. CLT is used to understand the evolution of various order moments with respect to events belonging to certain centrality (impact parameter) class. Here, the assumption used is that the colliding system consists of a large number of identical, independent emission source (IIES) and the final multiplicity of particles can be accounted as the sum of the contribution of multiplicities from all those individual emission sources [114]. Now under the assumption of IIES, n^{th} order moment of i^{th} centrality will be,

$$m_{n,i} = N_i m_{n,i}(x), \text{for } n = 1, 2, 3, ..., n \tag{3.64}$$

where N_i is the number of emission sources in the i^{th} centrality and $m_{n,i}(x)$ is the n^{th} order parent moments of those identical sources labeled as x. Now various order moments can be derived as follows.

$$\mu_i = N_i \mu(x) \tag{3.65}$$

$$\sigma_i^2 = N_i \sigma^2(x) \tag{3.66}$$

$$S_i = \frac{S(x)}{\sqrt{N_i}} \tag{3.67}$$

$$\kappa_i = \frac{\kappa(x)}{N_i} \tag{3.68}$$

Now again the following identity can be found from the above equations,

$$\frac{\mu_i}{\sum_{i=1}^n \mu_i} = \frac{\sigma_i^2}{\sum_{i=1}^n \sigma_i^2} = \frac{1/S_i^2}{\sum_{i=1}^n \S_i^2} = \frac{1/\kappa_i}{\sum_{i=1}^n \kappa_i} = \frac{N_i}{\sum_i^n N_i} \tag{3.69}$$

The centrality evolution of these moments can be found by fitting the normalized mean value ($\mu_i / \sum_{i=n}^n \mu_i$) with a function $f(\langle N_{part} \rangle)$ where $\langle N_{part} \rangle$ is the average number of participant nucleon. The relations are,

$$\mu(\langle N_{part} \rangle) = \Big(\sum_{i=1}^n \mu_i\Big) f(\langle N_{part} \rangle) \Rightarrow \mu \; \alpha \; \langle N_{part} \rangle \tag{3.70}$$

$$\sigma(\langle N_{part} \rangle) = \sqrt{\Big(\sum_{i=1}^n \sigma_i^2\Big) f(\langle N_{part} \rangle)} \Rightarrow \sigma \; \alpha \; \sqrt{\langle N_{part} \rangle} \tag{3.71}$$

$$S(\langle N_{part} \rangle) = 1/\sqrt{\Big(\sum_{i=1}^n 1/S_i^2\Big) f(\langle N_{part} \rangle)} \Rightarrow S \; \alpha \; 1/\sqrt{\langle N_{part} \rangle} \tag{3.72}$$

$$\kappa(\langle N_{part} \rangle) = 1/\left[\Big(\sum_{i=1}^n 1/\kappa_i\Big) f(\langle N_{part} \rangle)\right] \Rightarrow \kappa \; \alpha \; 1/\langle N_{part} \rangle \tag{3.73}$$

It is clear from the above equations that $S\sigma$, $\kappa\sigma^2$ are constant as a function of $\langle N_{part} \rangle$.

3.6.3 Statistical Error Estimation Methods

For any experimental data analysis, there are two types of errors or uncertainties associated with the results: statistical and systematic. Statistical error estimation is one of the most crucial parts of the higher moments analysis for proper interpretation of the results.

There are three types of methods adopted to estimate the statistical errors associated with the higher moments, which are discussed below.

3.6.3.1 Subgroup Method

In Subgroup method, the sample is randomly divided into several subgroups having the same statistics each. Then the calculation of all higher moments is done for each subgroup. Let's say, if there are n number of subgroup created and then the errors on the higher moments are estimated by taking the root mean square of them. This has to be done for each centrality bin.

3.6.3.2 Bootstrap Method

In Bootstrap method, instead of dividing the parent event sample, there are n numbers of clone samples created by random selection from the parent sample with same statistics [115]. This should be done for each centrality bin. Then various moments are calculated. At the end, n values of a particular moments will be obtained. Now the errors of the corresponding moments are obtained by taking the root mean square of those values.

3.6.3.3 Delta Theorem Method

In Delta theorem method, the errors for various order moments are calculated as described in Ref [116], and given as

$$
\begin{aligned}
Var(\sigma) &= (x_4 - 1)\sigma^2/(4n) && (3.74)\\
Var(S) &= [9 - 6x_4 + x_3^2(35 + 9x_4)/4 - 3x_3x_5 + x_6]/n && (3.75)\\
Var(\kappa) &= [-x_4^2 + 4x_4^3 + 16x_3^2(1 + x_4) - 8x_3x_5 - 4x_4x_6 + x_8]/n && (3.76)\\
Var(S\sigma) &= [9 - 6x_4 + x_3^2(6 + x_4) - 2x_3x_5 + x_6]\sigma^2/n && (3.77)\\
Var(\kappa\sigma^2) &= [-9 + 6x_4^2 + x_4^3 + 8x_3^2(5 + x_4) - 8x_3x_5 + x_4(9 - 2x_6) \\
&\quad -6x_6 + x_8]\sigma^4/n && (3.78)
\end{aligned}
$$

where $x_n = m_n/\sigma^n$ and m_n is the n^{th} moment. Now the error of the n^{th} order moments for a wide centrality bin will be,

$$Err(m_n) = \sqrt{\frac{\sum_{i=1}^{N} Var(m_i) n_i^2}{\left(\sum_{i=1}^{n} n_i\right)^2}} \tag{3.79}$$

where N is the total number of bins within that wide centrality range, n_i is the number of events in the i^{th} centrality bin.

Chapter 4

Simulation Study

In heavy-ion collision experiments, the collected data have limited statistics. On top of that the detectors involved in the data taking have limited acceptance and efficiency. That is why we need to have a complete idea of detector inefficiencies on the physics analyses and how to do the correction for the detector effect. This is addressed through the GEANT MC study. In ALICE, depending on physics demand various event generators are used for Monte Carlo (MC) study. The simulated data were generated by taking many event generators like HIJING, AMPT, DPMJET, PYTHIA. For the study of higher moments of net-charge and net-proton distributions, HIJING events are used for MC study. However, producing simulated data of heavy-ion collision events with GEANT is a CPU intensive. So there are only about 1.2×10^6 numbers of good HIJING events for the Pb+Pb collision data at $\sqrt{s_{NN}}$ = 2.76 TeV with 2010 ALICE geometry (Official production name: LHC11a10a_bis). Higher moments analysis is a statistics hungry analysis. Meanwhile, there are limited numbers of HIJING simulated events in ALICE. Hence, it is difficult to have various possible studies, like statistical effect on higher moments, efficiency correction etc. with least statistical uncertainties. Therefore, a toy model is introduced to understand the effect of efficiency and statistics on the higher moments of net-charge and net-protons. The toy model is discussed below for different studies in great details.

4.1 Toy Model

For the toy model study of net-charge (net-proton) number distributions, the N_+ and N_- (p and $\bar{p}$) numbers are the basic ingredients in event-by-event basis. It is already discussed in Section 3.5.1 that the resultant distribution of subtraction of two Poissonian distributions is a Skellam distribution. So evaluation of higher moments of a Skellam distribution is simple and convenient assumption because if the mean values of the individual Poissonian distribution are known, then the mean and other higher moments can be calculated by using Equations 3.50 to 3.55. Meanwhile, by knowing the N_+ and N_- (or p and $\bar{p}$) numbers in event-by-event basis, higher moments can be evaluated as stated in Equation 3.13. Now the first and foremost step is to get the mean numbers of N_+ and N_-. To mimic the event multiplicity of HIJING event generator, the mean numbers of N_+ and N_- are calculated at generator level from 0 to 80$\%$ centrality range by dividing it into 80 bins by taking 1$\%$ centrality bin-width using LHC11a10a_bis data. Those charged particles are taken which fall within the required p_T and η range. Then these mean numbers are used as input in this toy model to generate N_+ and N_- numbers randomly using the Poissonian distribution function event-wise. Now the N_+ and N_- (or p and $\bar{p}$) are understood as total number of positive and negative charged track of an event, respectively. Now according to the requirement of various studies, further sub-steps are implemented at track levels, which will be discussed in the subsequent sections. At the end of event and track generation, all information are stored event-wise. As stated earlier, the mean numbers of N_+ and N_- (or p and $\bar{p}$) are taken from HIJING for 80 centrality bins. Now instead of saying centrality bin, they are referred as “multiplicity bin” throughout this toy model study. Then higher moments are calculated for each multiplicity bin. The final values of higher moments are calculated in wider bin (10$\%$ bin width) using centrality bin width correction (CBWC) method. Here the final results are further classified into 8 multiplicity classes, e.g. 70-80$\%$ multiplicity bin corresponds to multiplicity class 1, 60-70$\%$ multiplicity bin corresponds to 2 and 0-10$\%$ corresponds to multiplicity class 8. The statistical uncertainties are calculated using Delta Theorem as discussed in Section 3.6.3.3.

4.1.1 Higher Moments of Net-charge Distributions

In this section, the effect of event statistics, detector effect and contaminations on the higher moments of net-charge distributions are studied. They are discussed below.

4.1.1.1 Event statistics

In order to check the effect of event statistics on the results of higher moments and their statistical uncertainties, five sets of events with different statistics are generated. Figure 4.1 (a) represents the mean of the net-charge distribution verses multiplicity classes for different statistics. The figure suggest that within error bars, mean is almost independent of event statistics above

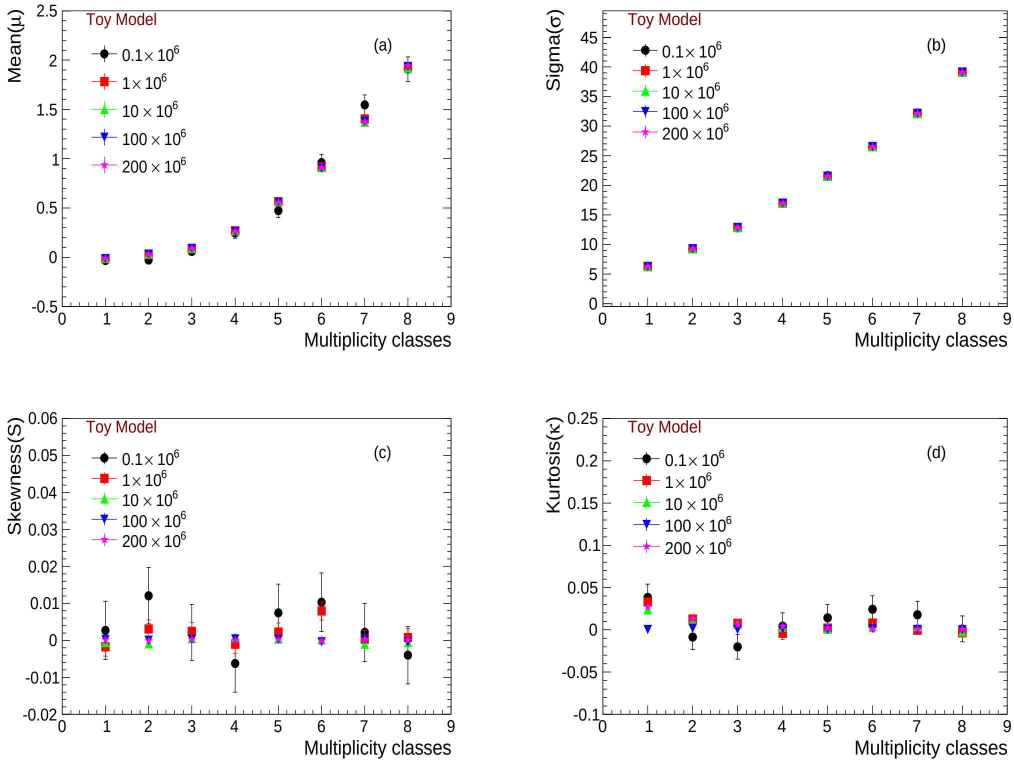

Figure 4.1: Event statistics dependence of (a) mean, (b) sigma, (c) skewness and (d) kurtosis values of net-charge distributions at different multiplicity classes (toy model study).

1×10^6 events per multiplicity class are taken. In Figure 4.1 (b), sigma of the net-charge distribution as a function of multiplicity classes suggests that the width of the

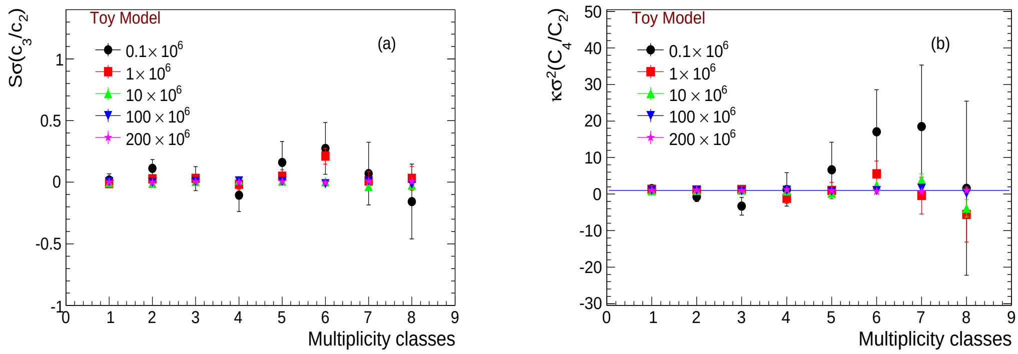

Figure 4.2: Event statistics dependence of (a)$S\sigma$ and (b)$\kappa\sigma^2$ values of net-charge distributions for different multiplicity classes (toy model study).

net-charge distribution is independent of event statistics. Figure 4.1 (c) and (d) represent the skewness and kurtosis as a function of multiplicity classes. The skewness and kurtosis are oscillating in nature and it decreases with increasing statistics. Their values become almost same in all multiplicity classes when more than 100×10^6 events are taken. Similarly, as shown in Figure 4.2 (a) and (b), oscillating behavior of $S\sigma$ and $\kappa\sigma^2$ values are also approaching saturation over all the multiplicity classes for more than 100×10^6 events. The solid line of panel (b) in Figure 4.2 corresponds to $\kappa\sigma^2 = 1$ which is equal to the expectation value of Skellam distribution. It is also observed that the $\kappa\sigma^2$ values are equal to one only at very high statistics of more than 100×10^6. But even after taking 200×10^6 numbers of events per multiplicity class, still the statistical error bars of $S\sigma$ and $\kappa\sigma^2$ are of 50$\%$ of their value. This study clearly indicates that as we go for higher order moments and their ratios, we need very large number of events, at least on the order of 500×10^6 per multiplicity class.

4.1.1.2 Detector efficiency

Due to finite detector efficiency there is always a finite probability of recording or missing a track during data taking and reconstruction. So a study is done to check what is/are the effect(s) of detector inefficiency to the measurement of higher moments of net-charge and net-proton number distributions. In this toy model, we get N_+ and N_- numbers randomly using the Poissonian distribution function event-wise. They are treated as the total numbers of positive and negative tracks of that event at generator level and are called generated tracks. Now using the real p_T distributions of the tracks in HIJING, p_T are assigned to those tracks randomly. Same flat reconstruction efficiency are applied to both positive and negative tracks as a function of p_T. They are called as reconstructed tracks. Now the generated tracks and reconstructed tracks are stored on event-by-event basis. In the mean time, an argument is placed to conclude whether we can do an event-wise or track-wise detector efficiency correction for higher moments analysis or not. These scenarios are discussed in the following subsections.

- **Event-wise detector efficiency correction:** It is not advisable to do event-wise efficiency correction to sensitive study like higher moments because it may bias the fluctuation on event-by-event basis. However, an attempt is made to go for an event-wise efficiency correction. This method can be validated by comparing the moments results before and after efficiency correction at different multiplicity classes. For simplicity, a flat reconstruction efficiency of 80$\%$ both for positive and negative tracks is used for this study. The average reconstruction efficiency (ϵ) at event level is calculated for each multiplicity bin by taking the division of average number of reconstructed (positive or negative) tracks to average number of generated tracks. Then to do efficiency correction, ϵ is multiplied with the total reconstructed tracks for each events of the whole event sample. So in total, there are three sets of results of higher moments from this toy model: (i) higher moments of the generated events, (ii) higher moments of reconstructed events and (iii) higher moments of the reconstructed event with event-wise efficiency correction. The results are shown in Figure 4.3.

  The lower panel of each figure (Figure 4.3) shows the relative difference (R.D) as a function of multiplicity class. The relative difference, R.D. is defined as

$$R.D. = \frac{\text{Generated value} - \text{efficiency corrected value}}{\text{Generated value}} \tag{4.1}$$

  In Figure 4.3 , the blue open circle corresponds to the values for generated events, the red filled circles corresponds to the values from reconstructed events and black

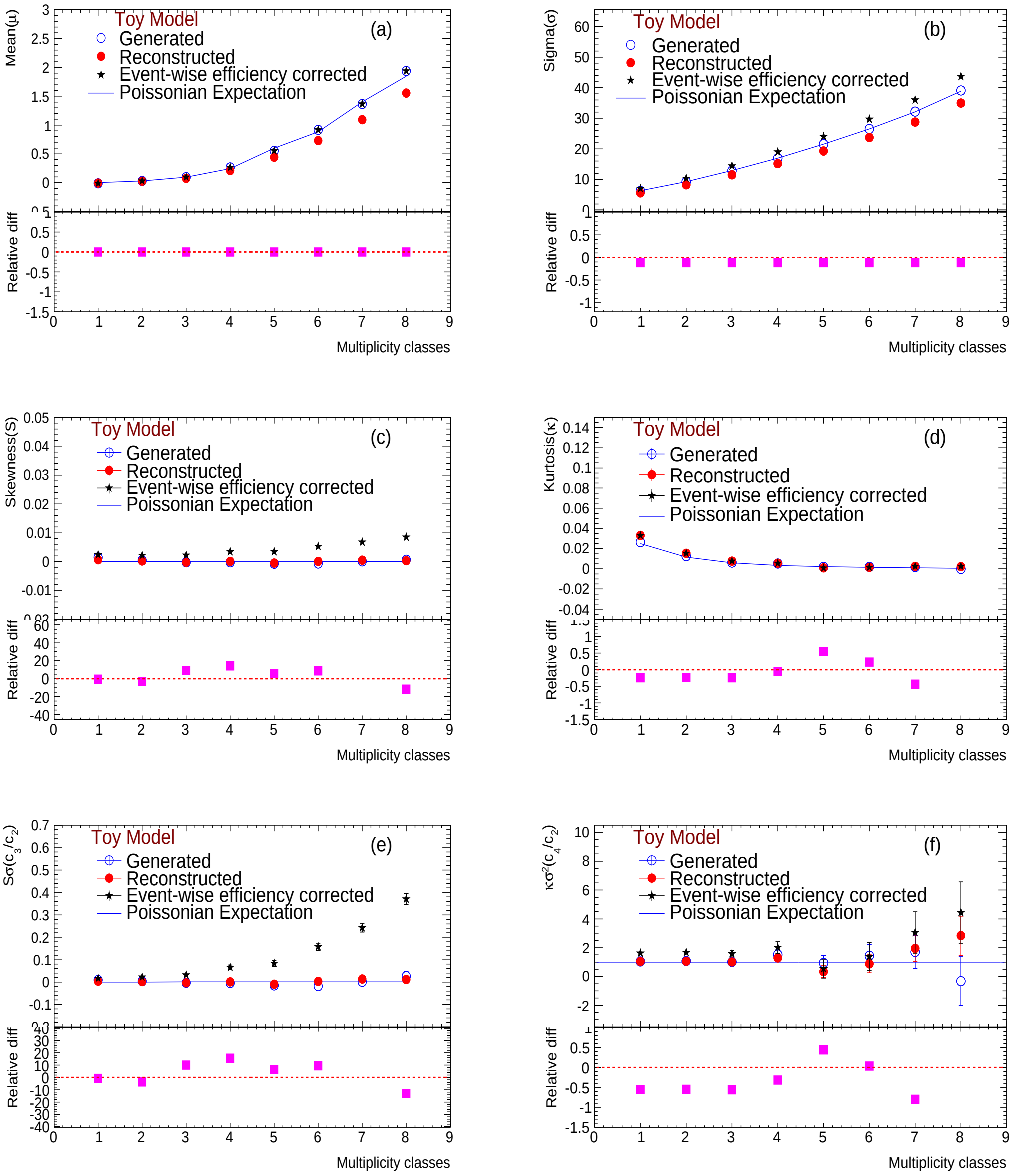

Figure 4.3: Different moments of net-charge distributions for different multiplicity classes of event-by-event basis efficiency correction (toy model study).

star markers corresponds to the values obtained after event-wise efficiency correction to the reconstructed numbers. The solid blue lines are the expected value obtained from Skellam distribution using the Equation 3.50 to 3.55.

The first observation to this study is that there is always substantial effect of detector inefficiency to the nature of net-charge distributions. This is clear from Figure 4.3 that mean, sigma and other higher moments of reconstructed distributions are different from the generated distributions. The second observation is to be made about the event-wise efficiency correction. If the event-wise efficiency correction is an appropriate method, then the R.D. should be ~ 0. It is clear that, except, mean values of the net-charge, the efficiency corrected values are not matching (more than 10% of R.D. and more than 100% for ratio of cumulants) with the generated values. Interestingly, it is observed that the reconstructed values are more closer to the generated values for skewness, kurtosis and the ratio of cumulants. This study shows that it is not possible to do an event-wise detector efficiency corrections for net-charge higher moments analysis.

- **Track-wise detector efficiency correction:** The next toy model study is carried out to see whether it is possible to correct the detector inefficiency for each track in the whole phase space (p_T, η and ϕ) and then to evaluate total positive and negative tracks. The difference of efficiency corrected total positive to total negative charge number gives the efficiency corrected net-charge of that event. At the end of large number of event sample, the higher moments of the net-charge distributions are estimated for these track-wise efficiency corrected numbers. Now these results are called as track-wise efficiency corrected values. The same strategy is adopted for event and track generation, reconstruction as before. The reconstruction efficiency considered for this study is flat as a function of p_T and is 80% for both positive and negative tracks. During the course of efficiency correction to the tracks, each reconstructed tracks are multiplied by a weight factor to correct the reconstruction inefficiency. The weight of a single track determined by taking the inverse of the efficiency of that track according to its p_T. The results are shown in Figure 4.4. In Figure 4.4, the open circle represents the results of generated events, filled red circle represents the reconstructed events and black star marker represents the results of the events with track-wise efficiency correction. It is observed from the 4.4 (a) that the mean value of the generated and track-wise efficiency corrected events of all multiplicity classes are same as the relative difference is close to zero. But in the panel (b) of Figure 4.4 shows that, the width (sigma) of the net-charge distribution is increased after track-wise efficiency correction. For skewness and kurtosis, the

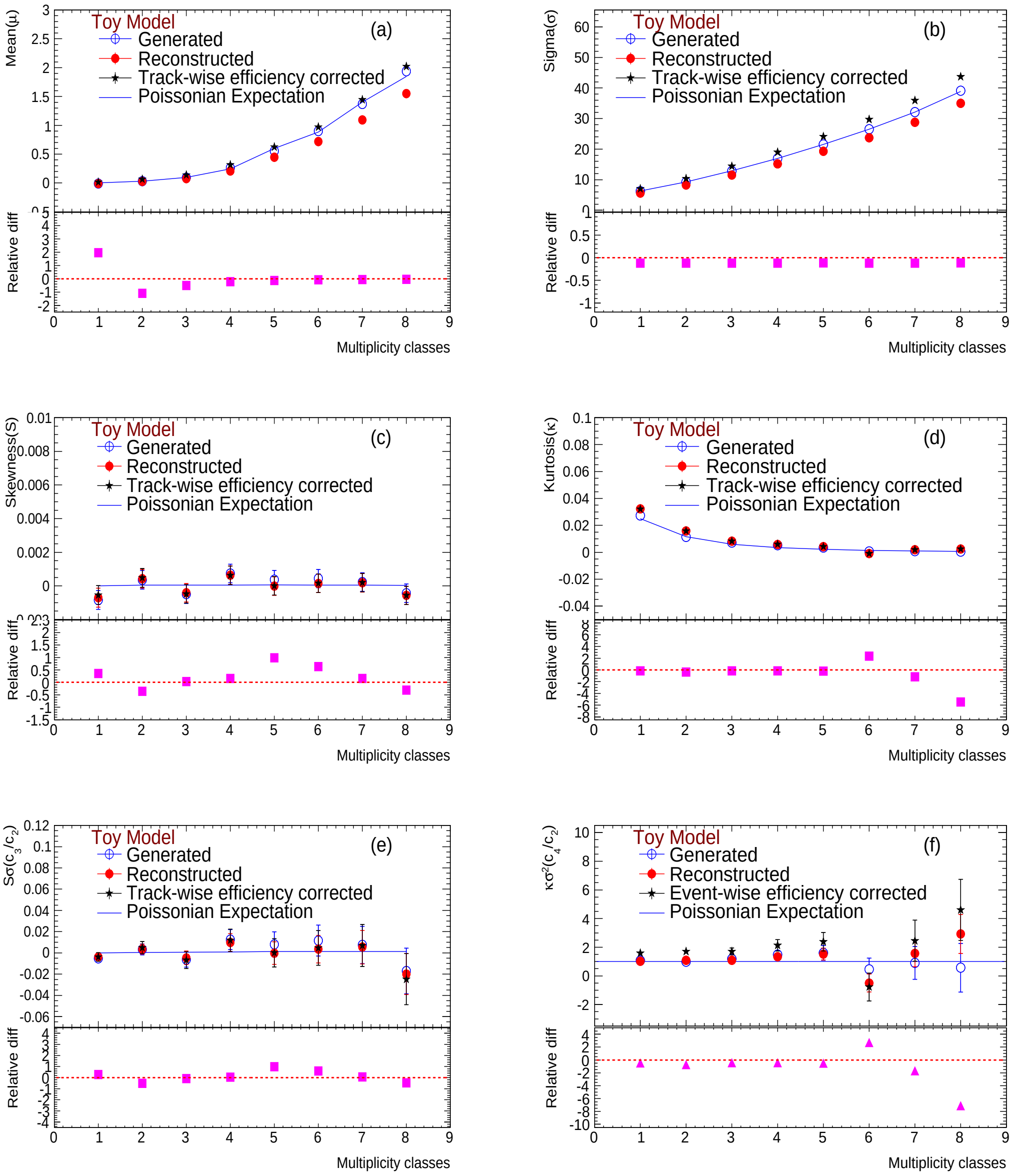

Figure 4.4: Net-charge higher moments results for track-wise efficiency correction (toy model study).

efficiency corrected results are almost same with the reconstructed values and differ from the generated values. The same scenario is true for $S\sigma$ and $\kappa\sigma^2$ results (panel (e) and (f) of Figure 4.4). This study suggests that track-wise efficiency correction can't be used to correct the detector effect to get back the higher moments of net-charge distributions except for mean values.

4.1.1.3 Contamination

During track reconstruction, there is some probability that a secondary track can be considered as a primary track. These tracks are called as contamination to the primary tracks. This toy model study is carried out to see the effect of contamination to the higher moments results of net-charge distributions. In this toy model, two cases of contaminations are taken: one with flat 2% of contamination and another with flat 5% contamination for each multiplicity bin.

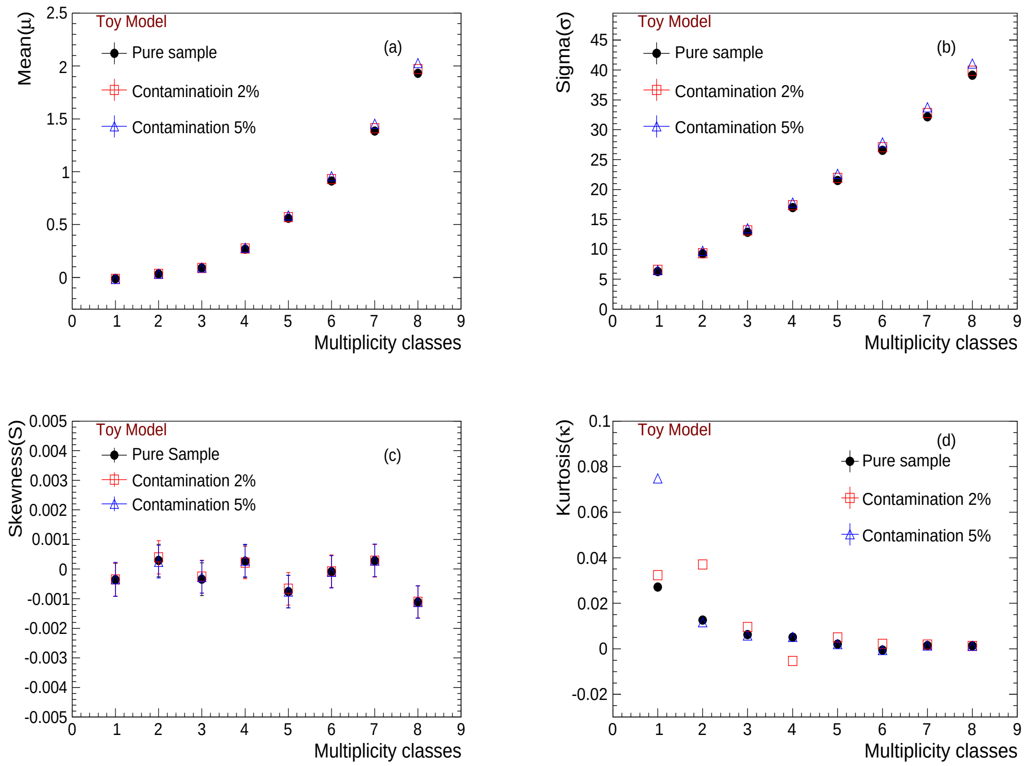

Figure 4.5: Effect of contamination on the (a) mean, (b) sigma (c) skewness and (d) kurtosis of net-charge higher moments in eight multiplicity classes (toy model study).

In Figure 4.5 and 4.6, the filled black markers are the results from pure sample (generated events), the open square represents the sample which have 2% contamination and the open triangle represents the result for the event sample with 5% contamination. In Figure 4.5 (a), it is observed that the mean values of the higher multiplicity classes is slightly increased when the contamination is added and it increases with increase of contamination. The effect of contamination is less in low multiplicity event classes. The similar observation is also made for the width of the net-charge distribution of Figure 4.5 (b). The skewness values of the contaminated and pure events are within the error bars and the effect is negligible. In the case of kurtosis, the effect of contamination is substantial in the first four low multiplicity classes and more prominent in case of 2% contamination and then it is almost same for last two higher multiplicity classes. In Figure 4.6 (a), again it is observed that the contaminated sample and pure sample has almost same $S\sigma$ values. Only the $\kappa\sigma^2$ values of the sample with 2% contamination largely differ from the pure sample, otherwise, the 5% contamination sample has same values with the pure sample (Figure 4.6 (b)). Hence, it is concluded that there is always some effect of contamination to the results of net-charge higher moments.

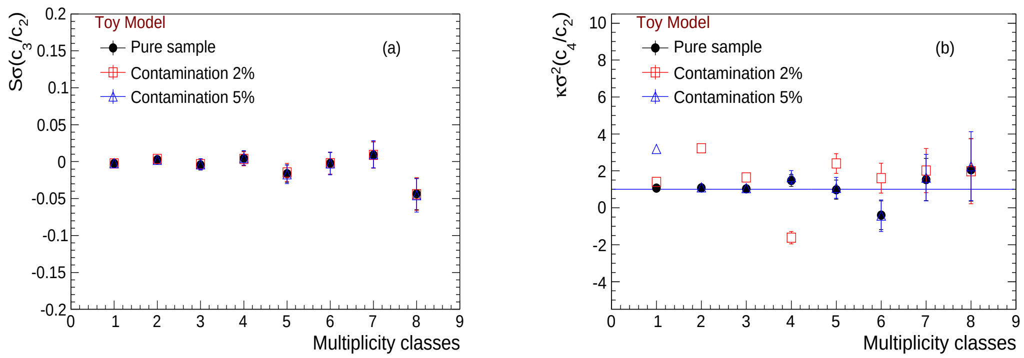

Figure 4.6: Effect of contamination on the ratio of cumulants of net-charge higher moments in eight multiplicity classes (toy model study).

4.1.2 Higher Moments of Net-proton Distributions

In this section, the effect of event statistics, detector effect and contaminations on the higher moments of net-proton distributions are discussed.

4.1.2.1 Event statistics

The dependence of results of higher moments of net-proton distributions on event statistics are studied. The procedure is exactly same as described in Section 4.1.1.1. Here instead of N_+ and N_-, the p and $\bar{p}$ numbers are taken from HIJING. The results of five sets of event statistics are studied in eight multiplicity classes. The results are shown in Figure 4.7 and Figure 4.8. It is observed from Figure 4.7 that the mean values of the lowest event statistics (black diamond marker) has larger statistical uncertainties and different from the other four sets of statistics. The mean values become same when more than 1×10^6 events are taken per multiplicity class. Like net-charge higher moments, the sigma values are same irrespective of number of events. The skewness, kurtosis of Figure 4.7 and $S\sigma$, $\kappa\sigma^2$ values of Figure 4.8 are oscillating from one multiplicity bin to the other and error bars are very large when statistics is low. When statistics reaches at 100×10^6 of events per multiplicity bin, then their values are not changing so much and the statistical uncertainties are very small and of the order of 10%. This study shows that, for net-proton analysis, around 100×10^6 of events are required for each multiplicity bin. Another observation is made from this toy model study that one can achieve a small statistical uncertainty with less statistics for the higher moments of net-proton compared to net-charge. This is because, the statistical error also depends on the value of the σ of the net-charge or net-proton distribution. This study clearly indicates that for net-proton and net-charge higher moments analysis, very large event statistics are required.

4.1.2.2 Detector efficiency

To study the detector effect on net-proton higher moments results, another set of toy model study is carried out. The event generation, the reconstruction of tracks and analysis procedure are same as the previously discussed method in section 4.1.1.2. The results are discussed below.

- **Event-wise detector efficiency correction:** The event-wise efficiency correction is done same as the net-charge higher moments toy model analysis. The results of mean, sigma, skewness, $S\sigma$ and $\kappa\sigma^2$ are shown in Figure 4.9 and 4.10. In Figure 4.9 and 4.10, the blue open circle represents the values for generated events, the red filled circles are the values from reconstructed events, black star marker represents the values obtained after event-wise efficiency correction to the reconstructed numbers. The solid blue lines correspond to the expected value obtained from Skel-

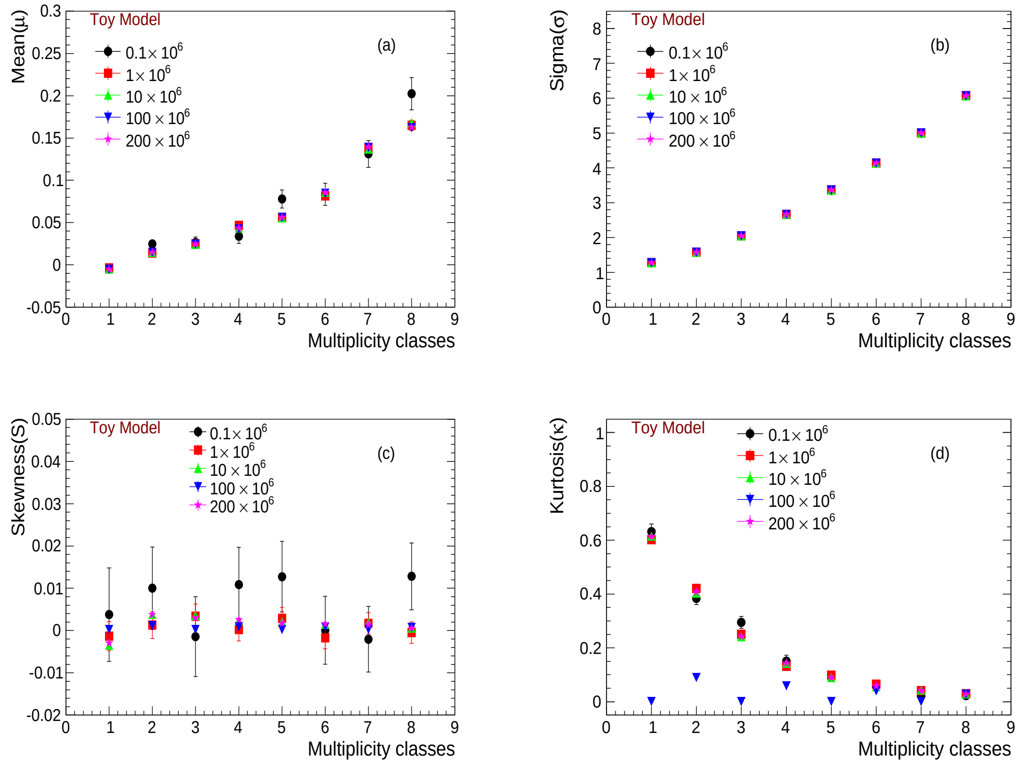

Figure 4.7: Dependence of (a) mean, (b) sigma, (c) skewness and (d) kurtosis of net-proton distributions at eight different multiplicity classes on event statistics (toy model study).

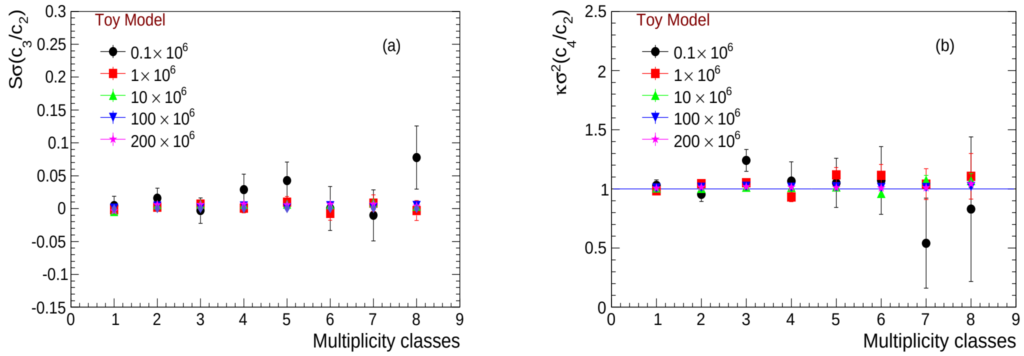

Figure 4.8: Dependence of (a) $S\sigma$ and (b) $\kappa\sigma^2$ of net-proton higher distributions at eight different multiplicity classes on event statistics (toy model study).

lam distribution. Again it is clear from the Figure 4.9 that only mean value can be corrected back by this method and others are not. In contrast to net-charge toy

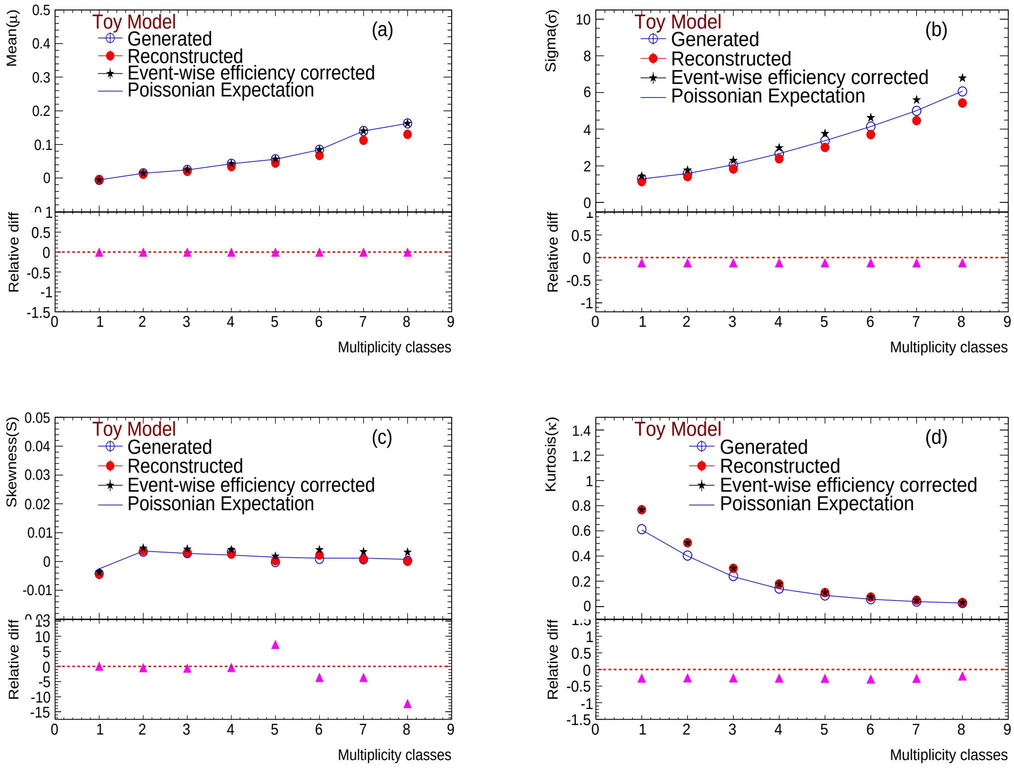

Figure 4.9: (a) mean, (b) sigma, (c) skewness and (d) kurtosis of net-proton distributions for different multiplicity classes of event-by-event basis efficiency correction (toy model study).

model study, it is observed from Figure 4.10 (a) and (b) that the generated and reconstructed values are almost same when the ratio of cumulants (e.g. $S\sigma$ and $\kappa\sigma^2$) are taken. However, the efficiency corrected value of $\kappa\sigma^2$ is far above the generated value in all multiplicity classes. Now it is clear that event-wise efficiency correction is also not working for net-proton higher moments analysis.

- **Track-wise detector efficiency correction:** The same strategy which was used for the net-charge toy model analysis in Section 4.1.1.2 is adopted to test whether the track-wise efficiency correction works for net-proton higher moments analysis or not. The generated events, the reconstructed events and the events with track-wise efficiency correction are studied and the results are shown in Figure 4.11.

  In Figure 4.11 the open circle represents the results of generated events, filled red circle is for reconstructed events and black star marker represents the results of the

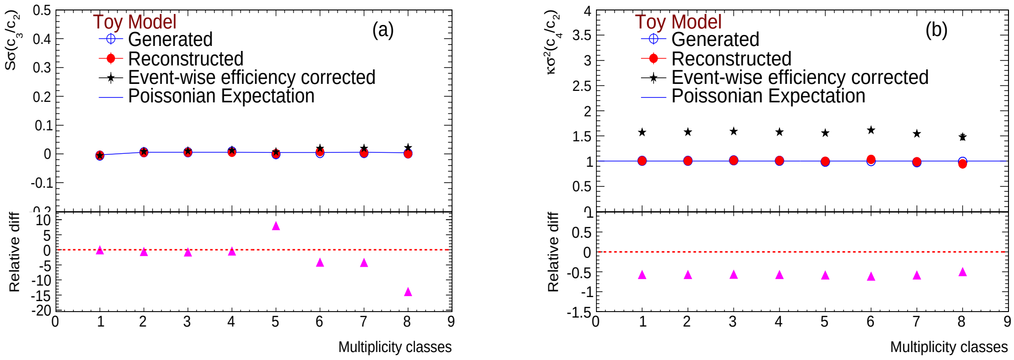

Figure 4.10: (a) $S\sigma$ and (b) $\kappa\sigma^2$ of net-proton distributions for different multiplicity classes of event-by-event basis efficiency correction (toy model study).

events with track-wise efficiency correction. Figure 4.11 (a) shows that the mean values of track-wise efficiency corrected sample of the higher multiplicity classes are not matching with generated values. The sigmas of all multiplicity classes are increased after doing the track-wise efficiency correction. But the skewness and kurtosis values of efficiency corrected events towards the higher multiplicity classes are almost same with the generated and reconstructed values. But it can be seen from panel (e) and (f) that in $S\sigma$ and $\kappa\sigma^2$ results, the efficiency corrected values are not matching with the generated values which is clear from their relative differences. So the similar conclusion is drawn from this toy model study that track-wise efficiency correction is not a good method of doing detector efficiency correction for net-proton higher moments analysis.

4.1.2.3 Contamination

For net-proton higher moments analysis, there are two types of contamination. First is the secondary track and second one is the weak decays. This toy model study is carried out to see the effect of contamination to the higher moments of net-proton distributions similar to the way discussed in Section 4.2.3. The results are shown in Figure 4.12 and Figure 4.13.

In Figure 4.12 and 4.13, the filled black markers are the results from pure sample (generated events), the open square represents the sample which have 2% contamination

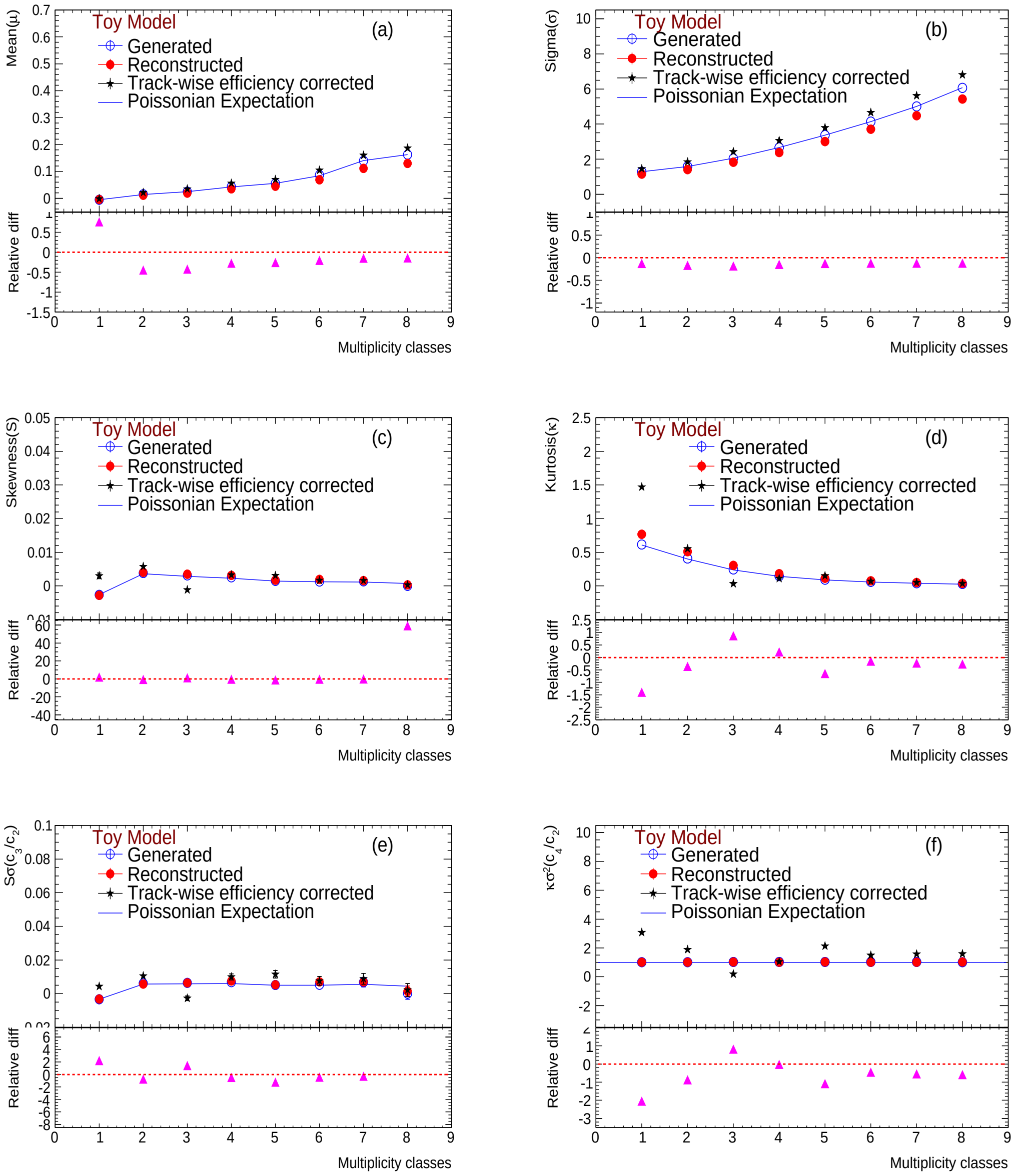

Figure 4.11: Results for net-proton higher moments in track-wise efficiency correction (toy model study).

and the open triangle represents the result for the event sample with 5% contamination. Here also, the mean and sigma values are increased due to the contamination and it is more for higher multiplicity classes. The skewness and kurtosis values of sample with 2% contamination is deviating more than the 5% contaminated sample. The reason is not clear as far as this toy model is concerned. But unlike net-charge, the $S\sigma$ and $\kappa\sigma^2$ values are deviating from the pure sample and the deviation is random in case of $S\sigma$, but

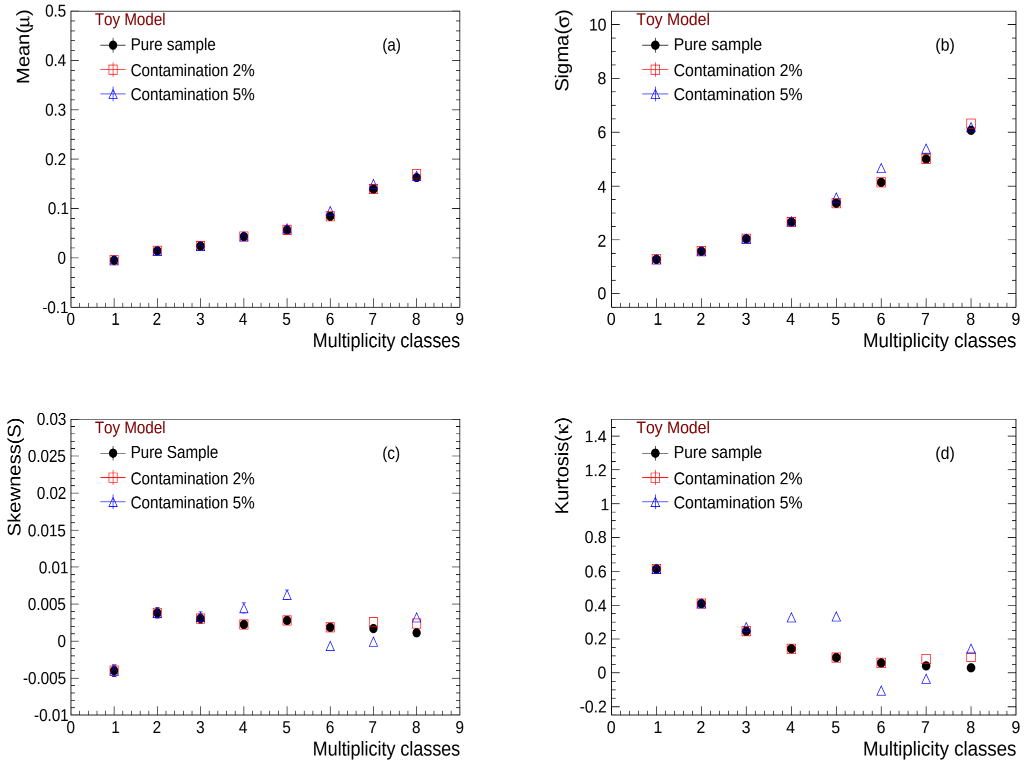

Figure 4.12: Effect of contamination on net-proton higher moments (toy model study).

systematically increased in case of $\kappa\sigma^2$ for high multiplicity classes. So this toy model study shows that there are substantial changes in the values of the higher moments of net-proton distributions because of contamination. Hence, it is necessary to reduce the contamination level as much as possible during the data analysis.

4.2 Proposed Methods for Detector Efficiency Correction for Higher Moments

A conclusion drawn from the toy model study discussed in the previous section about the main concern of higher moments analysis is that neither event-wise nor track-wise efficiency correction works. So those methods are discarded so far this analysis is concerned and looked for other alternative possible methods to remove the detector effects from the data to extract the relevant physics message. Here are few methods proposed recently

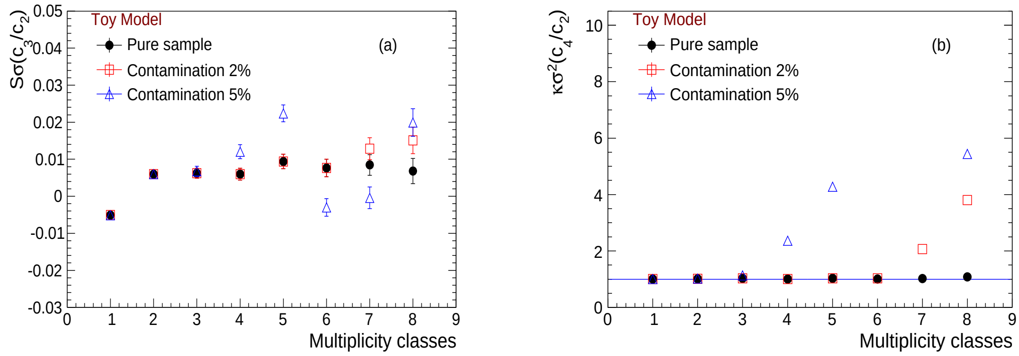

Figure 4.13: Effect of contamination on net-proton higher moments (toy model study).

by various authors for detector efficiency corrections which are discussed below with toy model study to see the feasibility for higher moment analysis.

4.2.1 Unfolding Method

Unfolding method is widely used in various analyses of heavy-ion collision experiments to correct the detector effect [117–119]. First time in [120], it is proposed that unfolding method can be used to eliminate the known detector inefficiency while studying the higher moments of net-charge and net-proton distributions from collision data. This method uses the basics of Bayesian unfolding method first proposed by G. D'Agostini [121]. Unfolding can be done using the software tool called as RooUnfolding [122]. Bayesian unfolding method is used to remove the known effect of measurement resolutions, detector inefficiency and systematic biases from the measured distributions (data) to get the true distribution. Basically it uses a response matrix to encode the known effects, which can be determined by MC simulation where both the true distributions and measured distributions are known. Then later on this response matrix is used to unfold the data. Detail descriptions of Bayesian unfolding method and algorithm of RooUnfolding are given in Ref [121, 123]. In this toy model, the procedure given in Ref [120] is followed for this study. In Ref [120], HIJING event generator is used, whereas in this thesis the toy model is used. In Ref [120] , it is shown that the true or generated values of higher moments of net-charge and net-proton distributions can be faithfully unfolded back by using Bayes method. However, a drawback of their method is pointed out during this toy model study. The drawback in their method is that they have used HIJING events as training sample as well as for unfolding where the multiplicity is same in both the cases. In this toy model, an attempt is made to address this drawback by showing that event generators with different multiplicities can not be used for successful unfolding of all the higher moments. Here, two cases are considered in the present context of argument. In the first case, the events with same mean of N_+ and N_- are used for training as well as unfolding sample. In the second case, the unfolding sample is different from the training sample. The detector efficiency is kept same for both the cases. Here, the results of unfolding is shown for both the cases in Figure 4.14 and Figure 4.15, respectively.

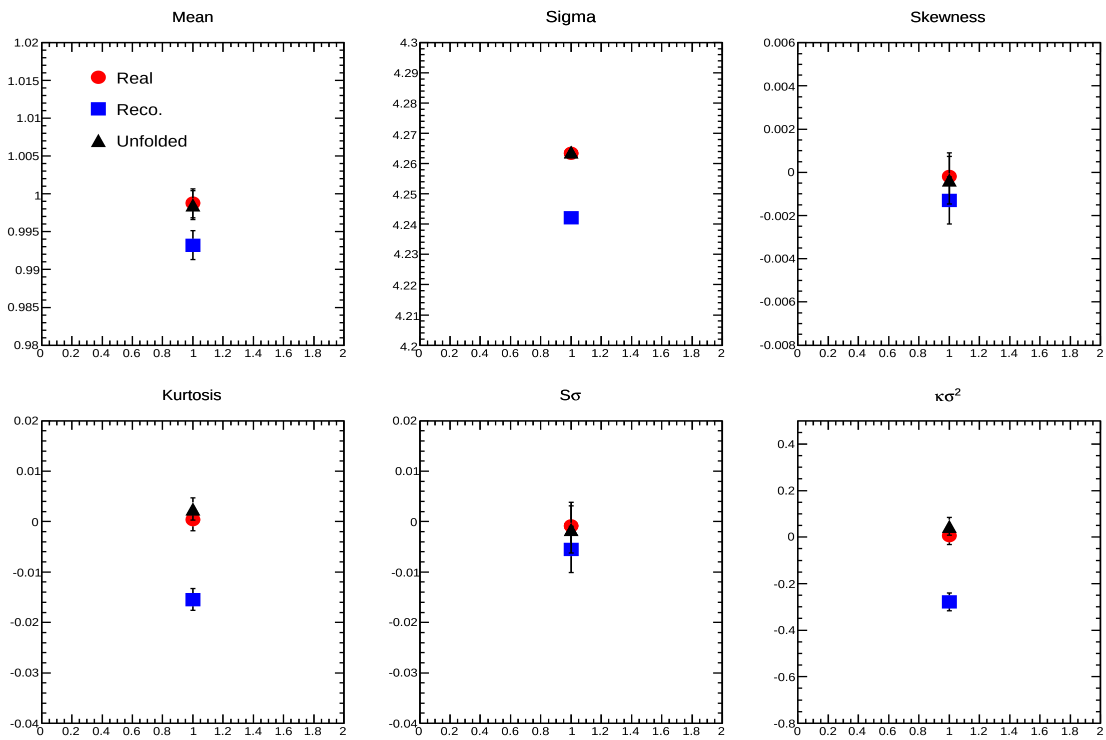

Figure 4.14: Unfolding results with event sets of same multiplicity used for training and unfolding (toy model study).

In Figure 4.14, the red filled circles are the moments value from the generated or real events, blue squares represent the moments value of the reconstructed events and black triangles are for the moments value obtained from the unfolded events. It is clear from Figure 4.14, when the events sample whose mean of the event multiplicity ($< N_+ >=$

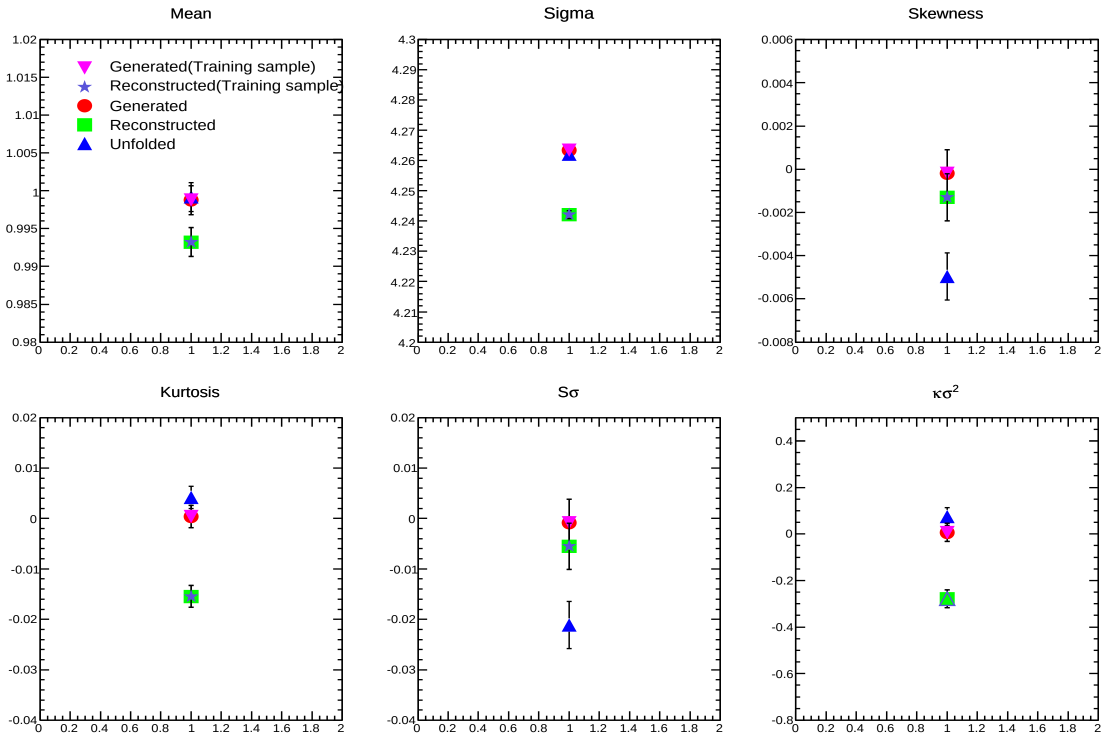

Figure 4.15: Unfolding results with two type of events with different multiplicity used for training and unfolding, respectively (toy model study).

$50, < N_- >= 50)$ is same as the events taken for training; the mean, sigma and other higher moments of the distributions are successfully unfolded back to the generated values. The results for the second case is shown in Figure 4.15. In Figure 4.15, the inverted triangles of magenta colors are the moments value of the generated events used for training, star markers for the moments values of the reconstructed events of the training sample. The red filled circles are of the generated events, the green square markers of reconstructed events and the blue triangles are the moments value for unfolded events for the event sample whose multiplicity is different from the training sample. It can be seen in Figure 4.15 that the generated and reconstructed values of all the higher moments of both type of event samples are same. This ensures the credibility of the toy model chosen to test the validity of the study reported in Ref [120]. It is observed in this study that when a different kind of event samples, whose mean values ($< N_+ >= 51, < N_- >= 50$) are slightly different than the training sample, are used for unfolding, only mean and sigma of the distributions are unfolded back successfully, but not the other higher moments. This can be observed in Figure 4.15. This conclusion is made from Figure 4.14 and 4.15 that even if the detector effect is same for both the events sample with different multiplicities, RooUnfolding method is unsuccessful to unfold back to the higher moments to the true distribution. It implies that, while using unfolding method to correct the detector effect, we need a model for training whose mean number of positive and negative charged particles (the multiplicity) of the events, particle ratios, p_T spectra etc, should be same as the real data. This is also mentioned in [121]. The HIJING event generator doesn't describe the experimental data well. So one has to be very careful to implement the unfolding method to real data by taking HIJING events as training sample. From this simple toy model study, it is concluded that this unfolding method can't be used to correct the detector effect for the higher moments and cumulants study of net-charge and net-proton distributions with the present available event generators.

4.2.2 K-cumulants Methods Using Factorial Moments

This method is proposed in Ref [124]. The binomial probability distribution is used to model the correction methods and

$$\begin{aligned} p\left(n_1, n_2\right) = \sum_{N_1=n_1}^{\infty} \sum_{N_2=n_2}^{\infty} P\left(N_1, N_2\right) \frac{N_1!}{n_1!(N_1-n_1)!} p_1^{n_1} \left(1-p_1\right)^{N_1-n_1} \\ \times \frac{N_2!}{n_2!(N_2-n_2)!} p_2^{n_2} \left(1-p_2\right)^{N_2-n_2} \end{aligned} \tag{4.2}$$

where $p(n_1, n_2)$ describes the probability distribution of the measured particles n_1, n_2 and $P(N_1, N_2)$ is the probability distribution of the generated particles N_1, N_2. The parameters p_1 and p_2 take care of the detector efficiency. The subscript "1" and "2" represent the positive and negative particles, respectively. In this method, factorial moments is used in a convenient way to connect them with the generated and measured (reconstructed) probability distributions as given in equation 4.3 and 4.4.

$$F_{ik} \equiv \langle \frac{N_1!}{(N_1-i)!}\frac{N_2!}{(N_2-k)!}\rangle = \sum_{N_1=i}^{\infty}\sum_{N_2=k}^{\infty} P(N_1,N_2)\frac{N_1!}{(N_1-i)!}\frac{N_2!}{(N_2-k)!} \quad (4.3)$$

$$f_{ik} \equiv \langle \frac{n_1!}{(n_1-i)!}\frac{n_2!}{(n_2-k)!}\rangle = \sum_{n_1=i}^{\infty}\sum_{n_2=k}^{\infty} p(n_1,n_2)\frac{n_1!}{(n_1-i)!}\frac{n_2!}{(n_2-k)!} \quad (4.4)$$

$F_{i,k}$ and $f_{i,k}$ are the factorial moments of generated and measured numbers, respectively. Then a relation between the generated and measured factorial moments can be established as follows.

$$f_{i,k} = p_1^i.p_2^k.F_{i,k} \quad (4.5)$$

For simplicity, the formula to correct the measured cumulants when the detector efficiency of both positive (p) and negative ($\bar{p}$) charged tracks are same (i.e. $p_1 = p_2$) is deduced and later more generalized formulae of the corrected cumulants denoted as K_n in the appendix of Ref [124] in terms of various factorial moments are given. To test this method, a toy model study is carried out by considering several cases. First the binomial efficiency type is considered and it is done only for a single centrality class of highest multiplicity bin of net-proton and net-charge. The probability in the binomial function used for positive particles and negative particles are 80$\%$ and 79$\%$, respectively. This probability is basically the efficiency of the detector. This p_1 and p_2 are the average efficiency of the detectors for positive and negative particles, respectively, which can be evaluated from this toy model as follows.

$$\text{Average Efficiency} = \frac{\text{Average number of measured positive (negative) charge tracks}}{\text{Average number of generated positive (negative) charge tracks}} \quad (4.6)$$

The toy model results for net-proton and net-charge are presented in Figure 4.16 and Figure 4.17, respectively. In Figure 4.16 and 4.17, the red marker represents the moments values of generated events, the square marker represents the value obtained from measured events and blue triangle marker is for the moments results after doing the efficiency correction using K-cumulant method. For both the cases, it can be seen that the corrected mean and sigma values of net-proton and net-charge distributions match with the gener-

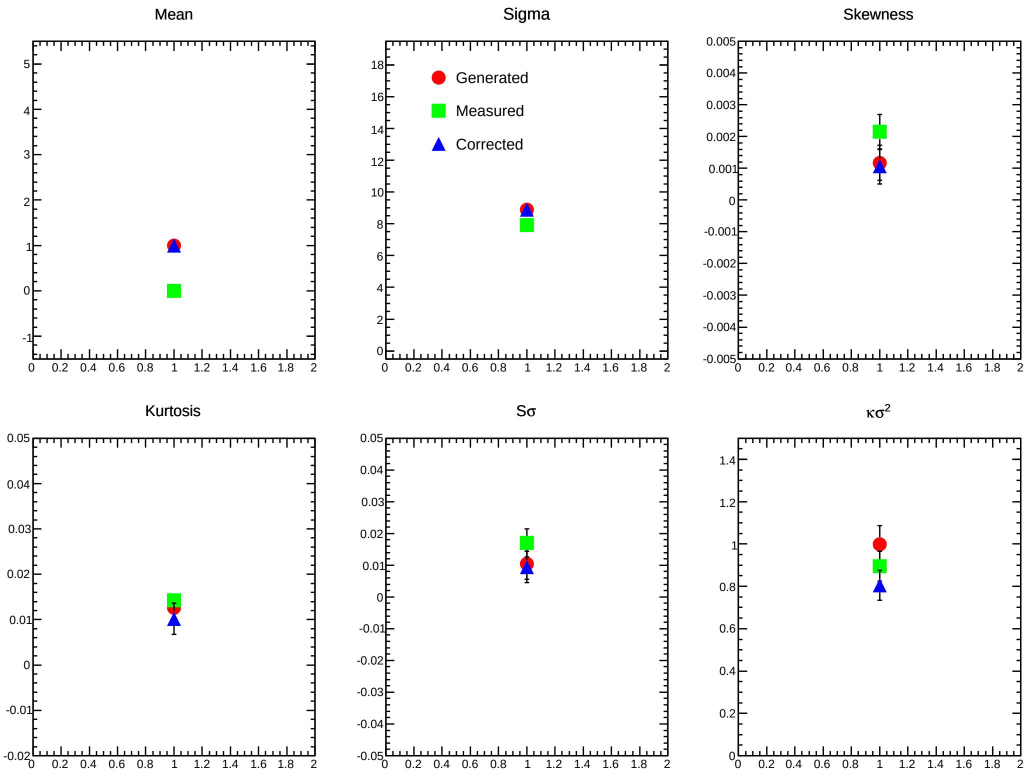

Figure 4.16: Efficiency corrected results of net-proton higher moments compared with the generated and reconstructed values using the K-cumulant method considering detector efficiency as binomial type (toy model study).

ated values. In Figure 4.16, except $\kappa\sigma^2$, the corrected values of skewness, kurtosis and $S\sigma$ are close to generated values. However, it is observed in Figure 4.17 that skewness, $S\sigma$ and $\kappa\sigma^2$ do not match with the generated results except kurtosis. This disparity from net-proton to net-charge results can be inferred as follows. While correcting small numbers (e.g. p and $\bar{p}$ numbers are around 40 each in most central collisions) with some factor, the small uncertainties in the correction factor may not make such change in the final results, but if you consider higher numbers (e.g for net-charge, the number of positive and negative tracks are around 900 each in most central collisions), even a 0.1$\%$ of uncertainties in correction factor can make a large difference. However, to be sure about the earlier observations, a more extensive toy model study for net-charge for all eight centrality classes is done which is given in Figure 4.18. In this study, total 160×10^6 numbers of events are taken (each centrality bin has 2×10^6 events). The reconstruction efficiencies used are

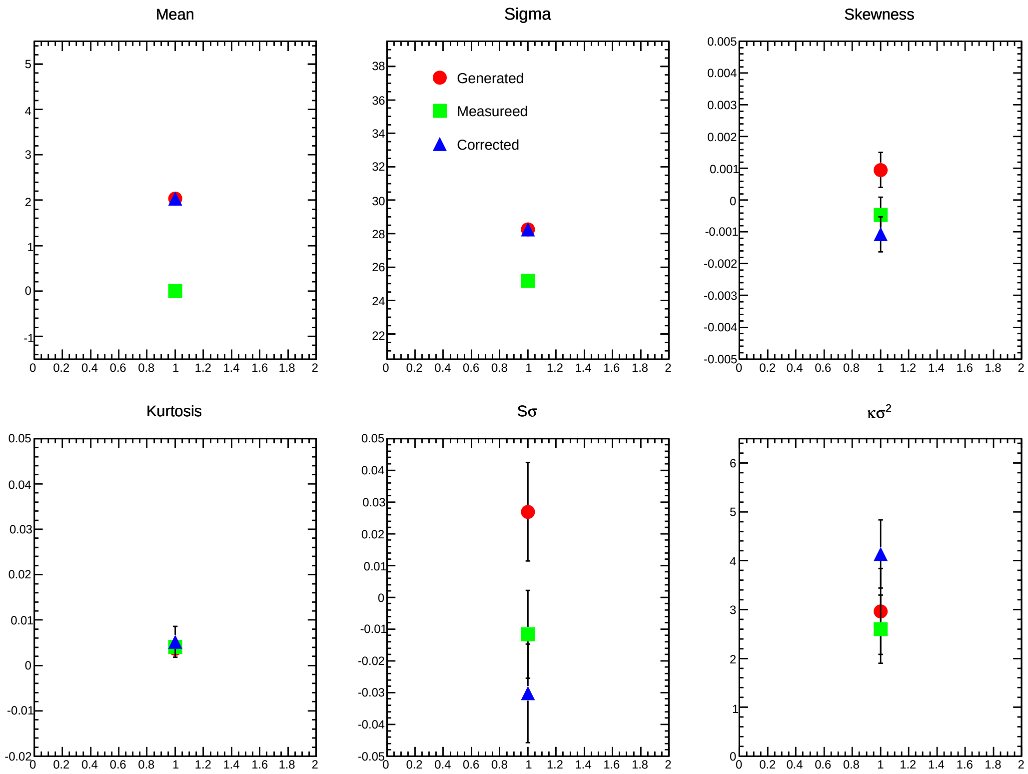

Figure 4.17: Efficiency corrected results of net-charge higher moments compared with the generated and reconstructed values using the K-cumulant method considering detector efficiency as binomial type (toy model study).

80% and 79% for positive and negative tracks, respectively.

In Figure 4.18, the red marker represents the moments values of generated events, the square marker represents the value obtained from measured events. The blue triangle marker is for the moments results after doing the efficiency correction using K-cumulant method. The lower panel of each figure is the ratio of corrected value to the generated values for eight centrality classes. It is observed that the mean and sigma values are corrected back to the generated values. For other higher moments and ratio of cumulants, the corrected values are more closer to the generated values. But the difference goes on increasing while moving from lower multiplicity class to the higher multiplicity class. It is also hard to conclude for the other higher moments, as the error bars are so large. This method has one drawback that it uses an average efficiency for each centrality class for correction. But in real, the detector efficiency varies with respect to p_T, η and ϕ of

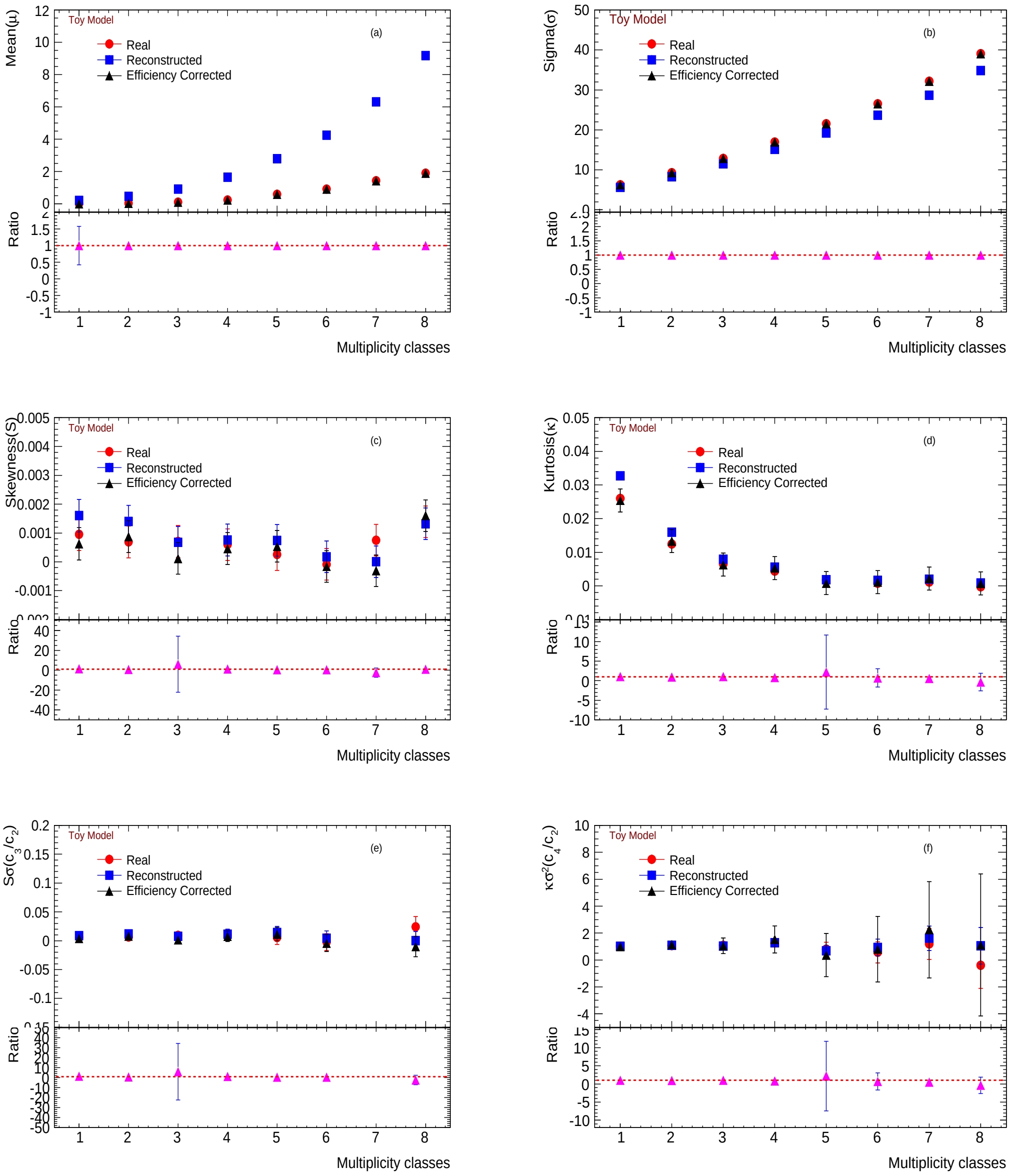

Figure 4.18: Net-charge higher moments using K-cumulants efficiency correction method (toy model study).

tracks. Recently, the same authors have proposed another method to correct the detector effect over all the phase space and is called as method of local efficiency correction to the cumulants [125]. This method is under study.

Chapter 5

Results and Discussion

The technicalities involved in collecting the data are discussed in details in Chapter 2. After passing through a lot of quality checks, the data are stored in a data container with all the global and individual track information of each event. Depending on the physics analysis, all desired selection criteria are applied to data. Sensitive analysis, like the study of fluctuations of conserved numbers, i.e. net-(electric) charge and net-proton, needs to be done with greater care. The detector effects are studied through MC simulation. The dataset, event and track selection methods for this analysis will be discussed in this chapter. Then the results of the measurements of net-charge and net-proton number fluctuations are discussed.

5.1 Data Analysis Procedures

The measurement of higher moments of net-charge and net-proton distributions are carried out taking Pb-Pb collision data of first LHC heavy-ion run in year 2010. The reconstructed events of the collision data are available in terms of ESD and AOD for physics analysis. Starting from event selection from AODs to the moments estimation procedures and systematic studies are discussed below.

5.1.1 Event Selection

In heavy-ion collision experiment, an event is defined as the collision between projectile and target nuclei. During the experiment, events are recorded by assigning certain trigger depending on the threshold defined for the trigger detectors. To select an event, first a trigger selection cut is used. Then to avoid background events and secondary interactions, vertex cuts are applied. In the mean time, the centrality of the event is determined. In this section, different event selection criteria are discussed.

5.1.1.1 Trigger selection and Background Event Rejection

In ALICE, there are different types of triggered events. For this analysis, events with minimum-bias triggers are used. Minimum-bias (MB) trigger implies that it imposes minimum or virtually no bias while selecting an event. A MB trigger satisfies two requirements out of the following three requirements during the data taking: (a) hits in the outer SPD layer, (b) signal in V0A and (c) signal in V0C. Technically, it is represented as **"CMBACS2-B-NOPF-ALL"**. The first part of the phrase is the basic trigger condition plus the information from LHC which confirms that there was bunch crossing ('B'). 'NOPF' stands for 'No Past-Future Protection' (past-future protection is used to avoid those events which are superimposed by too many pile-up collisions) and the last part stands for the active trigger detectors. The main detectors used for MB trigger are VZERO and SPD. The MB trigger has large efficiency for low multiplicity and diffractive events and has good rejection of background interactions.

Apart from real collisions, there is also some probability of interaction of beam with residual gas inside the beam pipe and may give a MB trigger. There is also another scenario of beam-halo interactions, which can fire a MB trigger. The halo is the gas of charged particles which are created after continuous collisions. To eliminate such events originating from beam-gas or beam-halo interactions, certain triggers are used in ALICE. This is decided by VZERO detector with the fact that the arrival times of particles to V0A and V0C are different in beam-beam and beam-gas interactions. Particles coming from real collisions will hit V0A after 11.4 ns of the time at which both the beam coming from opposite directions cross the nominal interaction point in ALICE [126]. But the particles generated from background events will arrive V0A and V0C at significantly different times. There are also some soft particles produced via QED processes due to strong electromagnetic fields generated by the relativistic heavy-ions. These QED processes involve lepton pairs production, dissociation of nucleus and photo production. These type of background events are rejected by putting selection criteria of an energy deposition above 500 GeV in each of the neutron ZDC kept at ±114 meters from the interaction point [127].

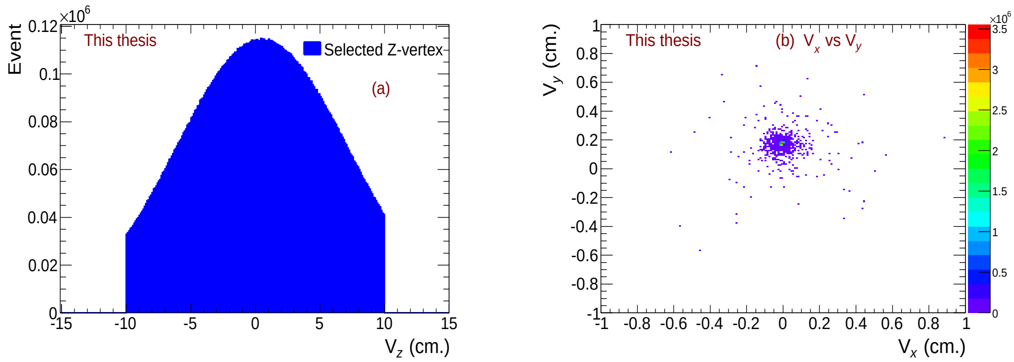

Figure 5.1: (a) z co-ordinate of the vertices of selected events, (b) Vertex-y vs, Vertex-x plot of the events in x-y plane of the collision vertex.

5.1.1.2 Vertex Selection

As mentioned earlier, to reduce the contribution of background events, events having reconstructed vertices are considered for the analysis. This is done by imposing some constraint on the position of the z component of collision vertex. Vertex position determination is done by SPD. All events are populated around the nominal interaction point ($z \sim 0$) and extend on either side. But the beam-gas events usually have higher $|V_z|$, which are comparable to the numbers of physics events. Thus, to minimize contamination from background events, events with $|V_z| < 10\ cm$ is selected. It is also possible to measure the x and y co-ordinate of the vertex. Since the analysis is carried out on AODs, there is always prefixed cut to V_x, V_y and V_z. The V_z distribution is shown in Figure 5.1(a). Figure 5.1(b) shows the scatter plot of V_x vs V_y. It is clear from Figure 5.1(b) that there is an offset of few millimeters of the vertex position in $x - y$ plane from (0,0). This implies that the beam is not perfectly aligned in the ALICE interaction point. However, this is not going to affect the analysis.

5.1.1.3 Centrality Selection

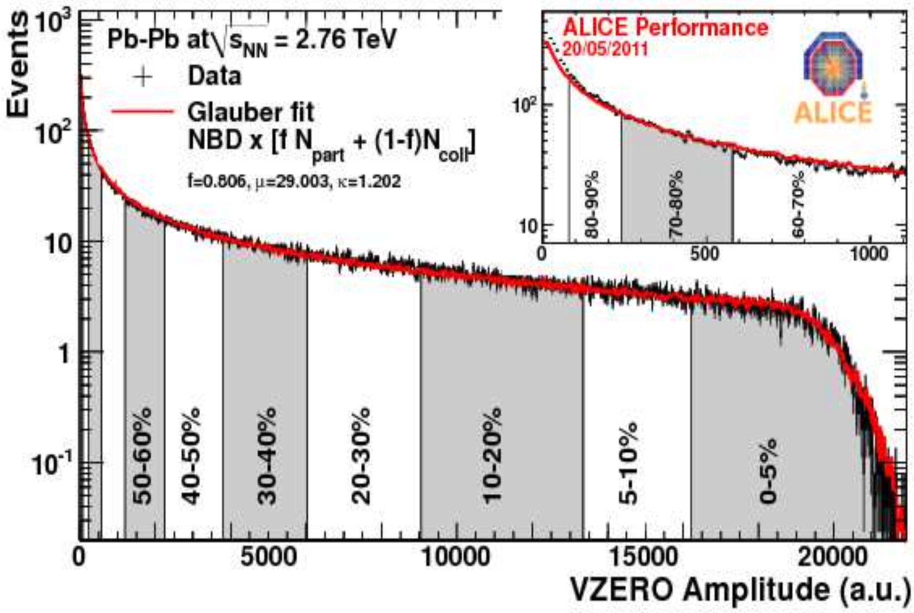

Figure 5.2: Distribution of the sum of the amplitudes in the V0 scintillators fitted with NBD-Glauber. The regions are divided into different centrality classes [128].

In heavy-ion collisions, each event has certain impact parameter. The interaction volume is always expressed via the numbers of participant nucleons (N_{part}). But neither the impact parameter nor the N_{part} are directly measured quantities in the experiment. The average charged particle multiplicity (N_{ch}) and the energy deposited in ZDC are only observables in the experiment through which the collision geometry can be determined. The average charged particle multiplicity is assumed to be decreased with increase of the impact parameter. So events are characterized by centrality classes by classifying the events according to their impact parameter. In ALICE, the centrality is defined as the percentile of the hadronic cross section corresponding to a particle multiplicity above a certain threshold or the energy deposited in the ZDC below certain threshold. In ALICE, the hadronic cross section and hence, centrality is determined by selecting the events where purity and efficiency of event selection are 100%. This purity is achieved by giving particular emphasis on the rejection of QED and machine-induced backgrounds. *Anchor*

Point (AP) is used as the absolute scale of the centrality determination which is defined as the amplitude of the V0 detector equivalent to 90$\%$ of the hadronic cross section. To determine AP, the most standard method used in ALICE is the NBD-Glauber fit to the V0 amplitude [128]. Monte Carlo Glauber model is used to determine the N_{part} and N_{coll} for a given impact parameter. NBD is used to parameterize the particle multiplicity per nucleon-nucleon collision. To incorporate both of them in the fit function, a two component model is used to fit the V0 amplitude assuming that the nucleus-nucleus collision is a contribution from linear combination of soft and hard processes. The particle production from soft processes scales linearly with N_{part}, whereas the particle production from hard processes scales with N_{coll}. The form of the two component model is,

$$N_{ancestors} = f \times N_{part} + (1 - f) \times N_{coll} \tag{5.1}$$

where $N_{ancestors}$ are the independently emitting sources of particles. f is a parameter, which controls the relative contribution of soft and hard processes. Now using AP, the event sample is divided into centrality classes, which correspond to well defined percentiles of the hadronic cross section. Then from the fit, the mean number of the relevant geometrical quantities, like N_{part} and N_{coll}, for a corresponding centrality are determined. Centrality selection is done by the ALICE offline team and assign all events with a centrality after the physics selection. Although several detectors are used for centrality estimation, V0 gives the best centrality estimation with centrality resolution $\sim 0.5\%$ for the centrality range 0-20$\%$ and below 2$\%$ for the centrality range 20-80$\%$. The V0 amplitude distributions are fitted with NBD-Glauber. Different centrality classes are shown in Figure 5.2. A list of different centrality range, the corresponding impact parameter, N_{part} and N_{coll} are given in Table 5.1. In this analysis, events of 0-80$\%$ centrality are selected and VZERO detector is used as centrality estimator. However, other detectors, like TPC and SPD, are also used to determine the centrality, which will be later taken for systematic study.

Table 5.1: Different centrality range, their corresponding impact parameter range and the number of nucleon participants obtained from MC Glauber model in Pb-Pb collisions [128]

Centrality	b_{min}	b_{max}	N_{part}	**Systematic in** N_{part}
0-5%	0.00	3.50	382.8	3.1
5-10%	3.50	4.95	329.7	4.6
10-15%	4.95	6.07	281.1	4.8
15-20%	6.07	6.98	238.6	4.2
0-10%	0.00	4.95	356.5	3.6
10-20%	4.95	6.98	260.5	4.4
20-30%	6.98	8.55	186.4	3.9
30-40%	8.55	9.88	128.9	3.3
40-50%	9.88	11.04	85.0	2.6
50-60%	11.04	12.09	52.8	2.0
60-70%	12.09	13.06	30.0	1.3
70-80%	13.06	13.97	15.8	0.6
80-90%	13.97	14.96	7.52	0.4
90-100%	14.96	19.61	3.77	0.1

5.1.2 Track Selection

In heavy-ion collision events, thousands of particles come out from the reaction zone and hit the detectors. But all particles may not be coming from the fireball. Some of the particles are from secondary interaction of the particles with the detector materials. Many of the particles, which are even originating from the fireball, may not fall in our detector acceptance and hence, can not be reconstructed efficiently. So one has to be specific about the track selection before going to any physics analysis keeping in mind about the optimization of the physics demand and detector acceptance within our region of interest. So after imposing event level cuts, now specialized track cuts have to be applied in accordance with the requirement of the analysis. The demand for a robust physics result is that the selected tracks must be primary track, within the required phase space to address the physics goal and free from any contamination of secondaries and detector effects. The whole analyses are done on AOD, which are produced from ESDs with certain filtering on the basis of physics analysis. The tracks are again stored with more specific qualitative track cuts with the name of filter bits to make them more compact in terms of data size and efficient in terms of computing time. These qualitative cuts are applied to ensure that the selected tracks are primary tracks. Primary tracks are the tracks produced in the collision, including products of strong, electromagnetic decays and weak decays of charm and beauty particles; free from the strange weak decays and other secondary particles. As discussed in Section 2, a reconstructed track can be a TPC only tracks or a Global track. In TPC only tracks, only TPC information are used for reconstruction, while for global tracks, other tracking detectors, like ITS, TOF and TRD, are used to improve the track quality. So in global tracks, the tracking is more precise and requires proper alignment of all the detectors. In AODs, there are different filter bits used to classify different categories of tracks in terms of different predefined track parameter cuts. These predefined qualitative track cuts are: numbers of TPC clusters, χ^2/ndf of the track fitting, distance of closest approach (DCA) of a track to the event vertex, kink produced from weak decays and asking whether it requires ITS refit or not for track reconstruction.

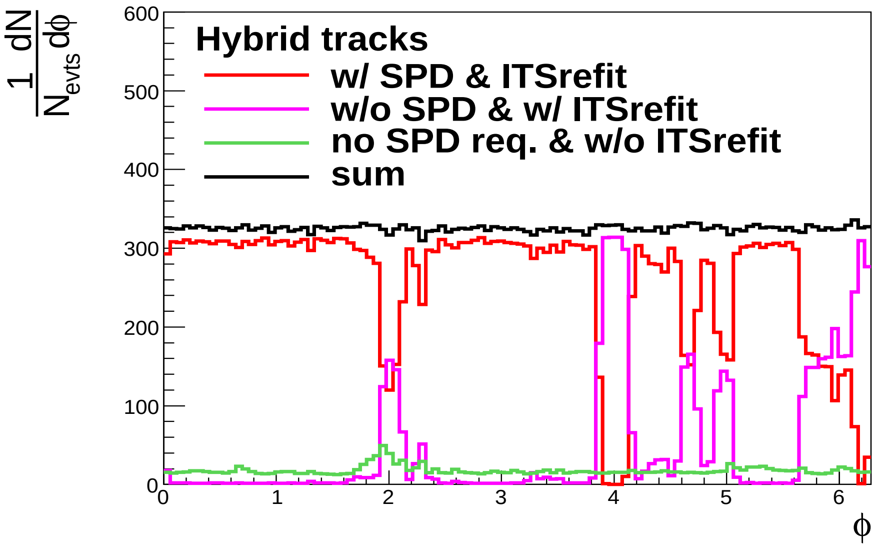

Figure 5.3: Azimuthal distribution of hybrid tracks [129].

The number of TPC clusters is the space points in the TPC used to reconstruct the track and the cut is used to ensure high efficiency track reconstruction, minimizing contribution from photon conversion and secondary charged particles produced in detector material. There are maximum 159 space points in TPC end cap, which are used for a track reconstruction. χ^2/ndf cut is used to eliminate the tracks which are not coming from the collision point. This measures the goodness of track fitting to the TPC cluster to form a trajectory of a charged particle traversing the TPC volume during reconstruction by the reconstruction algorithm. As the fundamental job is to select the primary tracks, DCA cuts are applied to ensure that the tracks are originating from the primary vertex. DCA is measured as the distance of the closet point of the particle trajectory to the primary vertex. As weakly decaying particles (e.g. $K^+ \rightarrow \mu^+\nu_\mu$) decay inside the tracking volume, the neutrino is not tracked and hence their trajectory has a kink giving the trajectory of the mother (K^+) and one of its daughter charged particle, i.e. μ^+. Such type of related tracks are reconstructed and flagged as kink mother and kink daughter. So depending on the analysis, one has to set whether the kink tracks should be selected or not. Similarly, for global tracks, to improve the track quality, it is asked whether the track needs ITS refit during reconstruction or not.

During the analysis, AODs are used and tracks are selected from AOD filter bits 272. Tracks with filter bit 272 are referred as hybrid tracks. The concept of hybrid track is as follows. During 2010 Pb-Pb data taking, some parts of the SPD were switched off in many run periods which give holes in the η and ϕ distribution of the tracks. To ensure uniform η and ϕ distributions, hybrid tracks were reconstructed using following three approaches [129],

1. global tracks with SPD hits and an ITS refit.
2. global tracks without SPD hits and with an ITS refit, constrained to the primary vertex.
3. global tracks without ITS refit, constrained to the primary vertex.

The azimuthal distribution of hybrid tracks in LHC10h data is given in Figure 5.3 for 0-10$\%$ collision centrality. It shows that how the sum of three hybrid tracks gives rise to a uniform azimuthal distribution.

Apart from the track quality cut, kinematic cuts like transverse momentum (p_T), pseudorapidity (η) cuts have to be applied depending on physics demand. Throughout the analysis, tracks which are in the pseudorapidity range of $-0.8 < \eta < 0.8$ and in full azimuthal space are used. Depending on the analysis, the tracks in the required transverse momentum range are taken which will be mentioned in the subsequent sections. Here are the tables summarizing the dataset used for this analysis.

Table 5.2: Summary of the dataset used for the study of higher moments analysis

Collision system	**Energy ($\sqrt{s_{NN}}$)**	**Production version**	**Trigger**	**AOD version**
Pb+Pb	2.76 TeV	LHC10h	Minimum bias	AOD 086

Table 5.3: Summary of the cuts used for event selection and track selection for the study of higher moments analysis

Event level cuts	**Values**	**Track level cuts**	**Values**
Vertex-z	$<$ 10 c.m.	AOD filter bit	272
Vertex-x	$<$ 3 c.m.	η	-0.8 to 0.8
Vertex-y	$<$ 3 c.m.	ϕ	0 to 2π

Table 5.4: Some basic selection cuts applied on different track parameters for construction of hybrid tracks (filter bit 272)

Track parameters	**Cut values**
Use standard TPC track	Yes
Minimum number of TPC clusters	70
Maximum χ^2/ndf per TPC cluster	4
Accept kink daughter	No
TPC refit require	Yes
ITS refit require	Yes
DCA to vertex-xy	2.4 c.m.
DCA to vertex-z	3.2 c.m.
Maximum χ^2/ndf for ITS cluster	36

5.1.3 Track QA Plots of Filter bit 272

Some basic track quality assurance plots for filter bit 272 are shown in Figure 5.4 and Figure 5.5. Figure 5.4 shows the p_T distribution and η distributions of the selected tracks, whereas Figure 5.5 represents the azimuthal angle of the selected tracks.

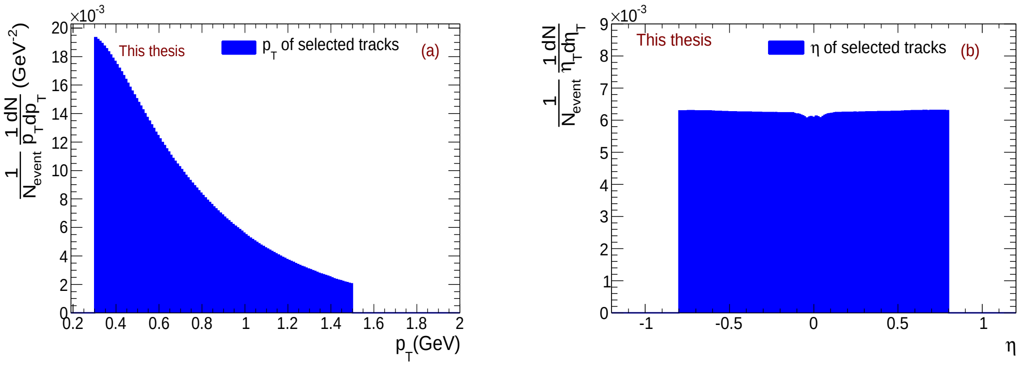

Figure 5.4: (a) Transverse momentum distribution of the selected tracks, (b) Pseudo-rapidity distribution of the selected tracks.

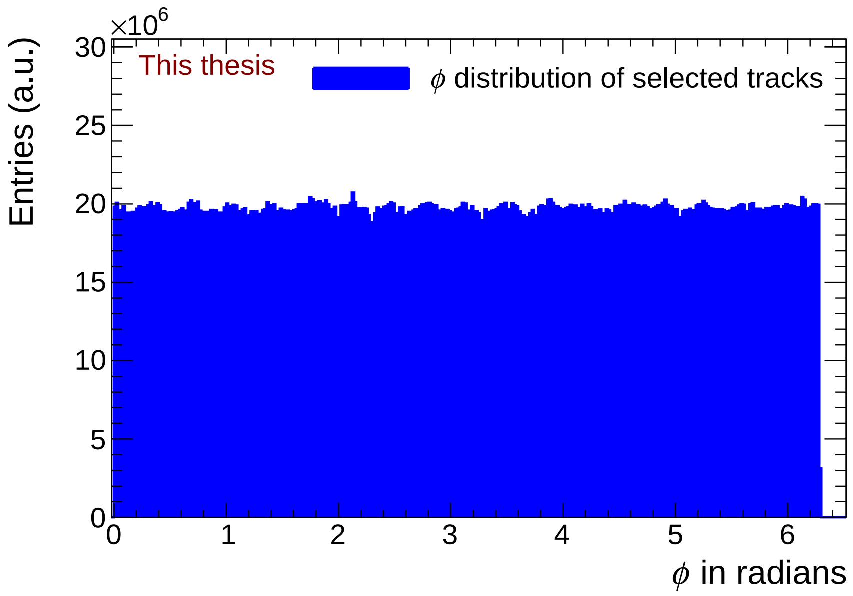

Figure 5.5: Azimuthal angle distribution of the selected charged particle's tracks.

5.2 Net-charge Analysis Results

For the measurement of higher moments of net-charge around 14×10^6 number of events were used after all the selection criteria. A histogram is drawn to show the numbers of events passed at different level of event selection during the data analysis, is given in Figure 5.6.

After event selection, the track selection criteria are imposed. All charged particles within the p_T range from 0.3 GeV/c to 1.5 GeV/c are selected. Net-charge fluctuation is

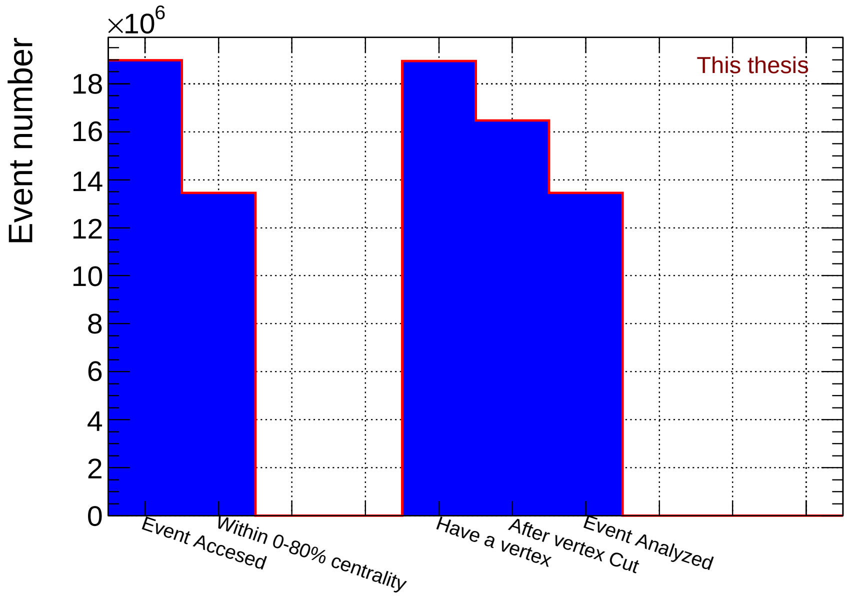

Figure 5.6: Histogram showing number of events passed different level of event selection criteria.

measured by taking the difference of total number of positive charged particles and total number of negatively charged particles on event-by-event basis. Let's say, N_+ is total number of positive charged particles, N_- is the total number of negative charged particles in an event within the detector acceptance, then the net-charged particles number (ΔN) is,

$$\Delta N = N_+ - N_- \, . \tag{5.2}$$

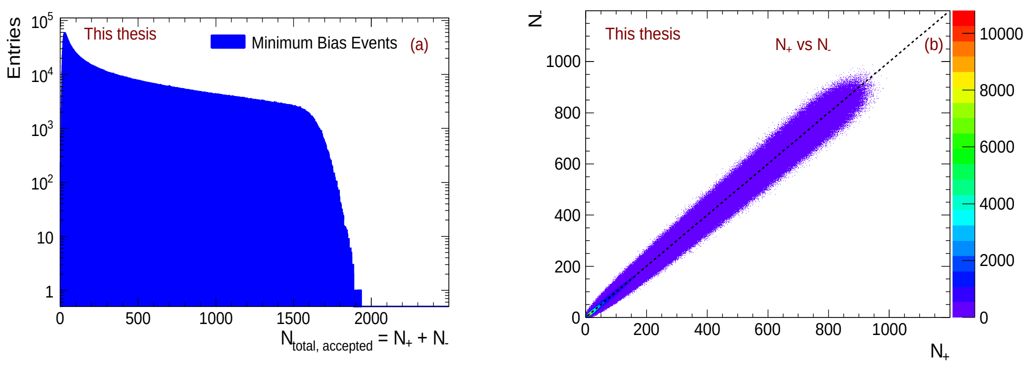

Figure 5.7: (a) Total accepted charged tracks within the applied kinematics cuts, (b) Correlation of N_+ and N_-.

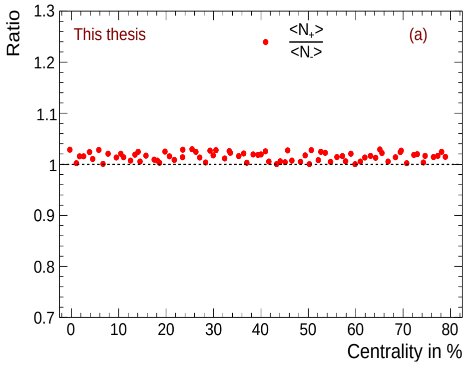

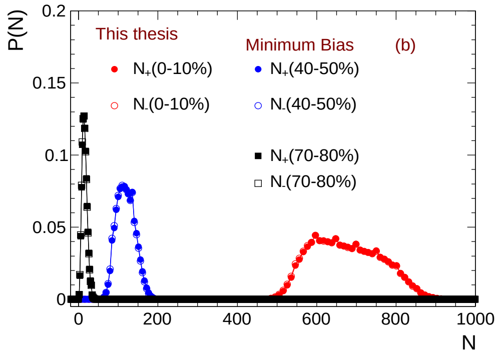

Figure 5.8: (a) Ratio of the average number of positive tracks to average number of negative tracks as a function of centrality, (b) Positive and negative charged particles distribution in different centrality bins.

This ΔN is the single variable which is used for the evaluation of different moments and cumulants. The N_+, N_- and ΔN are calculated for each 1% centrality bin width using V0M as the centrality estimator. For a large number of collection of events, a distribution of ΔN is obtained. Then mean and other central moments of that net-charge distributions are calculated by using Equation 3.13 and Equation 3.15 to 3.21. The mean, sigma, skewness, kurtosis and ratio of various order cumulants are calculated for each 1% centrality bin. Using the CBWC method, described in Section 3.6.1, moments are calculated at wider centrality bin for the final result. Before going to the higher moments results, following quality assurance checks are done. The correlation between the N_+ and N_- for the total accepted charged particles for 0-80$\%$ centrality after the track selection cuts are shown in Figure 5.7. Figure 5.7 (a) shows that there are maximum 1900 charged particles accepted within the specified acceptance region. This number is efficiency uncorrected and hence, it will increase after efficiency correction. The N_+ and N_- are very nicely correlated which can be seen in Figure 5.7 (b). The detector efficiency uncorrected $< N_+ >$ to $< N_- >$ ratios for all centralities are given in Figure 5.8 (a). This ensures that the ratios of total number of $< N_+ >$ to $< N_- >$ numbers are not varying much from one centrality to other centrality. The slight variation of $< N_+ >$ to $< N_- >$ ratios (2%) from one centrality bin to others may be accounted to the detector efficiency uncorrected numbers of charged particles. The individual N_+, N_-

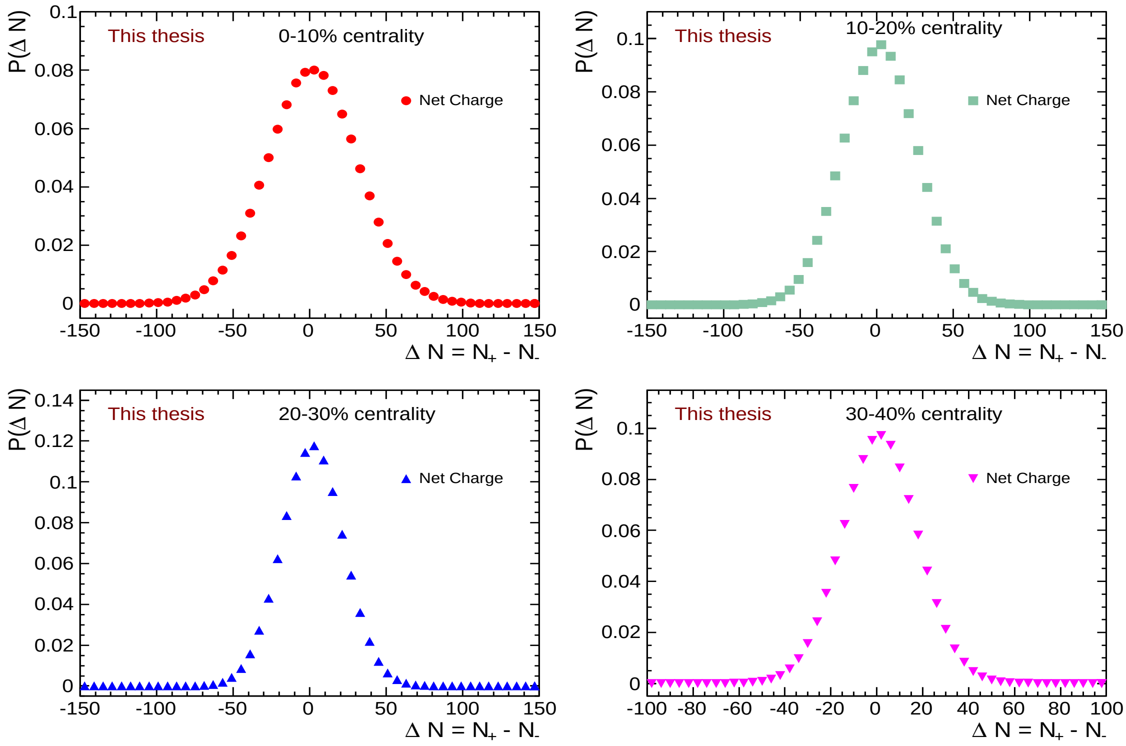

Figure 5.9: Net-charge distributions for different centralities range.

distributions for three centralities are shown in Figure 5.8 (b). The ΔN distributions for 8 centrality classes with 10% bin width are shown in Figure 5.10.

The detector efficiency uncorrected data of net-charge higher moments as a function of $\langle N_{part} \rangle$ are given in Figure 5.11, 5.12 and 5.13. The mean, sigma, skewness and kurtosis values are fitted with CLT to show their evolution with respect to $\langle N_{part} \rangle$ using Equation 3.70 to 3.73 as discussed in Section 3.6.2.

The mean values are increasing from peripheral events to central events and most central events are far away from the CLT. Similarly, the width of the net-charge distributions are increasing from peripheral events to central events. As shown in Figure 5.12, the skewness values are getting negative in two semi-central events and also deviating from the CLT line. But the kurtosis value is almost going to zero in all centralities except last three peripheral event bins. In Figure 5.13, the $S\sigma$ values are fluctuating around zero. The $\kappa\sigma^2$ values are with very high error bars and all are positive.

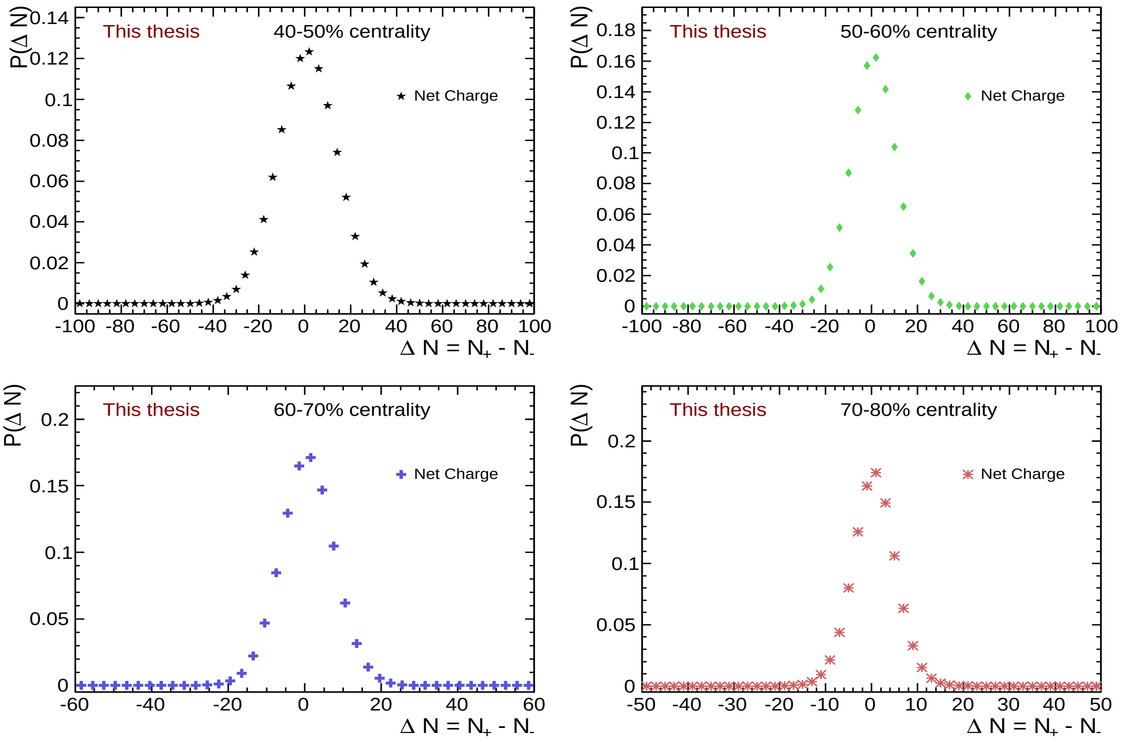

Figure 5.10: Net-charge distributions of different centralities range.

5.2.1 Simulation Study With HIJING

To understand the real experimental data, it is necessary to compare the results with relevant model. Meanwhile, the detector effect during event and track reconstruction can be studied by virtual detector simulation. For net-charge higher moments analysis, Heavy-Ion Jet Interaction (HIJING) is used as event generator for model comparison as well as to study the detector effect. ALICE has officially generated HIJING events and those events are passed through virtual detector environment and detector digitization, modeled by GEANT. The pure events at generator levels are called as true events and after passing through the GEANT, they are called as reconstructed or HIJING+GEANT events. The simulated data analysis is done as similar to the real data and same event and track selection criteria are followed. The HIJING and HIJING+GEANT results are compared with data and shown in Figure 5.15 and Figure 5.16.

The data are represented by filled blue circle, the HIJING result is represented by open magenta circle and HIJING+GEANT result is shown by filled magenta cross marker.

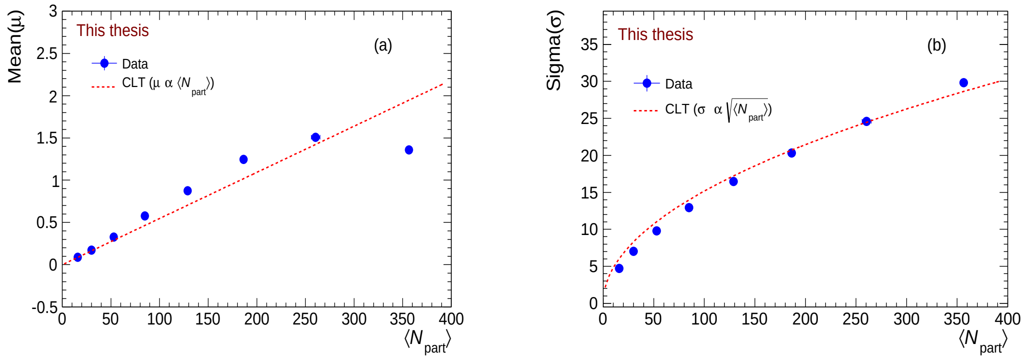

Figure 5.11: (a) Mean and (b) Sigma of net-charge distributions compared with CLT.

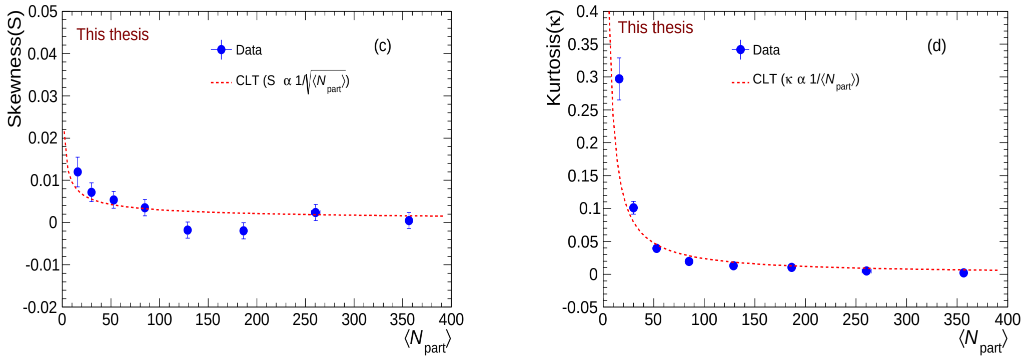

Figure 5.12: (a) Skewness and (b) Kurtosis of net-charge distributions compared with CLT.

From Figure 5.15 and 5.16, it is observed that neither HIJING nor HJING+GEANT describes the data. Simulation results from HIJING event generator, shown in Figure 5.15, suggest that the mean values are increased because of detector effect. Here the HIJING+GEANT refers to all the reconstructed tracks which include the primary tracks as well as the secondary tracks and the tracks coming from the detector materials. In short, it can be said that, because of inefficiency and contamination to the HIJING+GEANT tracks, the mean value is increased. But it is seen that the width of the net-charge distribution of the HIJING+GEANT has smaller value than the HIJING events. Similarly, other higher moments are also affected because of detector effects. The large error bars are accounted for the low event statistics (1.2×10^6). This HIJING study goes inline with the toy model study regarding the effect of event statistics and detector effect as discussed in

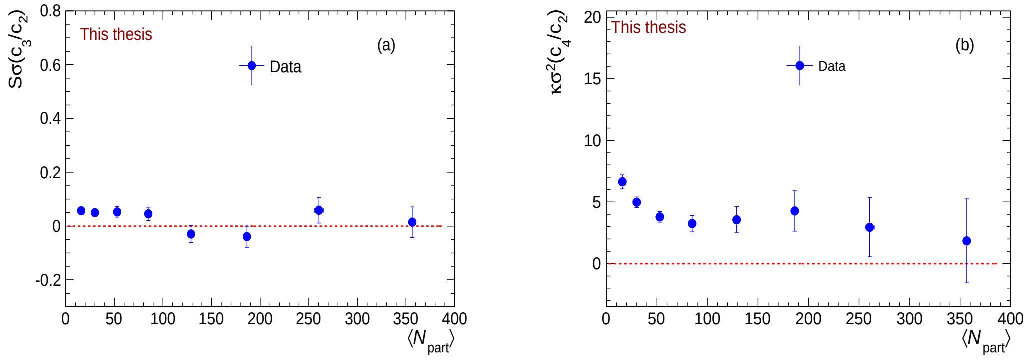

Figure 5.13: (a) $S\sigma$ and (b) $\kappa\sigma^2$ of net-charge distributions.

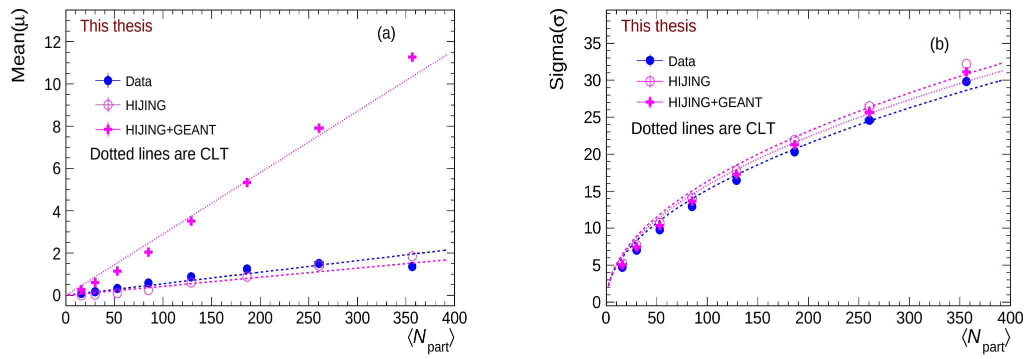

Figure 5.14: (a) Mean and (b) Sigma of net-charge distributions fitted with CLT.

Chapter 3. This implies that there are always some detector effects while representing the data and hence, it is difficult to conclude anything from the efficiency uncorrected data.

5.2.2 Systematic Study And Systematic Error Estimation

The analysis results shown so far are from the data taken by certain detectors. For example, track reconstruction in TPC, various parameters, like numbers of space points, distance of closest approach (DCA), goodness of fitting (χ^2/ndf), etc. are used to reconstruct a track. Sometime, to get good quality track which is free from possible contamination, tighter quality cuts are applied. But for these tracks, the tracking efficiency goes down. So keeping in mind both the quality and efficiency of track reconstruction, some optimal selection cuts on those parameters are used for the analysis. But it may not give

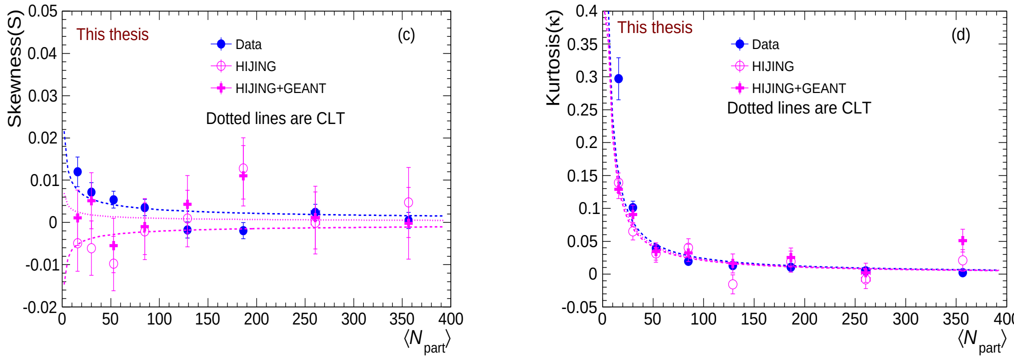

Figure 5.15: (c) Skewness and (d) Kurtosis of net-charge distributions fitted with CLT..

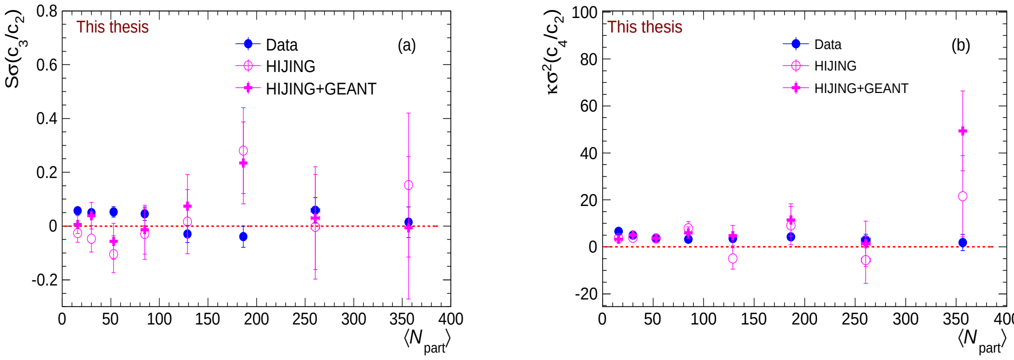

Figure 5.16: (a) $S\sigma$ and (b) $\kappa\sigma^2$ of net-charge distributions.

the most appropriate combination with other parameters to reconstruct a robust track. So there is always some systematic uncertainties associated with the track reconstruction. Similarly, for other measurements, like centrality determination by different assigned detectors, changing magnetic polarity can be treated as source of systematic uncertainties for the moments analysis of net-charge distributions. The default cut or the optimized event and track selection cuts used for this analysis is already discussed in the previous sections. The systematic studies for those mentioned sources compared with the default values are discussed below and are considered for systematic error calculation.

5.2.2.1 AOD filter bits

Different filter bits are used for different analysis. For this analysis two filter bits, i.e. 1 and 1024 are considered for the systematic. Filter bit 1 is also known as the global tracks. These global tracks are the standard TPC only tracks which require minimum 50 TPC clusters for a track reconstruction. Other track cuts used for filter bit 1 are similar to the hybrid filter bit. Track with filter bit 1024 has the track selection cuts which is used for nuclear modification factor (R_{AA}) calculation in ALICE [130]. The tracks, tagged with filter bit 1024, are reconstructed using ITS and TPC. In contrast to hybrid tracks, filter bit 1024 has some holes in the ϕ distribution of the tracks. This is because of few SPD sectors were switched off during the data taking. Tracks with filter bit 1024 use minimum 120 numbers of TPC crossed rows. TPC crossed rows are defined as the number of found clusters out of total clusters used for Kalman fit. So, it has more tighter cuts than the global tracks and equivalent cuts with respect to hybrid tracks with holes in azimuthal space. Now the analysis is carried out using these three filter bits for track selection. The results are shown in Figure 5.17. In Figure 5.17 (a), it is observed that the global tracks give largest mean values compared to the filter bit 1024 and the hybrid tracks (filter bit 272) at a particular centrality bin. Filter bit 1024 gives the mean values, which is larger than the hybrid tracks and smaller than the global tracks. The reason is as follows. In global tracks, there are more possibilities of contamination of secondary tracks due to track merging as it uses very loose cut on TPC cluster to reconstruct a track. Similarly, in filter bit 1024, as there are few holes in azimuthal distributions, it adds some artificial fluctuations to the distributions. In other higher moments and their ratios, there are slight differences of values of filter bit 1 and 1024 with respect to the hybrid tracks. This indicates that the more the quality of track, the more the purity of sample and better to study the sensitive analysis like higher moments of fluctuations of conserved numbers. The σ of net-charge distributions for three filter bits as a function of $\langle N_{part} \rangle$ are shown in Figure 5.17(b). Both filter bit 1024 and 272 have almost similar σ values whereas filter bit 1 gives larger σ values. The skewness and kurtosis of three filter bits are almost same within the statistical error bars, which are shown in Figure 5.17(c) and 5.17(d), respectively. As mentioned earlier, the σ of net-charge for filter bit 1 is more than the

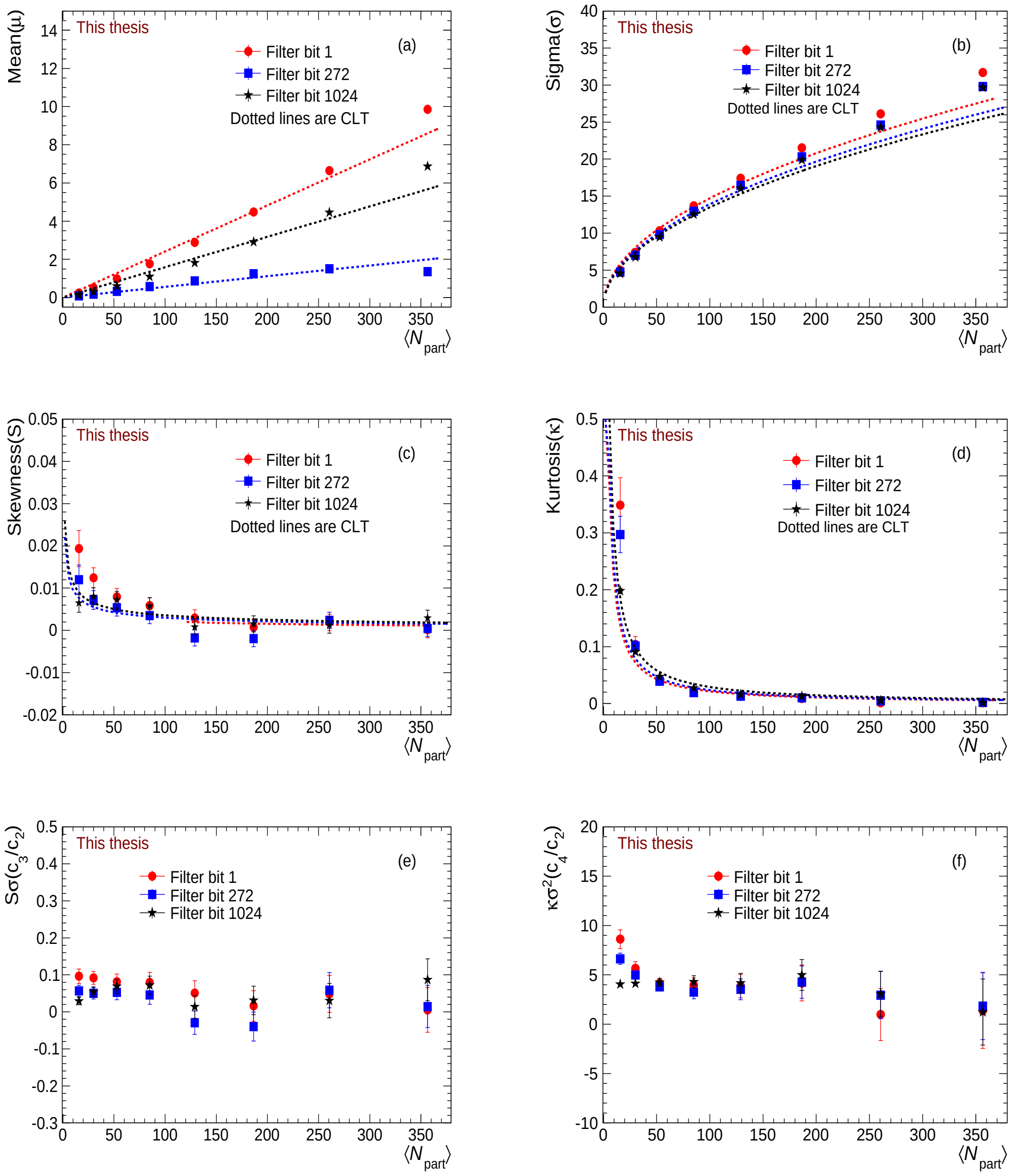

Figure 5.17: Systematic study for three filter bits (without efficiency correction).

other two filter bits, so its product with skewness and kurtosis have largest values among them, which are shown in 5.17(e) and 5.17(f).

5.2.2.2 Centrality estimators

In ALICE, there are various detectors used for centrality determination. V0M is used as the default centrality estimator as it is superior to all the detectors as mentioned in Section

5.1.1.3. For systematic study keeping all other selection criteria intact, SPD and TPC are used as centrality estimator. SPD uses the number of hits collected in its outer layer, TPC uses the number of reconstructed tracks information for centrality determination. Almost equivalent procedure, as stated for V0 detector, is used to fit the NBD-Glauber method to their distributions and the centrality is determined for both of them. Technically, centrality determination using SPD and TPC in the AOD analysis are denoted as CL1 and TRK, respectively. The detector efficiency uncorrected analysis results taking both of them as centrality estimators are shown in Figure 5.18. The result is also compared with the default centrality estimator V0M.

From Figure 5.18 (a) and (b), it is observed that the mean and sigma values are same irrespective of which detectors are used as centrality estimator. But the skewness and kurtosis results in the peripheral events are different from each other. This difference is pronounced more when the products of moments are taken, like $S\sigma$ and $\kappa\sigma^2$. This can be inferred as follows. As the analysis is done by taking the TPC and ITS tracks, there may be some auto-correlation built up when the same detectors (TPC and SPD) are used as centrality estimators.

5.2.2.3 Magnetic polarity

ALICE magnet has the capability to change its polarity. The 2010 heavy-ion data have few runs of magnetic field in positive z-directions and few runs of its reverse. But the analysis is done on the sum of these two datasets. The magnetic field along positive z-direction is referred to positive polarity and magnetic field along negative z-direction is referred to negative polarity. The numbers of events for each polarity are almost same. To see the effect of magnetic polarity to the higher moments of net-charge distributions, the systematic study is carried out. Here, the two cases are compared with each other and with all runs. The results of moments as a function of different centralities are shown in Figure 5.19.

From Figure 5.19 (a), it is observed that, in a particular centrality bin, positive polarity has the maximum mean values, whereas the negative polarity has the minimum mean values. The mean value of the full runs are just the average value of two different po-

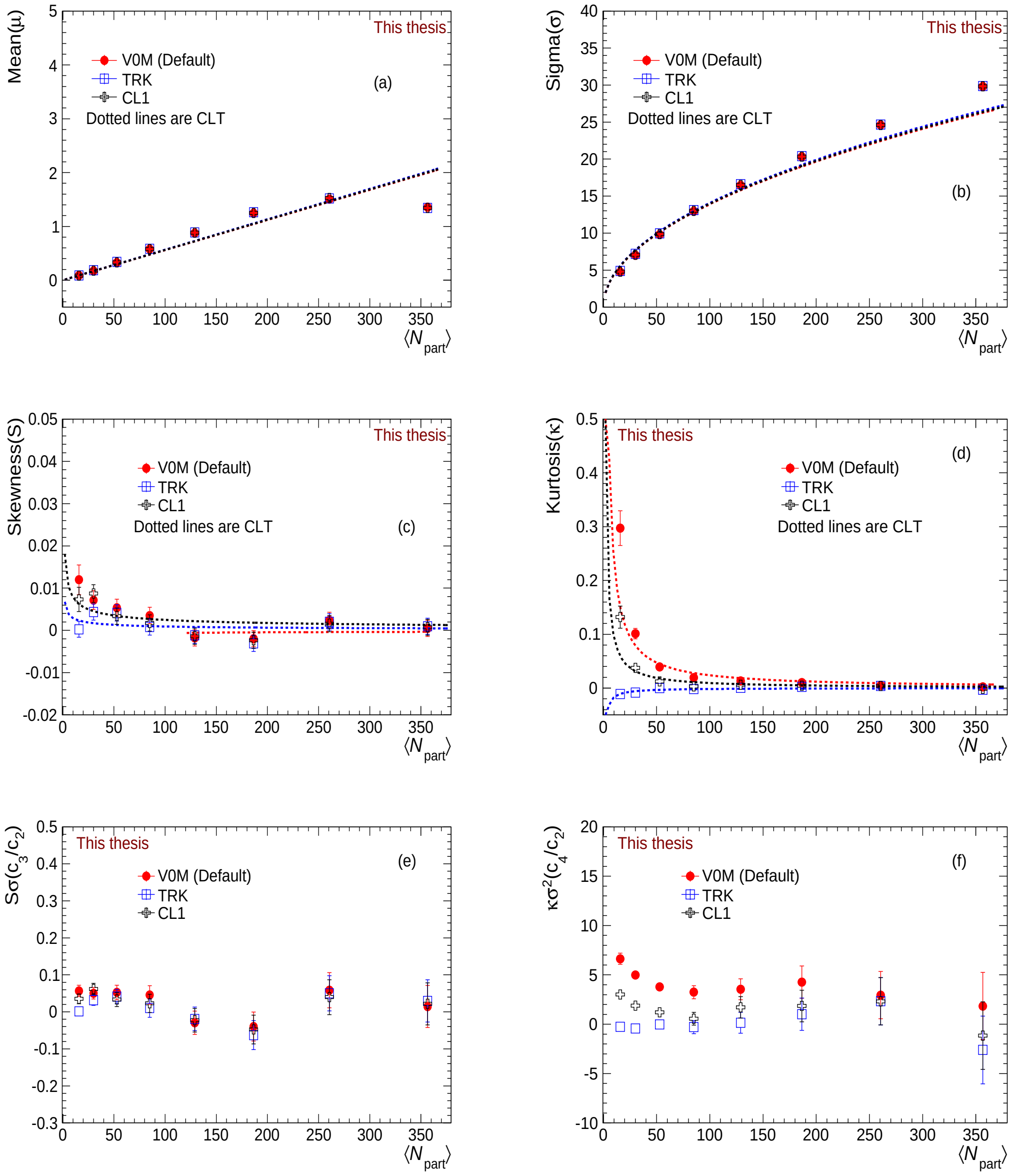

Figure 5.18: Efficiency uncorrected results of the systematic study for three different centrality estimators.

larities. But it is yet not understood why there is a substantial difference between two polarities which can be clearly seen at the most central collisions. Figure 5.19 (b) shows that the widths of the distributions are not affected by changing the polarity of magnetic field. The skewness and kurtosis of the net-charge distributions for positive polarity has always smaller values than the negative magnetic polarity. The skewness and kurtosis values of full runs are the average of the two polarities which is clear from 5.19 (c) and

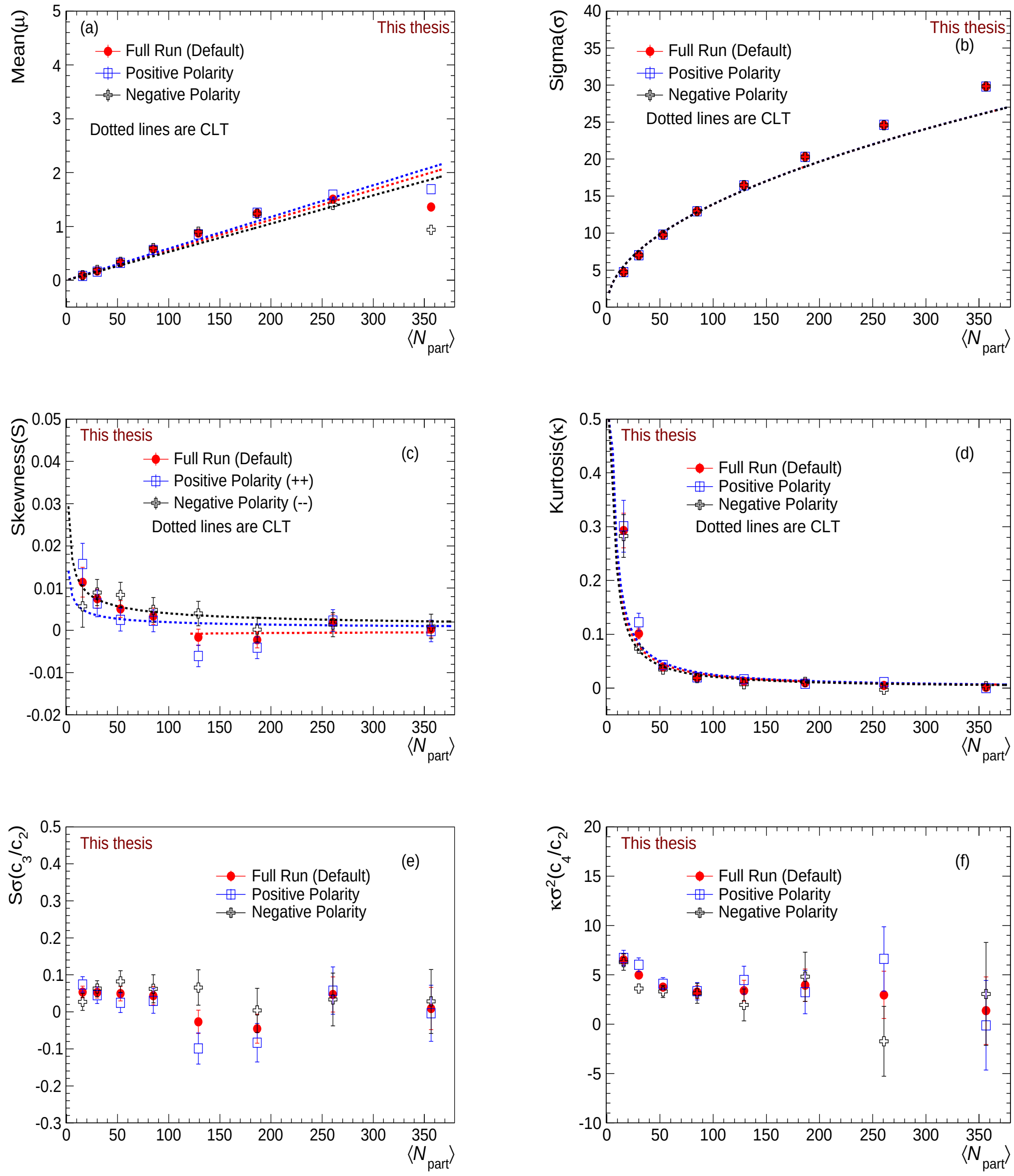

Figure 5.19: Systematic study for different magnetic polarity.

(d). The above described trends of skewness and kurtosis are reflected in the products of the moments which are shown in Figure 5.19 (e) and (f).

5.2.2.4 Systematic Error Estimation

There are six sources treated for systematic uncertainties. The results obtained from AOD fitter bit 272 (hybrid tracks) with V0M centrality estimator are treated as the reference point. Other systematic studies, like filter bit 1 (global track), filter bit 1024 (R$_{AA}$ analysis track cuts), magnetic field (with positive and negative polarity) and other two centrality estimators (TRK and CL1) are taken for systematic error estimation. If X is the reference point and X_i are the values of the respective moments from i^{th} source, then the systematic error is estimated as follows.

$$\text{Systematic Error} = X\sqrt{\sum_i \left(\frac{X_i - X}{X}\right)^2} \tag{5.3}$$

The efficiency uncorrected results with systematic errors are given in Figure 5.20. The moments values are plotted in y-axis and the $\langle N_{part}\rangle$ is plotted in x-axis. The mean, sigma, skewness and kurtosis of net-charge distributions are fitted with CLT. The open box represents the systematic uncertainty. In Figure 5.20, it is observed that the systematic error bars on mean values of net-charge distributions are very large and increasing from peripheral events to central events with a contrast to the systematic error on sigma. The main source of large systematic uncertainties for those are from filter bits. In the case of skewness and kurtosis, the systematic uncertainties are decreasing from peripheral events to central events. The products of moments ($S\sigma$ and $\kappa\sigma^2$) have also very large error bars. Such large systematic error bars are attributed to the efficiency uncorrected results for different systematic sources. The summary of the efficiency uncorrected results of net-charge higher moments with the statistical and systematic uncertainties are given for different $\langle N_{part}\rangle$ in Table 5.5, 5.6 and 5.7.

Table 5.5: The mean and sigma values of net-charge distributions for different $\langle N_{part}\rangle$ (centralities) with statistical and systematic errors.

$\langle N_{part}\rangle$	**Mean (stat±sys)**	σ **(stat±sys)**
356.5	1.35±0.02±10.14	29.81±0.01±1.88
260.5	1.50±0.02±5.92	24.60±0.01±1.54
186.4	1.24±0.01±3.64	20.30±0.01±1.28
128.9	0.87±0.01±2.22	16.45±0.01±1.05
85.0	0.57±0.01±1.30	12.94±0.007±0.85
52.8	0.32±0.007±0.71	9.79±0.005±0.67
30.0	0.17±0.005±0.36	7.02±0.004±0.50
15.8	0.08±0.003±0.15	4.72±0.002±0.36

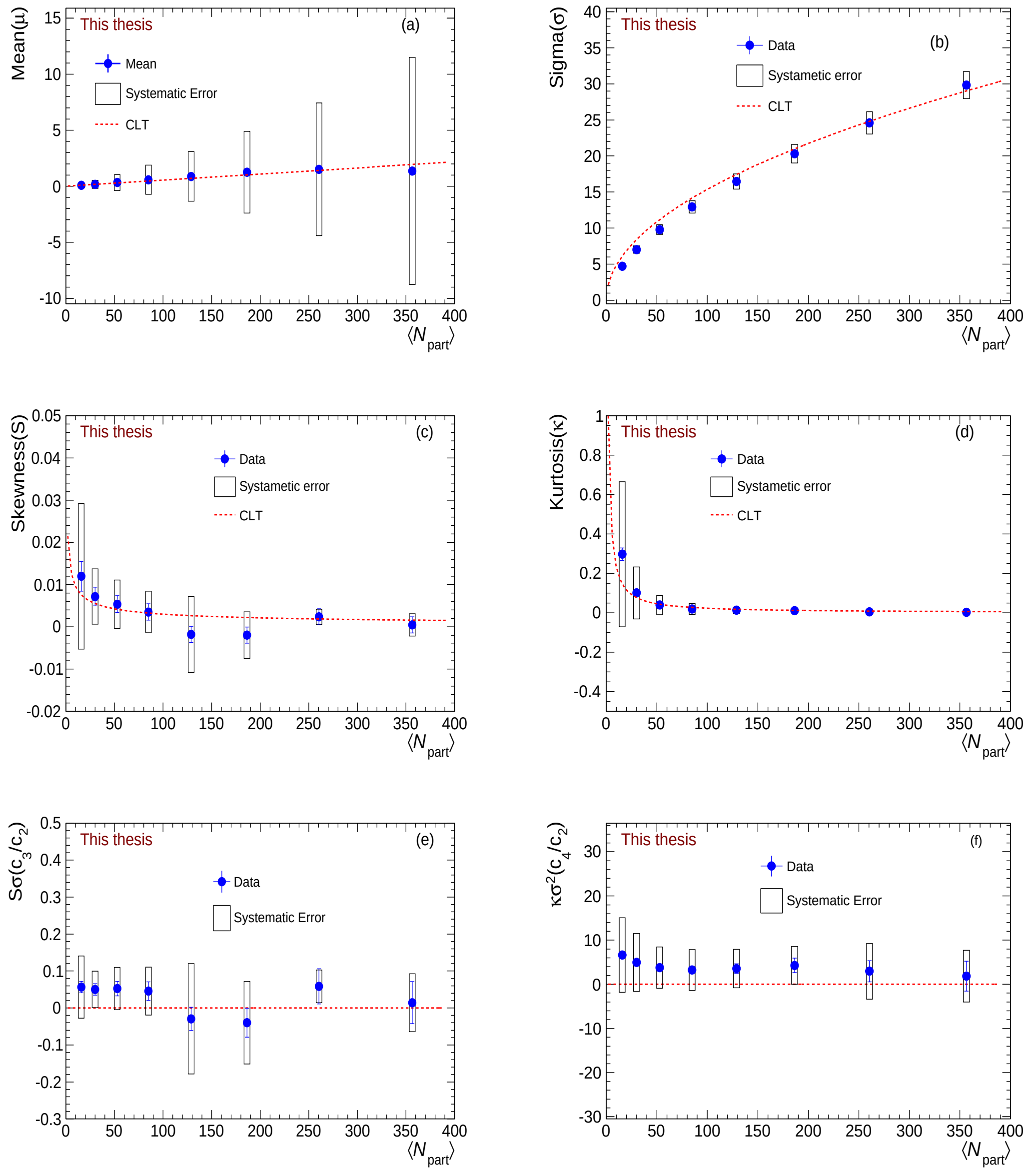

Figure 5.20: Efficiency uncorrected results of higher moments of net-charge distributions with systematic error bars.

5.2.3 Comparison of Data With Baseline Study

The efficiency uncorrected results of net-charge distributions are compared with the Poissonian and NBD expectations. The mean values of N_+ and N_- numbers are taken from the efficiency uncorrected data for the eight centrality classes and used as inputs for Poissonian and NBD expectation estimation. Then the higher moments of Poissonian and

Table 5.6: The skewness and kurtosis values of net-charge distributions for different $\langle N_{part} \rangle$ (centralities) with statistical and systematic errors.

$\langle N_{part} \rangle$	**skewness (stat±sys)**	**Kurtosis (stat±sys)**
356.5	0.0004±0.002±0.002	0.002±0.003±0.006
260.5	0.002±0.002±0.002	0.005±0.004±0.010
186.4	-0.002±0.002±0.005	0.0103±0.004±0.0106
128.9	-0.001 ±0.002 ±0.009	0.013±0.003 ±0.016
85.0	0.003 ±0.002 ±0.005	0.019 ±0.003 ±0.027
52.8	0.005 ±0.002 ±0.005	0.039 ±0.004 ±0.049
30.0	0.007 ±0.002 ±0.006	0.101 ±0.009 ±0.131
15.8	0.012 ±0.003 ±0.017	0.297 ±0.032 ±0.367

Table 5.7: The $S\sigma$ and $\kappa\sigma^2$ values of net-charge distributions for different $\langle N_{part} \rangle$ (centralities) with statistical and systematic errors.

$\langle N_{part} \rangle$	$S\sigma$ **(stat±sys)**	$\kappa\sigma^2$ **(stat±sys)**
356.5	0.01±0.05±0.07	1.84±3.40±5.89
260.5	0.05 ±0.04 ±0.04	2.95±2.39 ±6.33
186.4	-0.04 ±0.04 ±0.11	4.27 ±1.63 ±4.28
128.9	-0.03 ±0.03 ±0.15	3.55 ±1.06±4.34
85.0	0.04 ±0.02 ±0.06	3.24 ±0.66 ±4.62
52.8	0.05 ±0.02 ±0.05	3.79 ±0.43 ±4.66
30.0	0.05 ±0.01 ±0.05	4.98 ±0.42 ±6.56
15.8	0.05 ±0.01 ±0.08	6.63 ±0.56 ±8.44

NBD expectations are estimated as described in Section 3.5.1 and 3.5.2. In Figure 5.21, the NBD and Poissonian expectation values are represented by the solid continuos lines. The CLT lines are represented by dotted lines.

The baseline values (obtained from Poissonian and NBD expectations) for mean, skewness and kurtosis are same with data within the systematic uncertainties which are shown in Figure 5.21 (a), (c) and (d), respectively. But both Poissonian and NBD have higher sigma values than the data as shown in Figure 5.21 (b). The $\kappa\sigma^2$ of the Poissonian expectation values are one for all centralities and the data behave like a Poissonian within the systematic uncertainties. NBD is giving very large negative values for $\kappa\sigma^2$ and can't explain the data.

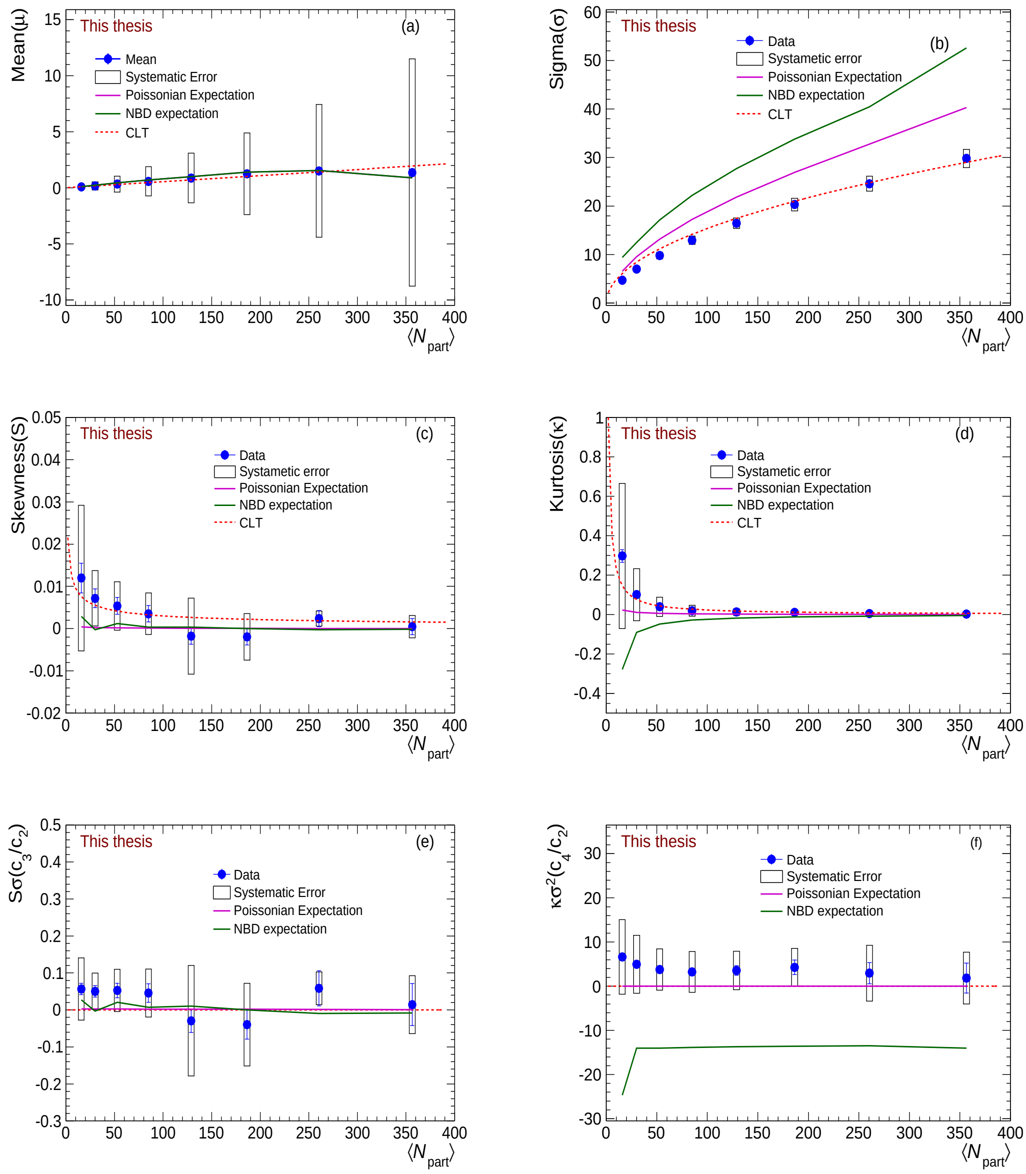

Figure 5.21: The efficiency uncorrected results of net-charge higher moments compared with the base line expectations.

5.2.4 Pseudorapidity Dependence of Net-charge Higher Moments

As discussed earlier, the heavy-ion collision system is subjected to statistical interpretation. One of the main concerns is about the system size and its formulation ground of any model, especially measurement of fluctuations under statistical ensembles, e.g. micro-canonical ensemble, canonical ensemble and grand canonical ensemble. Under

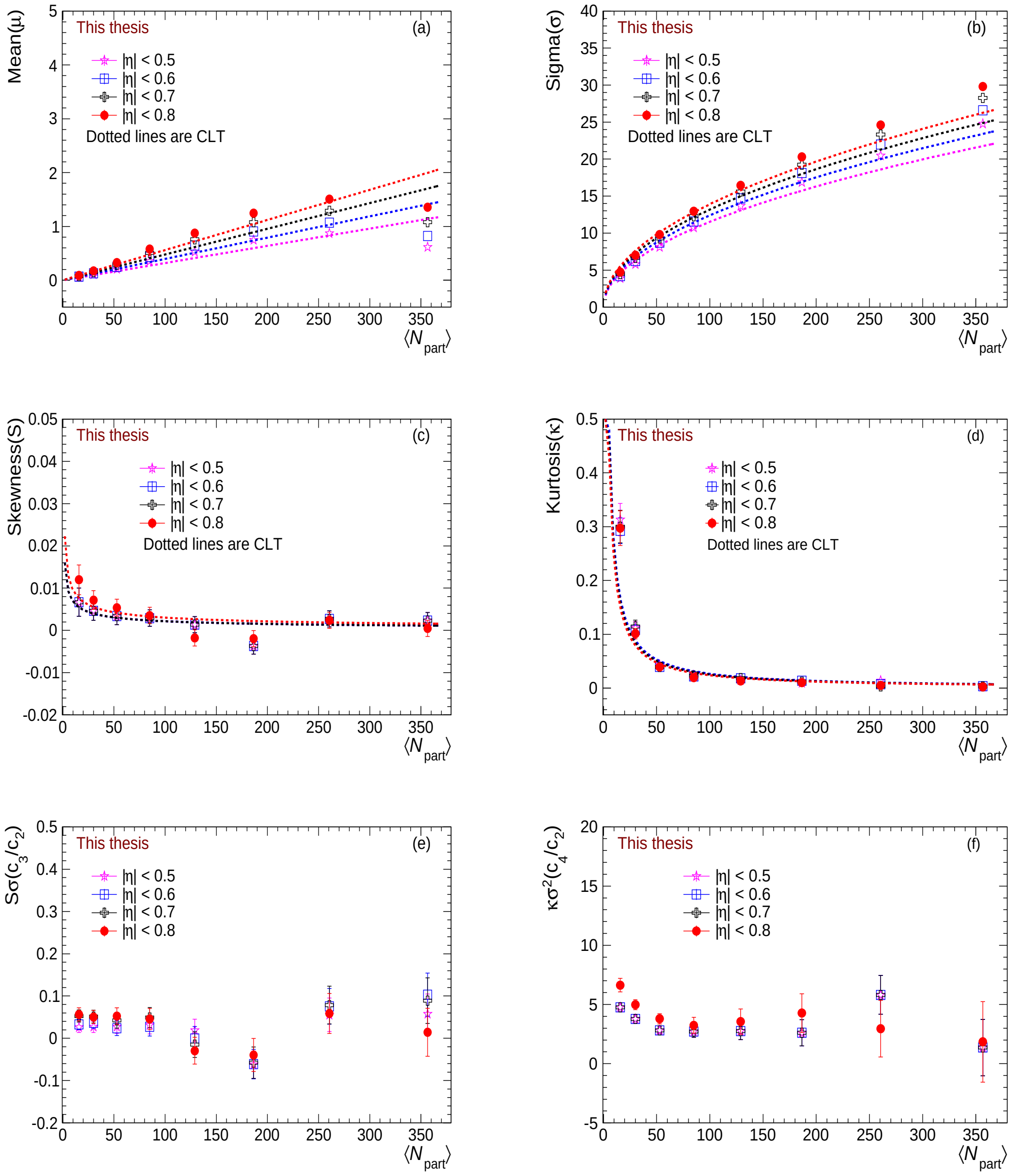

Figure 5.22: Pseudorapidity dependence of net-charge higher moments of the efficiency uncorrected data.

micro-canonical ensemble approach, the particle number and energy conservation laws are strictly fulfilled. For canonical ensemble, only material conservation laws are imposed locally and strictly, which reduces the phase space available for particle productions [131]. Canonical ensemble treatment is suitable for small collision systems and small particle multiplicities, like $e^+ + e^-$ and $p + p$ collisions. In case of grand canonical ensemble approach, the material and motional laws are relaxed, the mean values of conserved charges and energy are adjusted by introducing chemical potential and temperature. In heavy-ion collision system, where the numbers of carriers of conserved charge is large enough, grand canonical ensemble can be used [132]. In fluctuation study, like measurements of higher moments of conserved quantities (net-charge, net-baryon) both lattice QCD and HRG model use the grand canonical approach to heavy-ion collisions. But it should be noted here that in non-relativistic case, only in canonical ensemble, the particle number is fixed. However, in case of relativistic case, in high energy nuclear collisions, the particle number fluctuates both in canonical and grand canonical ensemble. So one has to be careful to choose the system volume for further thermodynamical interpretation. As we know, at relative fluctuations vanishes in the limit $V \to \infty$. Meanwhile, in an isolated system any conserved number doesn't fluctuate at all. So we should choose a part of the system (subsystem) which is large enough to neglect the quantum fluctuations as well as small enough that the entire system can be treated as heat bath and the statistical uncertainty of an observable (e.g. net-charge) can be calculated. In other word, in heavy-ion collisions, we have limited detector acceptance, so we measure a part of the whole thermodynamic system. But in the mean time, our acceptance in momentum and pseudorapidity should be large enough that the subsystem we deal with is capable of capturing the relevant fluctuations originating in the QGP phase, which can be used further for statistical interpretation as stated above.

It is shown that in heavy-ion collision that there is a possibility of wash out or dilution of fluctuations due to diffusion in the rapidity space [133]. This leads to the increase of width of fluctuations and the total charged particles (N) times the dynamical charge fluctuation (ν) can be described by an Error function as follows.

$$N\nu \approx N\nu_{\infty} erf\left(\Delta/\sqrt{8}\sigma\right), \tag{5.4}$$

where Δ is the rapidity window, $N \approx 2\rho\Delta$, ρ is the rapidity density and $N\nu_{\infty} = 2q_0(2\pi\rho^2\Sigma^2)^{-1/2}$ is the value at large rapidity window. It is also shown that the relative dynamical fluctuations approaches an asymptotic value at large rapidity window and the initial QGP fluctuations can be captured. So measurement should be done at certain minimum rapidity (pseudorapidity) space so that fluctuations originating from QGP must survive even after the freeze-out. In Ref. [51], a qualitative description has been given to find out the minimum rapidity interval required to carry out the fluctuation study. Under Bjorken scenario of expansion of fireball, if one estimates the flux of baryons inside and outside of a given subvolume and rapidity interval, it is shown that the initial fluctuation decays exponentially as follows.

$$\Delta N_b(\tau) = \Delta N_b^i \, exp\left[-\frac{1}{2\Delta\eta}\int_{\tau_i}^{\tau}\frac{d\tau}{\tau}\bar{v}(\tau)\right], \tag{5.5}$$

where ΔN_b^i and $\Delta N_b(\tau)$ are the net-baryon numbers at initial time and time τ, respectively. $\bar{v}(\tau)$ is the average thermal velocity of baryons. In the mean time, under Bjorken scenario, the temperature T falls like $\tau^{-1/3}$, then the remaing fluctuations ($\Delta N_b(\tau_f)$) at freeze-out will be

$$\Delta N_b(\tau_f) = \Delta N_b^i \, exp\left(-\frac{3\bar{v}_i}{\Delta\eta}\left[1-(T_f/T_i)^{1/2}\right]\right). \tag{5.6}$$

Now the exponent is close to $-\bar{v}_i/(2\Delta\eta)$ and hence the fluctuation survives if $\Delta\eta$ is larger than $\bar{v}_i/2 \approx 0.33$.

Secondly, due to exchange of baryon fluxes with neighboring subvolumes, the total number of baryons entering N_b^{en} or leaving N_b^{in} the subvolumes between τ_i and τ_f is given by

$$N_b^{en} = N_b^{in} = \frac{A}{2}\int_{\tau_i}^{\tau_f}\rho_b^{\tau}\bar{v}(\tau)d\tau. \tag{5.7}$$

This gives $N_b^{en} = N_b^{in} \approx N_b^i\bar{v}/2\Delta\eta$. As N_b^{en} and N_b^{in} fluctuate independently, the ratio of mean square fluctuation of the number of exchanged baryons N_b^{ex} to the average initial fluctuation can be written as,

$$\frac{[N_b^{ex}]^2}{[N_b^i]^2} \approx \frac{\bar{v}_i}{\Delta\eta}. \tag{5.8}$$

Equation 5.8 will be smaller than unity for $\Delta\eta \geq \bar{v}_i \approx 0.65$. Considering all the effects, like thermal fluctuations in the hadronization phase and time interval between hadronization and freeze-out, it is found that for fluctuation analysis, (pseudo)rapidity coverage with $|\eta| \geq 0.5$ is enough to catch the net-baryon number fluctuations originating from the plasma phase [51]. This also applies to the net-charge fluctuations also. Hence, it is considered that pseudorapidity coverage with $\Delta\eta \geq 1$ is suitable for the higher moments analysis. In ALICE, doing higher moments analysis has the advantage because of large pseudorapidity coverage. The study of pseudorapidity dependence of net-charge higher moments is carried out. The results are shown in Figure 5.22. The $|\eta|$ coverage is increased from 0.5 to 0.8 with steps of 0.1 unit. By increasing the pseudorapidity coverage, more and more charged particle tracks are captured and added to the events. That is why the mean of net-charge increases with increase in phase space coverage. This is observed in Figure 5.22 (a). The mean, sigma, skewness and kurtosis values are compared with CLT to see their evolution as a function of $< N_{part} >$. The trend of the data points is same over all the centralities when the $\Delta\eta$ is varied. It is observed from the Figure 5.22 (a) and (b) that the mean values as well as the sigma values are increasing while the pseudorapidity window is increased. This can be interpreted as that with increase of phase space coverage, more and more fluctuations are captured. However, no such change is observed in the value of skewness and kurtosis of the net-charge distributions. This is the efficiency uncorrected result of net-charge distributions. Hence, the values may change after doing the efficiency correction to the moments.

5.3 Net-proton Analysis Results

For the measurement of higher moments of fluctuation of net-proton numbers, event selections are done in the same way as it was done in the net-charge. There are around 14×10^6 number of good minimum bias events used for this analysis. Protons and anti-protons are selected within the p_T range from 0.5 GeV/c to 2.0 GeV/c. For selections of p and $\bar{p}$, Time Projection Chamber (TPC) and Time Of Flight (TOF) detectors are used. The energy loss of particles inside the TPC volume is compared with Bethe-Bloch expectations as a function of p_T as given in Equation 2.1. The difference of the measured value and expected value of energy loss ($-\frac{dE}{dx}$) with respect to the detector resolution σ is expressed as

$$n\sigma_{TPC} = \frac{dE/dx_{measured} - dE/dx_{expected}}{\sigma_{TPC}} \tag{5.9}$$

which can be calculated for each particle species. Now to select a particle, appropriate cut on $n\sigma$ of that particle is taken. More tighter the cut, more purity of the particle sample is. But in TPC, the particles (proton, pion and kaon) are identified up to 1.5 GeV/c of p_T and after that all the curves merge with each other as shown in Figure 5.23. And TOF information are used to identify particles above 1.5 GeV/c p_T region. TOF uses the arrival time of the particles to identify the particles as follows,

$$n\sigma_{TOF} = \frac{(time_{hit} - startTime) - time_{exp}(p, M, L)}{\sigma_{TOF}} \tag{5.10}$$

The $time_{hit}$ is measured by TOF detector and other information are obtained from ALICE reconstruction framework. Then from the time difference, one can calculate the β (velocity) of the particles (see Figure 5.23), which can be used to select the particles. Now to have better PID, TPC and TOF information are combined and the combined PID is defined as,

$$n\sigma_{combined} = \sqrt{(n\sigma_{TPC})^2 + (n\sigma_{TOF})^2} \tag{5.11}$$

This is provided by the *AliHelperPID* task of the ALICE offline framework. In this analysis, less than 3 $n\sigma$ cut is applied for p and $\bar{p}$ selection.

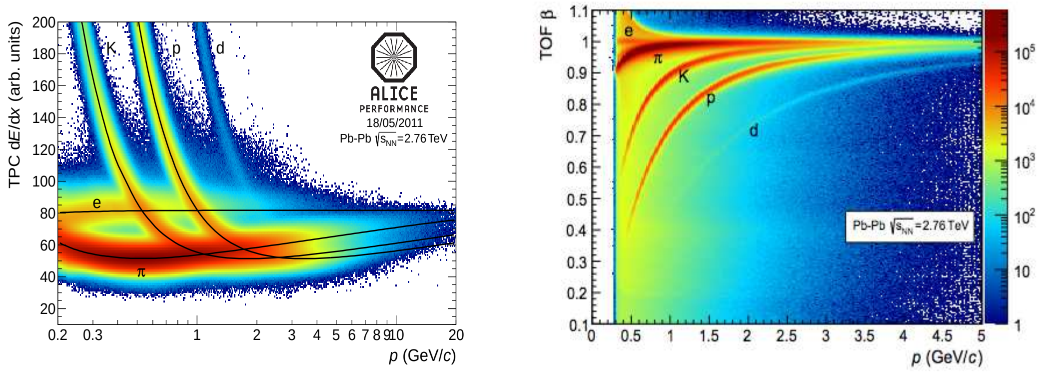

ALI-PERF-3849

Figure 5.23: (Left panel) TPC energy loss ($\frac{dE}{dx}$) of particles as a function of momentum of the particles. (Right panel) TOF β as a function of p. Figures are taken from ALICE figure repository.

After selecting protons and anti-protons, net-proton number fluctuation is measured by taking the difference of the two in an event-by-event basis. Let's say, p is total number of protons, $\bar{p}$ is the total number of anti-protons in an event, then the net-proton number (Δp) is,

$$\Delta p = p - \bar{p} \tag{5.12}$$

This Δp is the single variable which is used for the evaluation of different moments and cumulants. The p, $\bar{p}$ and Δp are calculated for 1% centrality bin width using V0M as the centrality estimator. The mean, sigma, skewness, kurtosis and ratio of various order cumulants are calculated for 1% centrality bin. Using the centrality bin-width correction (CBWC) method final results are calculated at wider centrality bin. Before going to the results, many quality assurance checks are performed on data which are shown in Figure 5.24, 5.25 and 5.26(a).

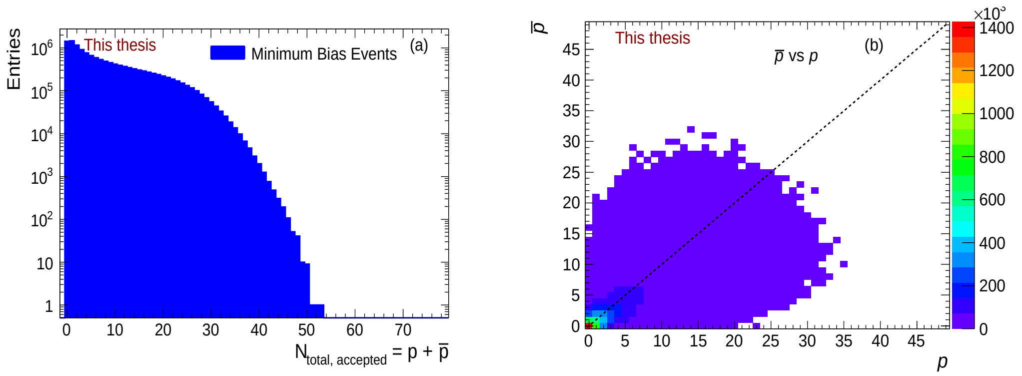

Figure 5.24: Total accepted protons and anti-protons within the applied kinematics cuts, (b) The p to $\bar{p}$ correlation plot.

The total accepted p and $\bar{p}$ for 0-80$\%$ centrality is shown in Figure 5.24 (a). The correlation between the p and $\bar{p}$ are shown in Figure 5.24 (b). There are maximum 55 number of proton and anti-proton tracks accepted in the most central events. In the proton to anti-proton correlation plot (Figure 5.24 (b)), the spread of the band implies that the correlation is weak in comparison to the N_+ and N_-. The $< p >$ to $< \bar{p} >$ ratios in 1 $\%$ centrality bin from 0 to 80 $\%$ centrality are shown in Figure 5.25 (a). There is around 20$\%$ difference of proton number to anti-proton number observed across all centrality bins.

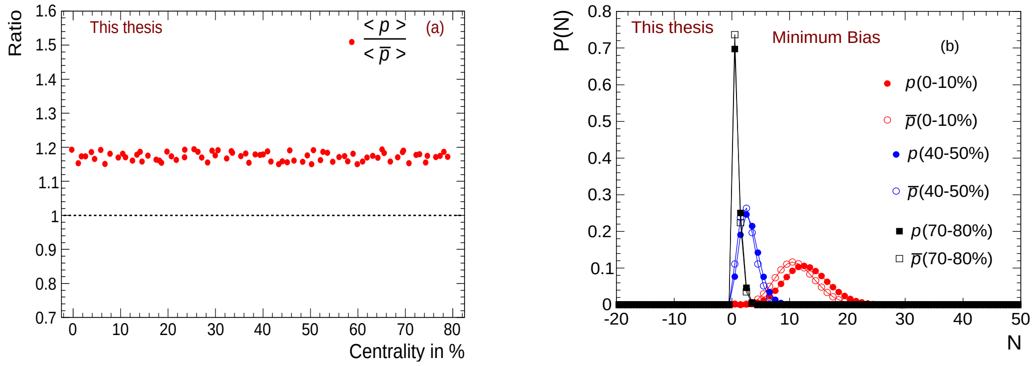

Figure 5.25: (a) Ratio of the average protons tracks to anti-proton tracks as a function of centrality, (b) p and $\bar{p}$ charged particle distributions in different centrality bins.

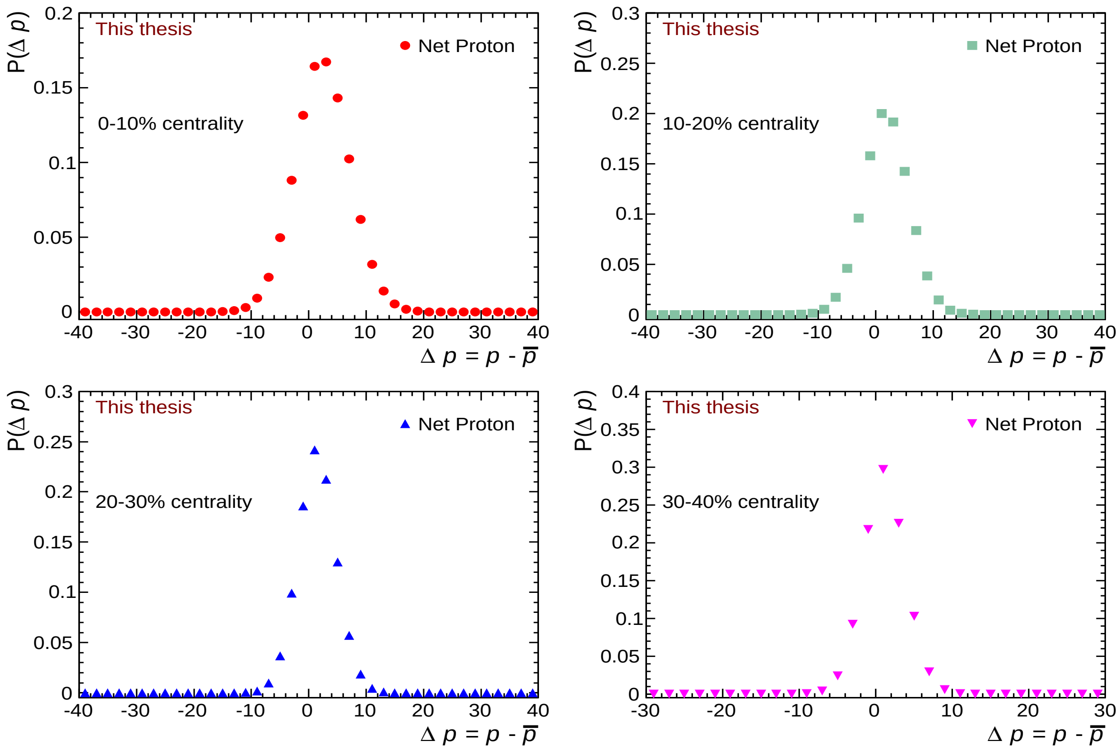

Figure 5.26: Net-proton distributions for different centralities.

However, $< p >$ to $< \bar{p} >$ ratio is close to 1 as reported in [134]. Here the discrepancy is accounted for the detector inefficiency. The individual p and $\bar{p}$ distributions are shown for three centralities in Figure 5.25 (b). The Δp distributions for 8 centrality classes with 10% centrality bin width are given in Figure 5.26 and 5.27. The detector efficiency uncorrected data of net-proton higher moments as a function of $\langle N_{part} \rangle$ are given in Figures 5.28, 5.29

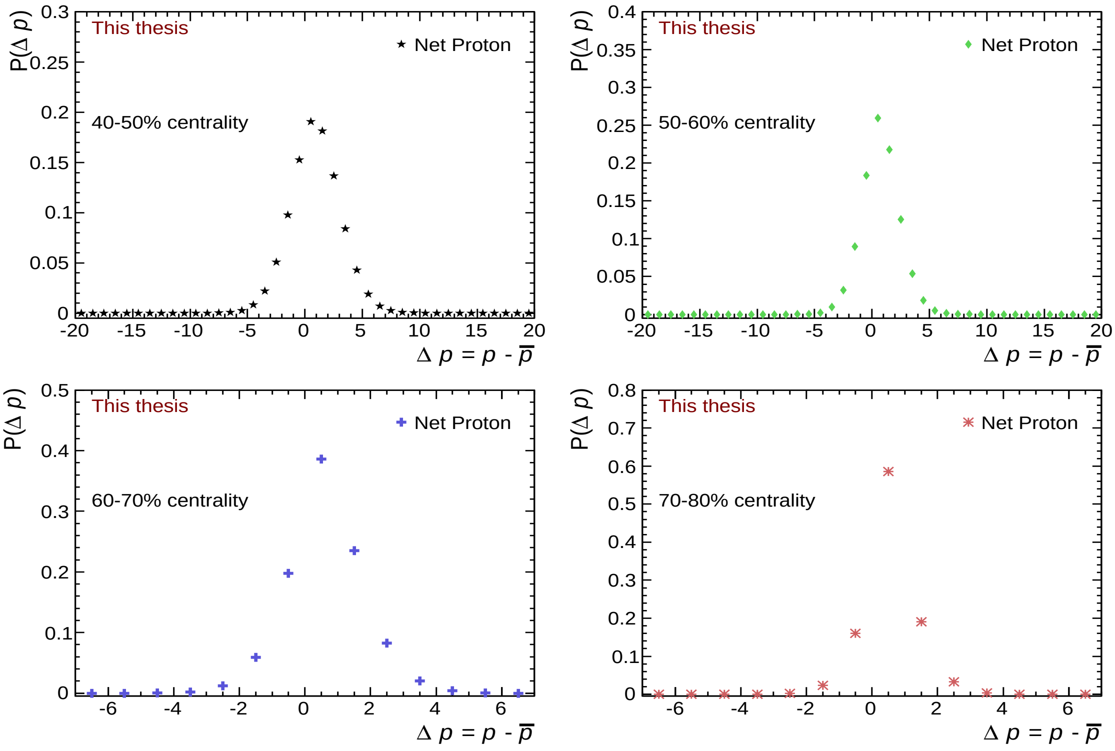

Figure 5.27: Net-proton distributions of different centralities.

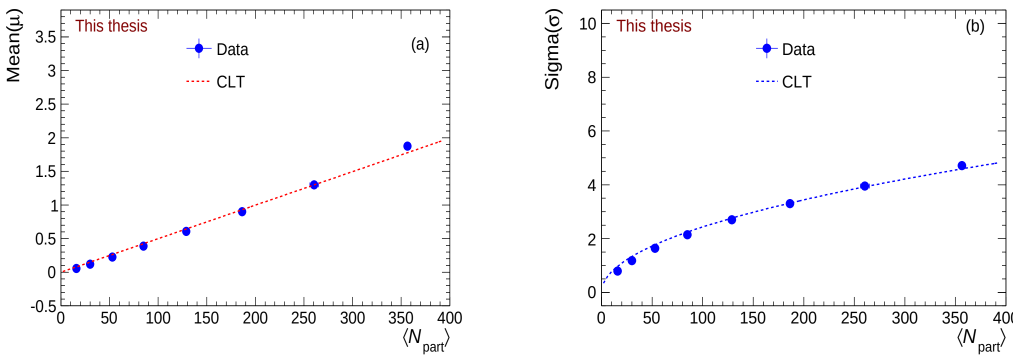

Figure 5.28: (a) Mean and (b) Sigma of net-proton distributions fitted with CLT.

and 5.30. The mean, sigma, skewness and kurtosis values are fitted with CLT to show their evolution with respect to $\langle N_{part} \rangle$. The higher moments data of net-proton distributions are fitted with CLT very nicely. The error bars are within the marker size. Very interestingly the $\kappa\sigma^2$ values are close to one which is expected from the Skellam distributions.

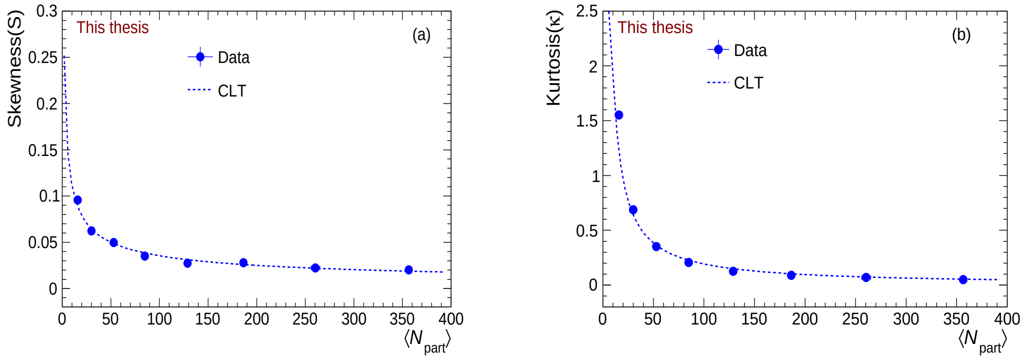

Figure 5.29: (a) Skewness and (b) Kurtosis of net-proton distributions fitted with CLT.

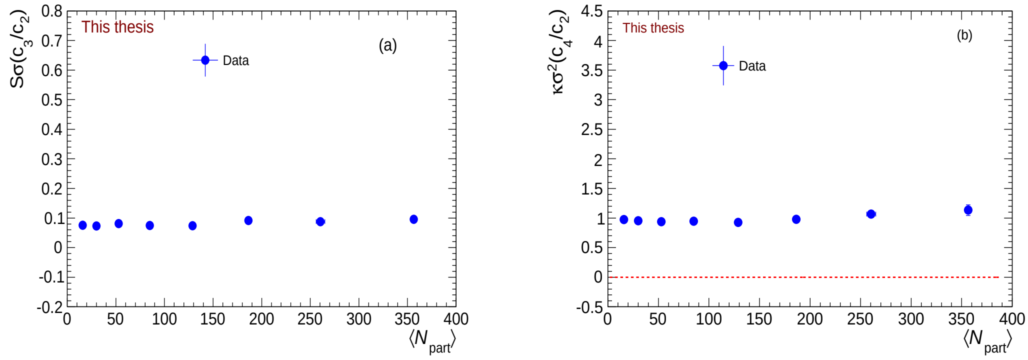

Figure 5.30: (a) $S\sigma$ and (b) $\kappa\sigma^2$ of net-proton distributions.

5.3.1 Simulation Study With HIJING

Like net-charge higher moments, the model study is done for net-proton by taking HIJING event generator and the detectors effects are studied by taking the HIJING+GEANT events. Figure 5.31 shows that the mean values of HIJING+GEANT are always higher than the HIJING values but the width of the net-proton distribution is decreased because of detector effect. Similarly, due to detector effect the net-proton distribution is more skewed with respect to the HIJING events and the peakedness also slightly increased. This can be observed from Figure 5.32 (a) and (b). Figure 5.33 (a) and (b) show that the product of the moments of HIJING+GEANT data are different than the HIJING except in few centrality bins of $\kappa\sigma^2$. This study concludes that there is always finite detector effect on the moments and product of moments of net-proton distributions, like the net-charge distributions, which needs to be corrected for final physics interpretation.

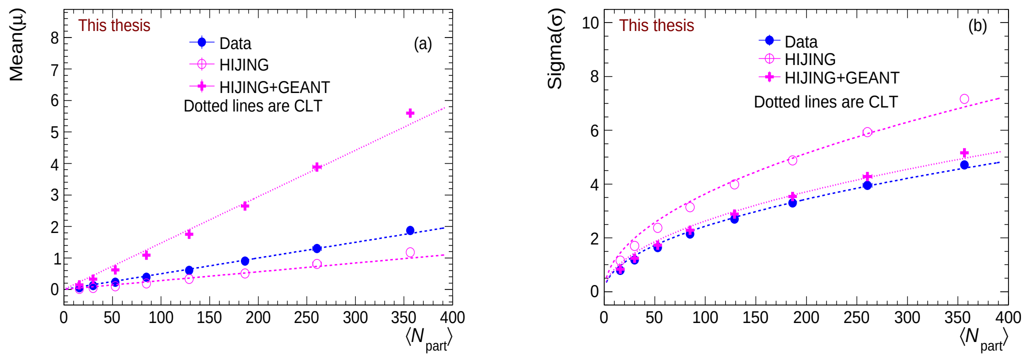

Figure 5.31: (a) Mean and (b) Sigma of net-proton distributions fitted with CLT.

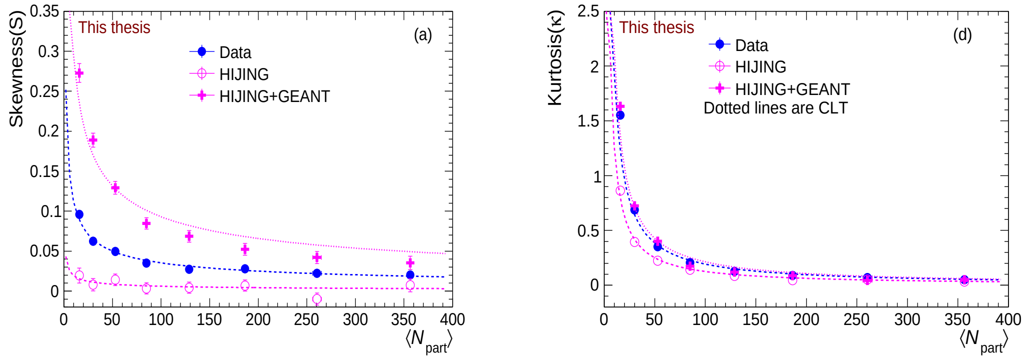

Figure 5.32: (a) Skewness and (b) Kurtosis of net-proton distributions fitted with CLT.

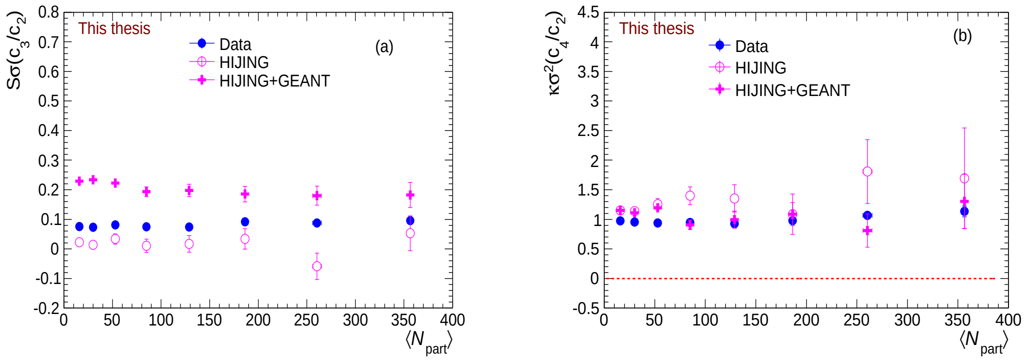

Figure 5.33: (a) $S\sigma$ and (b) $\kappa\sigma^2$ of net-proton distributions.

5.3.2 Systematic Study And Systematic Error Estimation

Like net-charge higher moments analysis, systematic studies and systematic error estimation are done by considering different sources of systematics. These are discussed below.

5.3.2.1 Filter bits

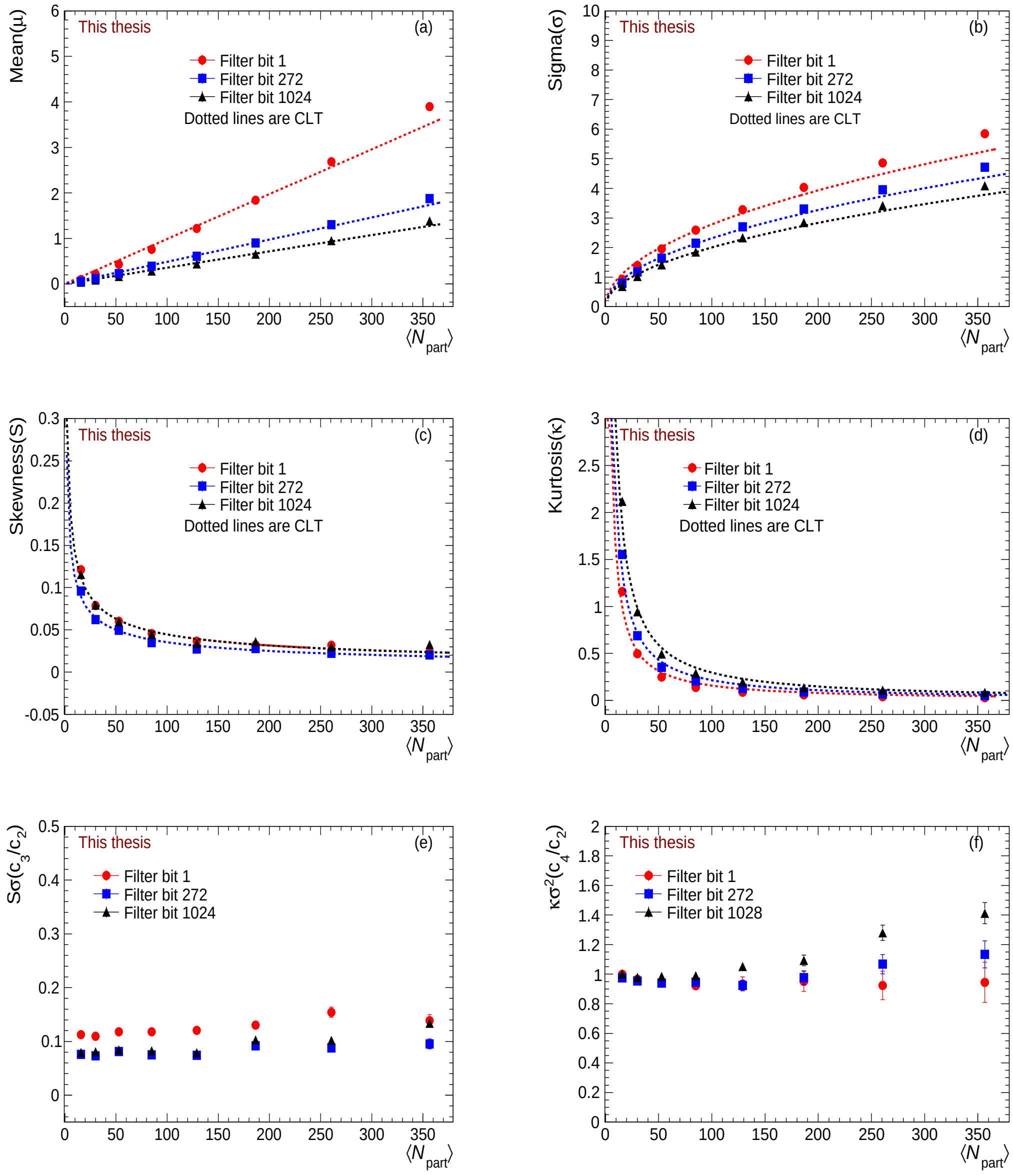

Figure 5.34: Systematic study of net-proton higher moments for three filter bits of the efficiency uncorrected results.

Filter bit 1 and 1024 are considered for systematic study to address the effect of various track selection cuts for the net-proton higher moments analysis. The results are compared with the default filter bit (filter bit 272) and are shown in Figure 5.34. The moments are fitted with CLT. In all three filter bits, the nature of fitting is almost same. This implies that the evolution of the moments as a function of $\langle N_{part} \rangle$ is same for all of them. Like net-charge higher moments systematic study, the global tracks (filter bit 1) gives larger mean and σ values than other two filter bits. However, the difference in mean values of net-proton between the dataset with filter bit 272 and filter bit 1024 is small compared to the difference in mean values of net-charge with filter bit 272 and 1024. Similar trend is observed for the σ of the net-proton distributions for all three filter bits. The skewness of the net-proton distributions are shown in Figure 5.34 (c). The default track filter bit gives the smallest skewness values than the other two filter bits. But the kurtosis value of the hybrid tracks is almost average of the two filter bits in all centrality bins. The products of the moments for three filter bits are shown in Figure 5.34 (e) and (f). Except one centrality bin, the $S\sigma$ values of filter bit 272 and 1024 are same. In case of $\kappa\sigma^2$, the results of filter bit 1 are more close to the default results.

5.3.2.2 Centrality estimators

Taking V0M as the default centrality estimator, TRK and CL1 are considered for systematic study. The results are shown in Figure 5.35. The moments results are fitted with CLT to see their evolution with respect to the $\langle N_{part} \rangle$. All of them fit with CLT nicely. It is observed from the Figure 5.35 (a), (b), (c) and (d) that there is no such substantial change for any of the two centrality estimators.

5.3.2.3 Magnetic polarity

Systematic study is done for different magnetic polarities like the net-charge. Here the two cases are compared with each other and as well as with the full dataset. The results are shown in Figure 5.36. It is also observed from Figure 5.36 (a), (b), (c), (d), (e) and (f) that the moments and their product values are same with the results of full set of run within the error bars.

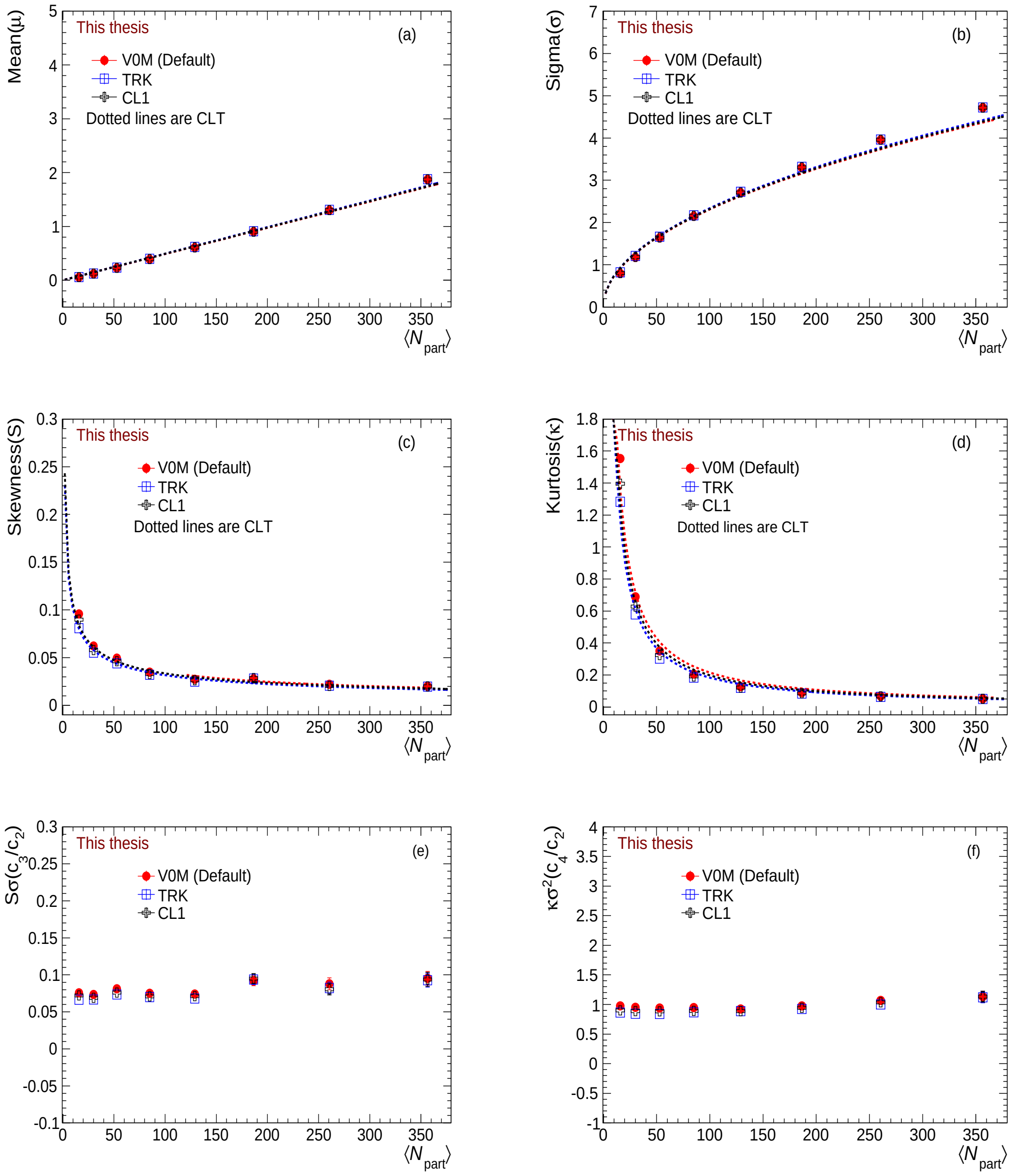

Figure 5.35: Systematic study of net-proton higher moments for three different centrality estimators (efficiency uncorrected results).

5.3.2.4 PID selection cut

The method to select protons and anti-protons may also lead to some systematic uncertainties. The systematic study of net-proton higher moments with different $n\sigma$ cuts for proton and anti-proton selection are done and compared with the default values. The results are shown in Figure 5.37. Mean, sigma, skewness and kurtosis of net-proton distributions

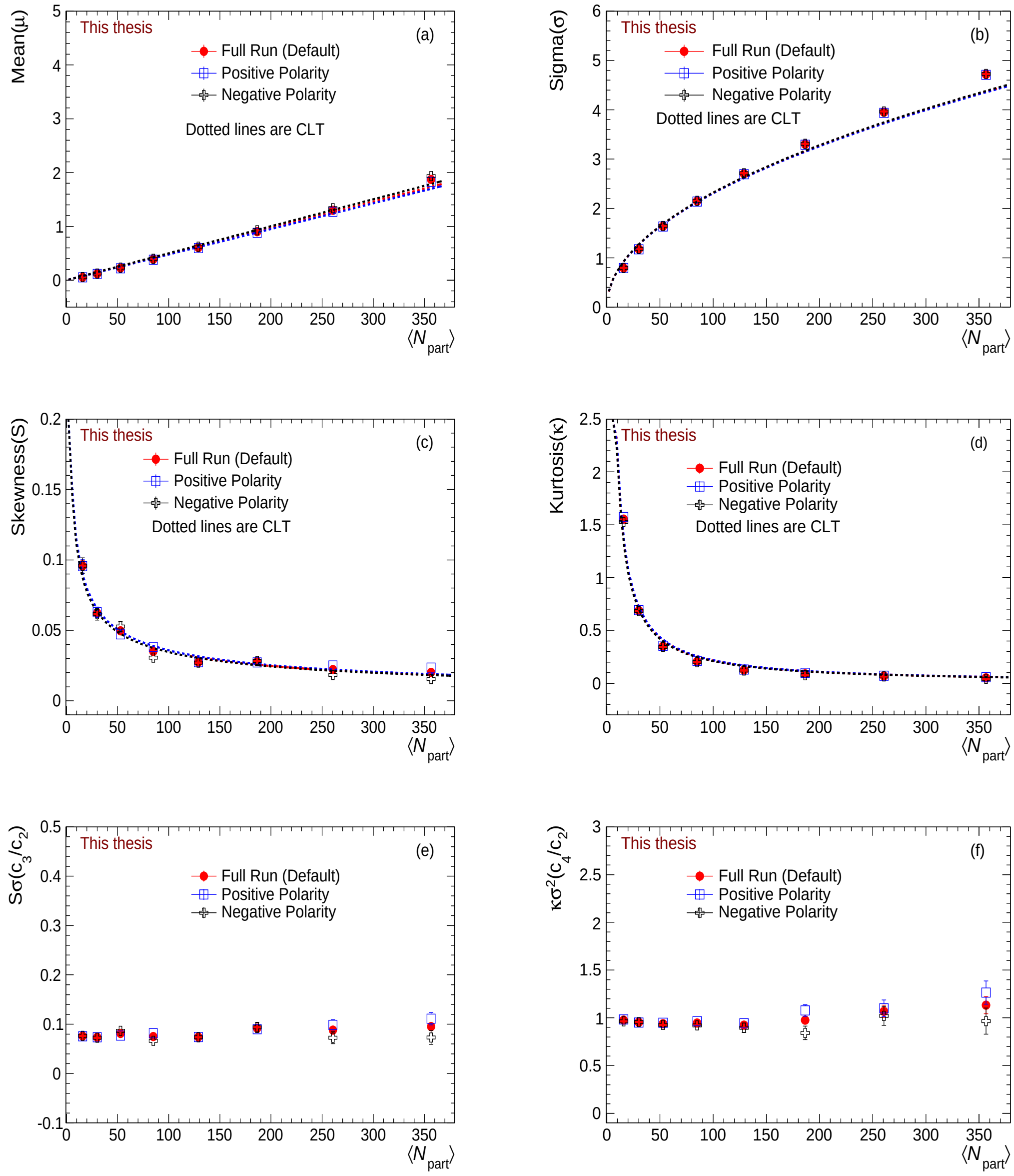

Figure 5.36: Systematic study of net-proton higher moments for different magnetic polarity (efficiency uncorrected results).

for three different $n\sigma$ cuts are fitted with CLT. All moments are fitted with CLT nicely. It is observed that small mean and σ values are observed with tight $n\sigma$ cut. This can be interpreted as the increase of purity of p and $\bar{p}$ with more stricter cut on PID selection. But for other moments like skewness and kurtosis and their products, no such change is observed by applying tighter $n\sigma$ cut for PID selection.

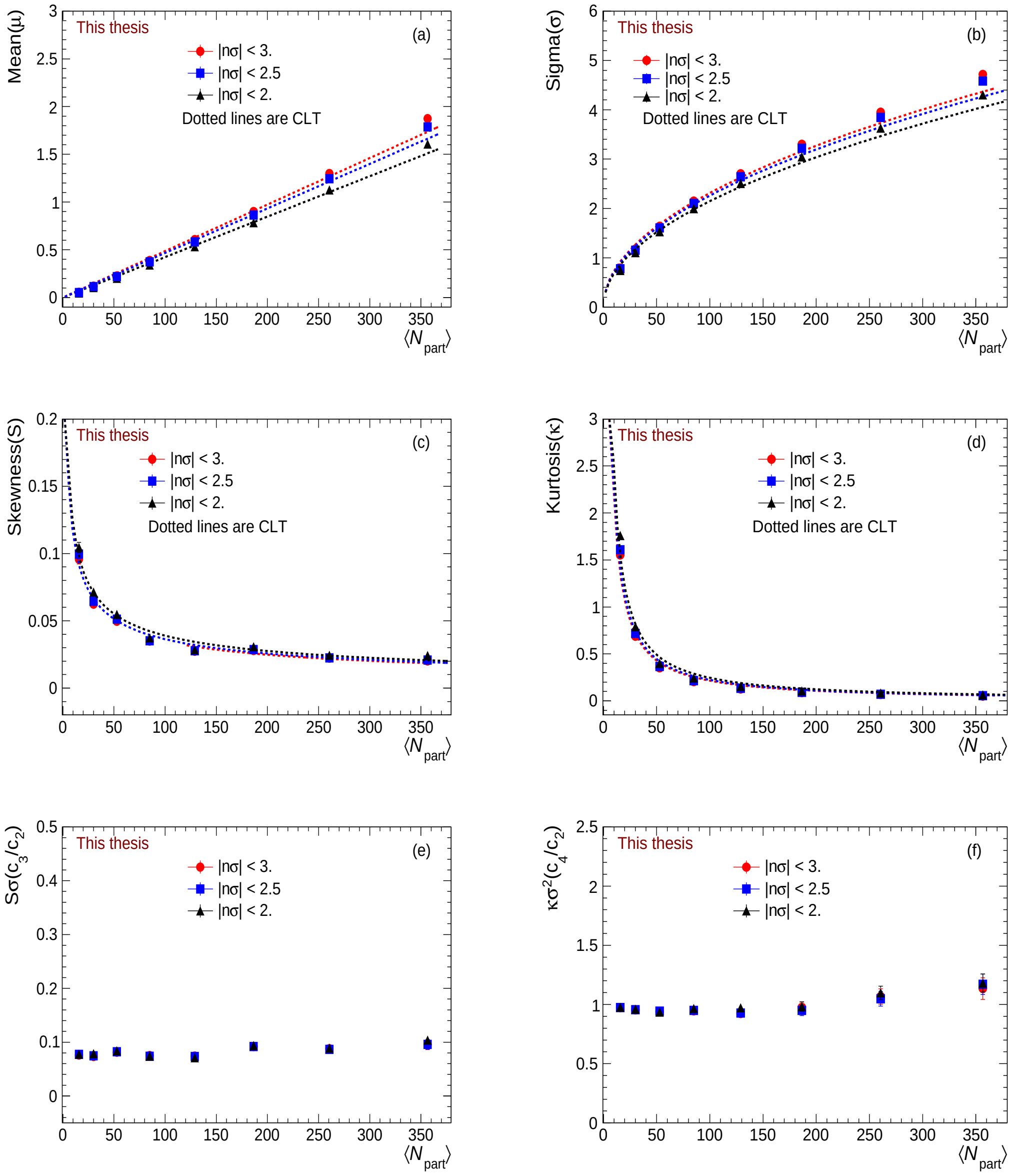

Figure 5.37: Systematic study of net-proton higher moments for different PID $n\sigma$ cut (efficiency uncorrected results).

5.3.2.5 Systematic Error Estimation

The efficiency uncorrected results with systematic and statistical uncertainties are shown in Figure 5.38. The open box represents the systematic error. These systematic errors are estimated from 8 different sources discussed previously. The systematic uncertainties are added in quadrature. The data points are also fitted with CLT.

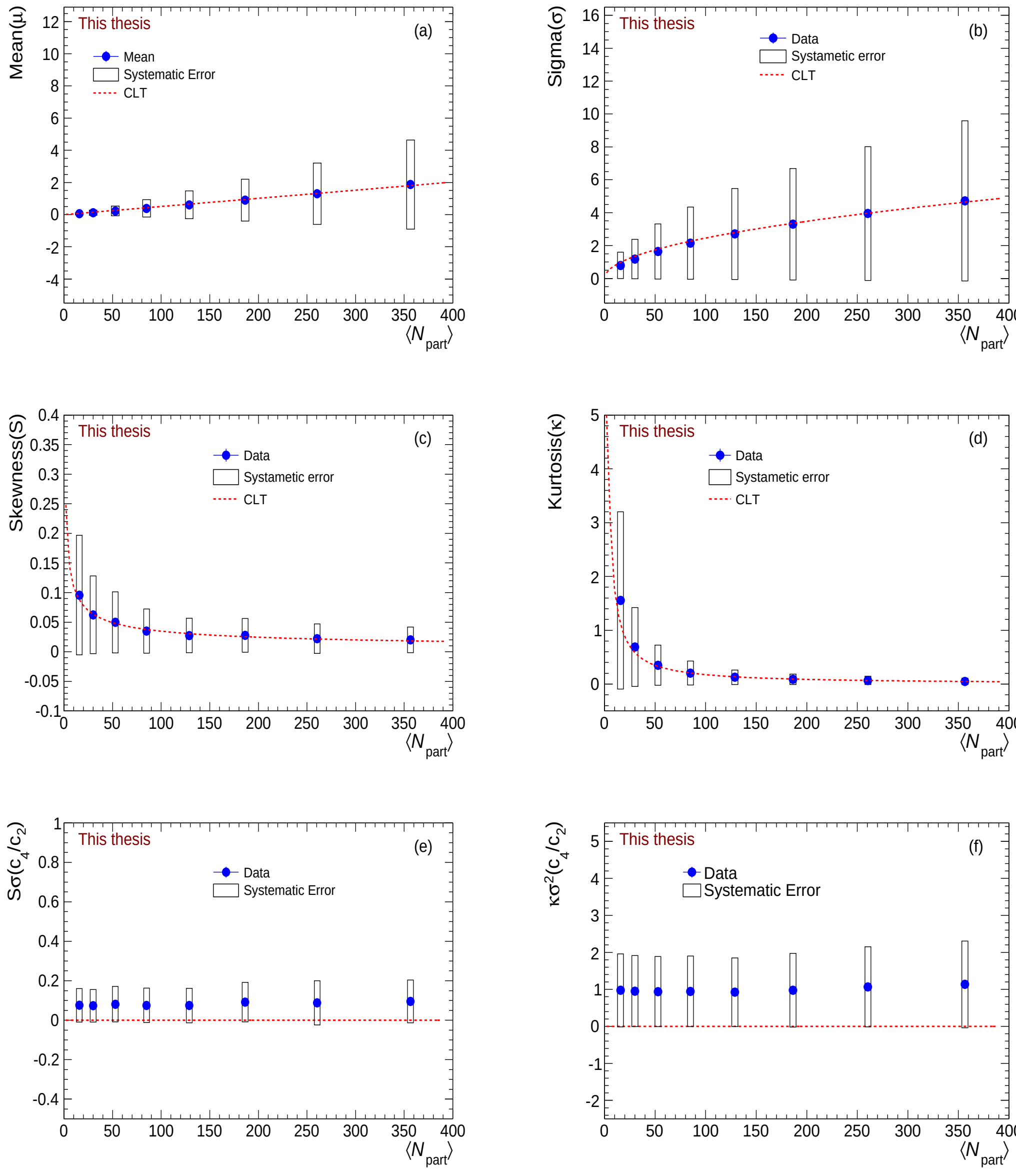

Figure 5.38: Efficiency uncorrected results of higher moments of net-proton distributions with systematic error bars.

From Figure 5.38 (a), it is observed that the systematic uncertainties for mean and sigma of net-proton distributions are increased from peripheral to central events and decreased for skewness and kurtosis. The main contribution for higher systematic uncertainties for mean and sigma is from the filter bit cuts. But for the products of moments ($S\sigma$ and $\kappa\sigma^2$), the systematic uncertainties are almost same for all eight centrality bins. The raw results of net-proton higher moments with the statistical and systematic errors are given for different $\langle N_{part} \rangle$ in Tables 5.8, 5.9 and 5.10.

Table 5.8: The mean and sigma values of net-proton distributions for different $\langle N_{part} \rangle$ (centralities) with statistical and systematic errors.

$\langle N_{part} \rangle$	**Mean (stat±sys)**	σ **(stat±sys)**
356.5	1.87±0.003±2.77	4.71±0.002±4.87
260.5	1.30±0.003±1.90	3.95±0.002±4.06
186.4	0.90±0.002±1.30	3.30±0.001±3.40
128.9	0.60±0.002±0.86	2.70±0.001±2.77
85.0	0.38±0.001±0.53	2.14±0.001±2.19
52.8	0.22±0.001±0.30	1.63±0.001±1.67
30.0	0.11±0.001±0.15	1.17±0.0007±1.20
15.8	0.05±0.0006±0.07	0.79±0.0005±0.80

Table 5.9: The skewness and kurtosis values of net-proton distributions for different $\langle N_{part} \rangle$ (centralities) with statistical and systematic errors.

$\langle N_{part} \rangle$	**Skewness (stat±sys)**	**Kurtosis (stat±sys)**
356.5	0.02±0.002±0.02	0.05±0.004±0.05
260.5	0.02±0.002±0.02	0.06±0.004±0.07
186.4	0.02±0.002±0.02	0.08±0.004±0.09
128.9	0.02±0.002±0.02	0.12±0.004±0.13
85.0	0.03±0.002±0.03	0.20±0.005±0.22
52.8	0.04±0.002±0.05	0.35±0.005±0.37
30.0	0.06±0.002±0.06	0.68±0.007±0.73
15.8	0.09±0.003±0.10	1.55±0.01±1.64

Table 5.10: The $S\sigma$ and $\kappa\sigma^2$ values of net-charge distributions for different $\langle N_{part} \rangle$ (centralities) with statistical and systematic errors.

$\langle N_{part} \rangle$	$S\sigma$ **(stat±sys)**	$\kappa\sigma^2$ **(stat±sys)**
356.5	0.1±0.01±0.10	1.133±0.1±1.170
260.5	0.08±0.007±0.11	1.06±0.06±1.08
186.4	0.09±0.006±0.1	0.97±0.04±0.99
128.9	0.07±0.005±0.08	0.924±0.03±0.927
85.0	0.07±0.004±0.08	0.94±0.02±0.95
52.8	0.08±0.003±0.08	0.94±0.01±0.94
30.0	0.07±0.003±0.08	0.95±0.01±0.96
15.8	0.07±0.002±0.08	0.97±0.006±0.98

5.3.3 Comparison Of Data With Baseline Study

The efficiency uncorrected results of higher moments of net-protons are compared with the Poissonian and NBD expectations. The expectation values, evaluated by the method explained in Section 3.5.1 and 3.5.2, are plotted against the raw results in Figure 5.39. The solid green lines represent the Poissonian expectation values and solid magenta lines represent the Binomial expectations. The expectation values obtained from NBD and Poissonian assumptions are almost same and close to the efficiency uncorrected results of data. Within the systematic uncertainties, both NBD and Poissonian lines explain the mean, sigma and skewness values of net-proton distributions of data. But some peculiar behavior is observed from NBD values for kurtosis and hence for $\kappa\sigma^2$. The reason is still not clear. The $\kappa\sigma^2$ value of net-proton distribution is almost equal to one in all centralities. Hence, it can be said that the efficiency uncorrected higher moments results of net-proton distribution is Poissonian kind. However, it is difficult to make any conclusion of this result in the present scenario and make any connection to the determination of freeze-out parameter.

5.3.4 Pseudorapidity Dependence of Higher Moments

A study is done to see the evolution of net-proton number fluctuations by increasing the pseudorapidity coverage. The pseudorapidity window is increased with the step of 0.1 unit from $|\eta| < 0.5$ up to $|\eta| < 0.8$. The pseudorapidity dependence of net-proton higher moments for different pseudorapidity coverage are shown in Figure 5.40. The data points

are also fitted with CLT to see their evolution with respect to $\langle N_{part} \rangle$. It is observed from Figure 5.40 (a) and (b) that with the increase of pseudorapidity coverage, the efficiency uncorrected mean and sigma values are increased. Otherwise, other higher moments are same for all pseudorapidity coverage. Moreover, the products of the moments are same for all pseudorapidity coverage. This study shows that the nature of the net-proton distribution is not affected except the mean and width of it. And hence the ratio of the cumulants or the products of the moments are same for all four pseudorapidity

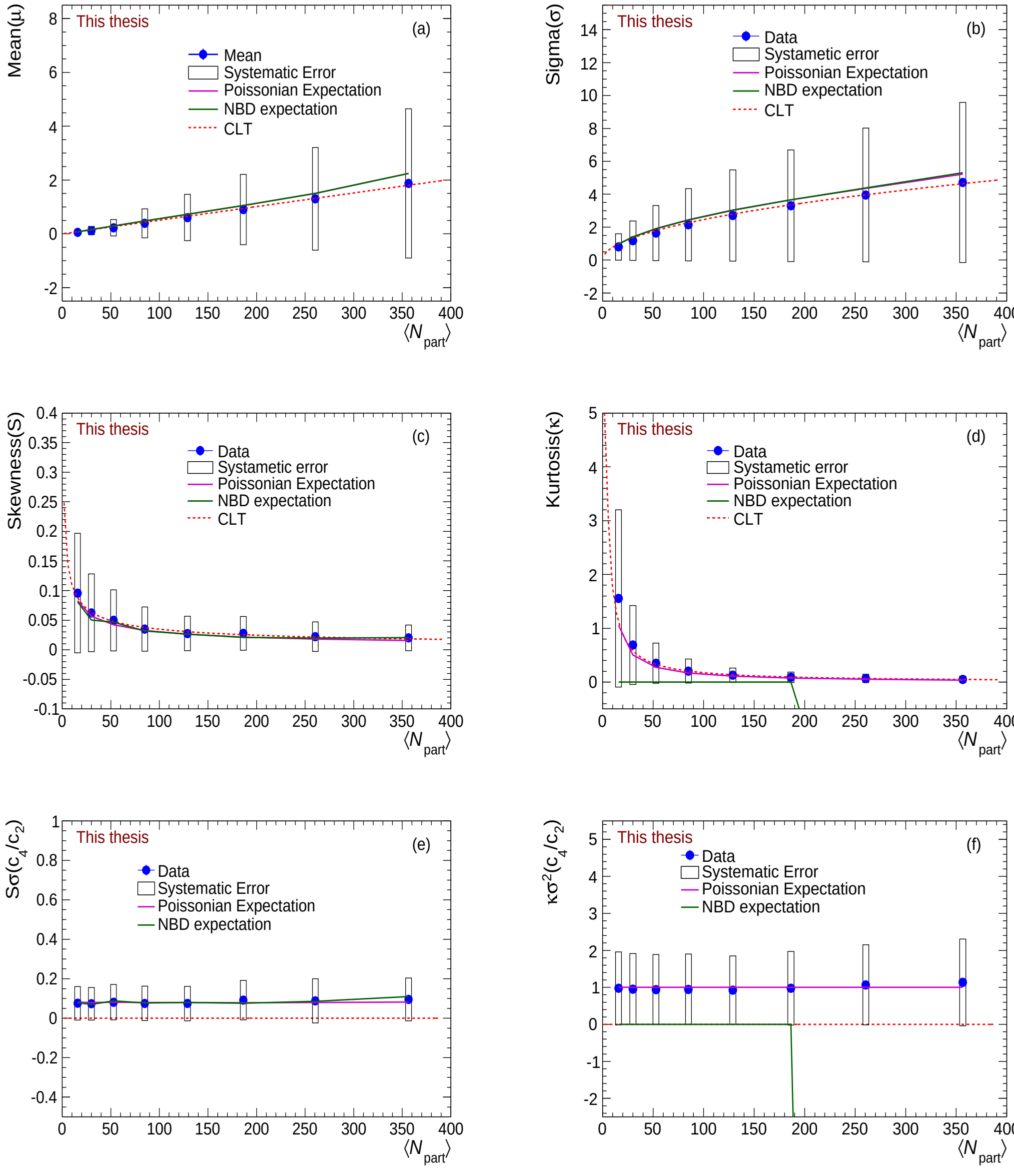

Figure 5.39: Comparison of net-proton higher moments results with baseline expectations.

window in a particular centrality.

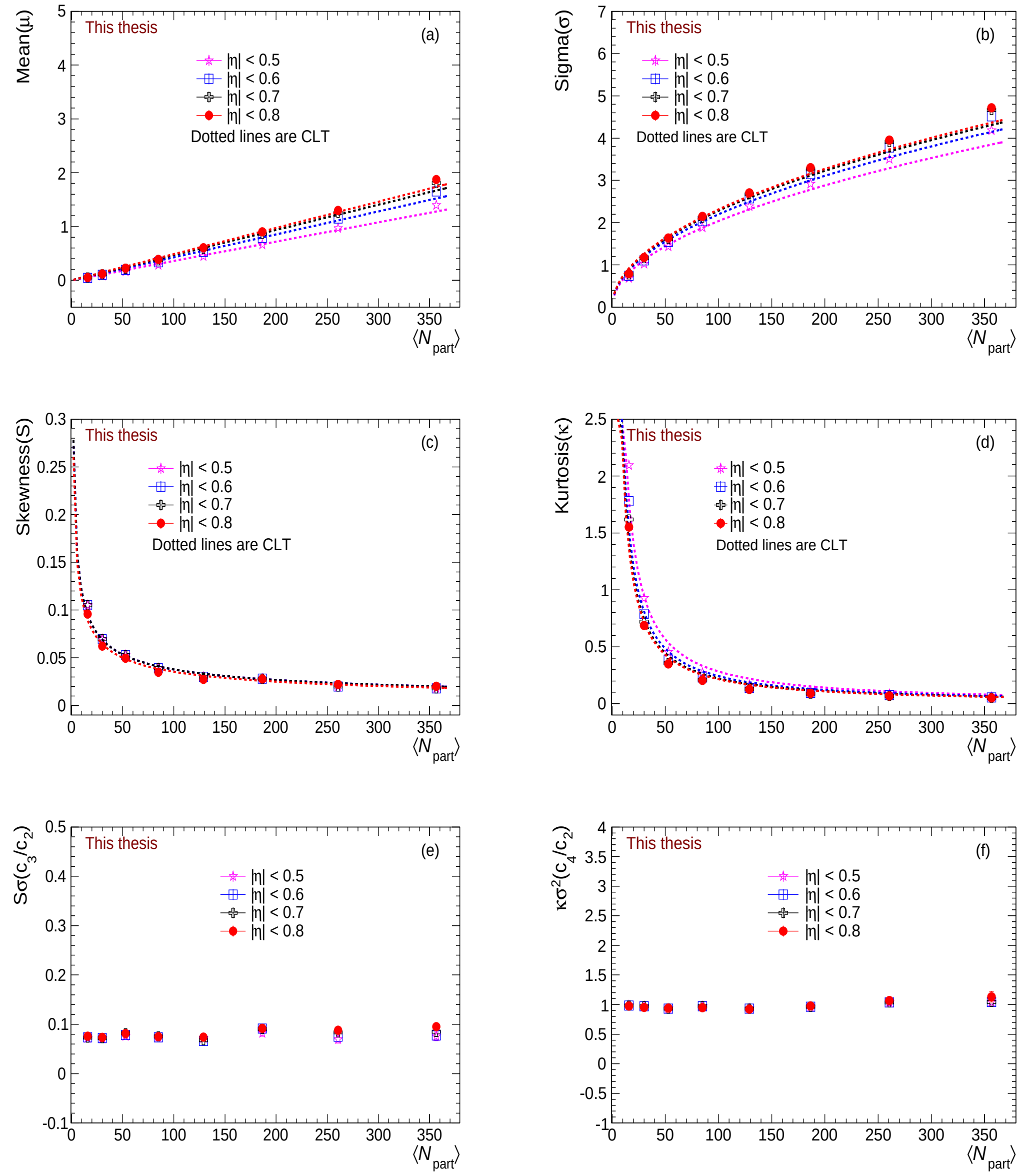

Figure 5.40: Pseudorapidity dependence of net-proton higher moments as a function of centrality.

Chapter 6

Summary and Future Prospective

6.1 Summary

In summary, one of the goal of heavy-ion collision experiment is to map the QCD phase diagram in T-μ_B plane and to characterize the phase transition of hadronic matter to QGP phase. Various experimental observables are proposed to study the matter produced in relativistic heavy-ion collisions. Many theoretical studies suggest that event-by-event measurement of $\langle p_T \rangle$ fluctuations, particle ratio fluctuations and specially fluctuation of conserved quantities, like net-charge, net-baryon, can be unique signatures of QGP. There are many theoretical predictions where it has been discussed that higher moments of conserved quantities, like net-charge, net-baryon distributions which will signal the location of the critical point in the QCD phase diagram. Moreover, study of higher moments of fluctuations of conserved quantities, like net-charge and net-proton at LHC can be used to quantify the freeze-out parameters and to put constraints on lattice QCD prediction to map the QCD phase diagram. This thesis work is carried out on the study of the higher moments of net-charge and net-proton number fluctuations in Pb+Pb collisions at $\sqrt{s_{NN}}$= 2.76 TeV in ALICE at LHC. ALICE is a versatile detector, which is built specially to investigate the QGP by studying the heavy-ion collision data.

In this analysis, the central moments and cumulants are evaluated which are always calculated with respect to the mean value. By invoking statistical mechanics and the lattice QCD, the relation between n^{th} order cumulants to n^{th} order generalized susceptibilities can be obtained as $c_n = VT^3\chi_q^{(n)}$. This is how it demonstrates that the moments and cumulants of conserved quantities, like net-charge, net-baryon (net-proton), which are experimentally measurable, can be connected with the lattice QCD observables. In lattice QCD, the freeze-out parameters are calculated by taking the ratio of various order of susceptibilities. This in turn, by taking the ratio of respective order cumulants, freeze-out parameters can be evaluated from experimental data. It is also shown that any deviation of the higher moments results from HRG model prediction can be used as a signal of critical fluctuations and chiral symmetry restoration. Before discussing about the results, the analysis methodologies, like Central Limit Theorem, Centrality Bin-Width Correction, statistical error estimation methods are discussed. The baseline estimation from Poissonian and NBD expectations are also discussed.

Because of limited statistics of MC data in ALICE, simulation studies are done using toy model. The toy model study is carried out to understand the effect of efficiency and statistics on the results of higher moments of net-charge and net-proton number distributions. It is observed from the toy model study that at low statistics, the results are oscillating in nature and with increase of statistics, the oscillating behavior of $S\sigma$ and $\kappa\sigma^2$ values are also approaching saturation over all the multiplicity classes. This toy model study suggests that for net-charge, at least on the order of 500×10^6 events and for net-proton, 100×10^6 events are required for each multiplicity bin for stable results with statistical uncertainties less than 10%. The effect of detector inefficiency is studied using the toy model for net-charge and net-proton. This study shows that, because of detector inefficiency, the results are affected. To correct the detector effect, event-wise and track-wise efficiency corrections were tried and found that none of them are able to remove the detector effects from the moments except mean of a reconstructed event. Then other two methods specially proposed to correct the detector efficiency to the higher moments are tried. The first method is the Unfolding method. Using toy model, it is tried and shown that it works only when a model used for the training whose multiplicity is same as the unfolding data can unfold back the moments results successfully. But if the training sample has different model than the data, then except mean and sigma, the other higher moments can't be unfolded back. In case of our study, the HIJING together with GEANT is used to model the detector effect. But HIJING doesn't explain the data well, so it can't be used for Unfolding method to correct the higher moments results. The second one, K-cumulant method is also tried with toy model both for net-charge and net-proton higher moments. This method also shows that except mean and sigma, other higher moments can't be corrected back. A drawback of this method is found that it uses the integrated detector efficiency over the whole phase space, however, the detector efficiency is dependent on p_T, η and ϕ of the tracks, which needs to be taken care of.

Then the analysis results of net-charge and net-proton are discussed. The minimum bias data of Pb+Pb collision of LHC10h AOD086 production version is used taking V0M as centrality estimator. The event selection, track selection etc, are discussed. For net-charge analysis, the tracks with p_T range from 0.3 to 1.5 GeV/c and within pseudorapidity coverage -0.8 to 0.8 are used. The raw results of mean, sigma, skewness and the products of moments, i.e. $S\sigma$ and $\kappa\sigma^2$, are presented as a function of $\langle N_{part} \rangle$. The data are fitted with CLT. Then the data are compared with HIJING and HIJING+GEANT results. Neither HIJING nor HIJING+GEANT can explain the data. The systematic study for six sources namely, two filterbits, two centrality estimators and positive and negative magnetic polarity are used. After systematic error estimation, the results are again plotted as a function of $\langle N_{part} \rangle$. The filterbits contribute maximum percentage for the systematic uncertainties. The reason is attributed to the efficiency uncorrected results of the filterbits. The Poissonian and NBD expectations also compared with the results. It is found that Poissonian expectation explains well the data within the statistical and systematic errors.

For net-proton analysis, the particle identification is done by using combined information of TPC and TOF. The particles with 0.5 GeV/c to 2.0 GeV/c and pseudorapidity coverage -0.8 to 0.8 are selected. The efficiency uncorrected results are shown as a function of $\langle N_{part} \rangle$ and fitted with CLT. The net-proton results are also compared with HIJING and HIJING+GEANT results. Neither HIJING nor HIJING+GEANT can explain the net-proton higher moments results. Then systematic uncertainties are estimated. The Poissonian and NBD expectation values are plotted together with the data. It is found that the data behave like Poissonian and the $\kappa\sigma^2$ value is almost one for all centralities. The pseudorapidity dependence of higher moments of net-charge and net-proton distributions are studied for four sets of pseudorapidity windows. It is observed that with increase of pseudorapidity coverage, the mean and sigma of the distributions increase. A comparison of data with HRG model and lattice QCD calculations are given in Table 6.1.

Table 6.1: Ratio of cumulants of data (0-5% centrality), HRG model and lattice QCD calculations for net-charge and net-proton number fluctuations. The theoretical values are taken from Ref. [80].

Ratio	**HRG**	**QCD:** $T^f/T_{pc} \leq 0.9$	**QCD:**$T^f/T_{pc} \simeq 1$	**Data**
χ_4^B/χ_2^B	1	≥ 1	~ 0.5	c_4/c_2 = 1.13±0.1±1.17 (Net-proton)
χ_4^Q/χ_2^Q	~ 2	≥ 2	~ 1	c_4^Q/c_2^Q = 1.84±3.4±5.8

The results of net-charge and net-proton higher moments are presented in this thesis without the correction of detector efficiency. The statistical and systematic uncertainties are very large. Therefore, no conclusion is drawn from the data at this point of time.

6.2 Future Prospective

This study of higher moments of conserved quantities, like net-charge and net-proton (baryon) numbers are very useful to quantify the freeze-out parameters at LHC. It will also help to constrain the Lattice QCD predictions and mapping the QCD phase diagram. So far the efficiency uncorrected results of net-charge and net-proton numbers are concerned, it is hard to say about the freeze-out parameters at this energy. In this study, there are two limitations: limited event statistics and lack of robust method to do efficiency correction to the data. The Pb+Pb collisions data of 2011 can be included to increase the event statistics to reduce the statistical uncertainties. There are few methods of efficiency correction to higher moments are under test. In future, results on this study will be certainly a crucial factor to map the QCD phase diagram and determination of the freeze-out parameters. There are also many theoretical predictions that flavor dependent higher moments will help to locate the freeze-out line at the vicinity of crossover line [135].

Bibliography

[1] David Griffiths, **“Introduction to Elementary Particles”**.

[2] F. Englert and R. Brout, **“Broken Symmetry and the Mass of the Gauge Vector Mesons”**, Phys. Rev. Lett. **13**, 321 (1964)

[3] P.W. Higgs, **“Broken Symmetries and the Mass of the Gauge Bosons”**, Phys. Rev. Lett. **13**, 508 (1964).

[4] M. Breidenbach et al. **“Observed Behavior of Highly Inelastic ElectronProton Scattering”**. Phys. Rev. Lett. **23**, 935 (1969).

[5] David J. Gross and Frank Wilczek, **“Ultraviolet Behavior of Non-Abelian Gauge Theories”**, Phys. Rev. Lett. **30**, 1343 (1973)

[6] H. D. Politzer, **“Reliable Perturbative Results for Strong Interactions?”**, Phys. Rev. Letters. **30**, 1346 (1973).

[7] I. J. R. Aitchison and A.J.G. Hey, **“Gauge theories in particle physics”**, Third Edition, Volume II, ISBN 0-7503-0950-4.

[8] Siegfried Bethke, **“Experimental Tests of Asymptotic Freedom”**, Prog. Part. Nucl. Phys. **58**, 351-386 (2007).

[9] Kenneth G. Wilson, **“Confinement of quarks”**, Phys. Rev. D. **10**, 2445 (1974).

[10] Rajan Gupta, **“Introduction to Lattice QCD”, Lectures given at the LXVIII Les Houches Summer School ”Probing the Standard Model of Particle Interactions”**, July 28-Sept 5, 1997. LAUR-98-3174, [arXiv:hep-lat/9807028].

[11] F. Karsch, E. Laermann and A. Peikert, **“The pressure in 2, 2+1 and 3 flavour QCD”**, Phys. Lett. B **478**, 447 (2000).

[12] C.P. Singh, **“Signals of QGP”**, Physics Report, (Review Section of Physics Letters) 236, No. 3 147-224 (1993).

[13] J. Rafelski, Nuclear Physics B Proceedings Supplement 00 18 (2013).

[14] http://www.phy.duke.edu/research/NPTheory/QGP/transport/index.php

[15] J. D. Bjorken, **“Highly relativistic nucleus-nucleus collisions: The central rapidity region”**, Phys. Rev. D **27**, 140151 (1983).

[16] V. N. Gribov and L. N. Lipatov, Sov. J. Nucl. Phys. **15**, 438 (1972).

[17] G. Altarelli and G. Parisi, **“Asymptotic freedom in parton language”**, Nucl. Phys. B **126**, 298 (1977).

[18] Yu. L. Dokshitzer, Sov. Phys. JETP **46**, 641 (1977).

[19] X. N. Wang and M. Gyulassy, **“Gluon shadowing and jet quenching in A+A collisions at $\sqrt{s}$=200A GeV”**, Phys. Rev. Lett. **68**, 1480 (1992).

[20] R. Baier, Yu. L. Dokshitzer, A. H. Mueller, S. Peigne, D. Schiff, **“Radiative energy loss of high energy quarks and gluons in a finite volume quark-gluon plasma”**, Nucl. Phys. B **483**, 291-320 (1997).

[21] B. G. Zakharov,**“Radiative energy loss of high energy quarks in finite-size nuclear matter and quark-gluon plasma”**, JETP Lett. **65**, 615-620 (1997).

[22] Yu. L. Dokshitzer, D. E. Kharzeev,**“Heavy-quark colorimetry of QCD matter”**, Phys. Lett. B **519**, 199 (2001).

[23] J. Adams et al. [STAR Collaboration], **“Evidence from d+Au Measurements for Final-State Suppression of High-p$_T$ Hadrons in Au+Au Collisions at RHIC ”**, Phys. Rev. Lett. **91**, 072304 (2003).

[24] B. B. Back et al. [PHOBOS Collaboration], **“Centrality Dependence of Charged-Hadron Transverse-Momentum Spectra in d+Au Collisions at $\sqrt{s_{NN}}$=200 GeV”**, Phys. Rev. Lett. **91**, 072302 (2003).

[25] S. S. Adler et al. [PHENIX Collaboration], **“Absence of Suppression in Particle Production at Large Transverse Momentum in $\sqrt{s_{NN}}$=200 GeV d+Au Collisions”**,Phys. Rev. Lett. **91**, 072303 (2003).

[26] I. Arsene et al. [BRAHMS Collaboration],**“Transverse-Momentum Spectra in Au+Au and d+Au Collisions at $\sqrt{s_{NN}}$=200 GeV and the Pseudorapidity Dependence of High-p$_T$ Suppression”**, Phys. Rev. Lett. **91**, 072305 (2003).

[27] Martin Spousta, **“Jet Quenching at LHC”**, Mod. Phys. Lett. A **28**, 22 (2013) .

[28] S. Voloshin and Y. Zhang, **“Flow study in relativistic nuclear collisions by Fourier expansion of Azimuthal particle distributions”**, Z. Phys. C **70**, 665, [hep-ph/9407282] (1996).

[29] P. Huovinen and P. Petreczky, **“QCD Equation of State and Hadron Resonance Gas,”**, Nucl. Phys. A **837**, 26 (2010).

[30] P. Kovtun, D. T. Son and A. O. Starinets,**“Viscosity in strongly interacting quantum field theories from black hole physics”**, Phys. Rev. Lett. **94**, 111601 (2005).

[31] J. Barrette et al, **“Proton and pion production relative to the reaction plane in Au + Au collisions at 11A GeV/c”**, Phys. Rev. C **56**, 32543264 (1997).

[32] T. Wienold, et al. [NA49 Collaboration], **“Stopping and collective effects at SPS energies”**, Nucl. Phys. A**610**, 76C-87C (1996).

[33] J. Adams et al. [STAR Collaboration], **“Azimuthal anisotropy in Au+Au collisions at $\sqrt{s_{NN}}$=200 GeV”**, Phys. Rev. C **72**, 014904 (2005).

[34] M. Gyulassy and L. McLerran, **“New forms of QCD matter discovered at RHIC”**, Nucl. Phys. A **750**, 30 (2005).

[35] R. Snellings, **“Elliptic Flow: A Brief Review”**, New J. Phys. **13**, 055008 (2011).

[36] T. Matsui and H. Satz, **“J/ψ Suppression by Quark-Gluon Plasma Formation”**, Phys. Lett. B **178**, 416 (1986).

[37] M. Gonin *et al.*, [NA50 Collaboration], **“Anomalous J/ψ suppression in Pb + Pb collisions at 158-A-GeV/c”**, Nucl. Phys. A **610**, 404C (1996).

[38] S. S. Adler *et al.* [PHENIX Collaboration], **“J/ψ production from proton proton collisions at $\sqrt{s}$ = 200 GeV”**, Phys. Rev. Lett. **92**, 051802 (2004).

[39] S. S. Adler *et al.* [PHENIX Collaboration], **“J/psi production and nuclear effects for d+Au and p+p collisions at $\sqrt{s}$ = 200-GeV”**, Phys. Rev. Lett. **96**, 012304 (2006).

[40] A. Adare *et al.* [PHENIX Collaboration], **“J/ψ Production vs Centrality, Transverse Momentum, and Rapidity in Au+Au Collisions at $\sqrt{s_{NN}} = 200$ GeV”**, Phys. Rev. Lett. **98**, 232301 (2007).

[41] A. Adare *et al.* [PHENIX Collaboration], **“Cold-nuclear-matter effcts on heavy-quark production in d+Au collisions at $\sqrt{s_{NN}} = 200$ GeV”**, Phys. Rev. Lett. **109**, 242301 (2012).

[42] P. Braun-Munzinger and J. Stachel, **“(Non)thermal aspects of charmonium production and a new look at J / psi suppression”**, Phys. Lett. B **490**, 196 (2000).

[43] R. L. Thews, M. Schroedter and J. Rafelski, **“Enhanced J/ψ production in deconfined quark matter”**, Phys. Rev. C **63**, 054905 (2001).

[44] B. B. Abelev *et al.* [ALICE Collaboration], **“Centrality, rapidity and transverse momentum dependence of J/ψ suppression in Pb-Pb collisions at $\sqrt{s_{NN}}$=2.76TeV”**, arXiv:1311.0214 [nucl-ex] (2013).

[45] F. Karsch, **“Lattice QCD at high temperature and density,”** Lect. Notes Phys. **583**, 209 (2002).

[46] V. Koch, **“Aspects of chiral symmetry”**, Int. J. Mod. Phys. E **6**, 203 (1997).

[47] R. Rapp and J. Wambach, **“Chiral symmetry restoration and dileptons in relativistic heavy ion collisions”**, Adv. Nucl. Phys. **25**, 1 (2000).

[48] L. L. Landau and E.M.. Lifshitz,Statistical Physics, Pergamon Press, (1958).

[49] S. A. Voloshin, V. Koch and H. G. Ritter, **“Event-by-event fluctuations in collective quantities”**, Phys. Rev. C **60**, 024901 (1999).

[50] S. Jeon and V. Koch, **“Charged particle ratio fluctuation as a signal for QGP”**, Phys. Rev. Lett. **85**, 2076 (2000).

[51] M. Asakawa, U. W. Heinz and B. Muller, **“Fluctuation probes of quark deconfinement”**, Phys. Rev. Lett. **85**, 2072 (2000).

[52] G. F. Smoot, **“Nobel Lecture: Cosmic microwave background radiation anisotropies: Their discovery and utilization,”** Rev. Mod. Phys. **79**, 1349 (2007).

[53] G. F. Smoot, C. L. Bennett, A. Kogut, E. L. Wright, J. Aymon, N. W. Boggess, E. S. Cheng and G. De Amici *et al.*, **“Structure in the COBE differential microwave radiometer first year maps”**, Astrophys. J. **396**, L1 (1992).

[54] D. N. Spergel *et al.* [WMAP Collaboration], **“Wilkinson Microwave Anisotropy Probe (WMAP) three year results: implications for cosmology,”** Astrophys. J. Suppl. **170**, 377 (2007).

[55] J. Adams *et al.* [STAR Collaboration], **“Experimental and theoretical challenges in the search for the quark gluon plasma: The STAR Collaboration’s critical assessment of the evidence from RHIC collisions,”** Nucl. Phys. A **757**, 102 (2005).

[56] N. Borghini and U. A. Wiedemann, **“Distorting the hump-backed plateau of jets with dense QCD matter,”** arXiv:hep-ph/0506218 (2005).

[57] T. Renk, **“Parton shower evolution in a 3-d hydrodynamical medium,”** Phys. Rev. C **78**, 034908 (2008).

[58] David dEnterria and Barbara Betz, **“Lecture notes in QGP, The Physics of the Quark-Gluon Plasma: Introductory Lectures,”**, Lect. Notes Phys. **785** (Springer, Berlin Heidelberg, DOI 10.1007/978-3-642-02286-9 (2010).

[59] A. D. Polosa and C. A. Salgado, **“Jet Shapes in Opaque Media,”** Phys. Rev. C **75**, 041901 (2007).

[60] J. Ruppert and B. Muller, **“Waking the colored plasma,”** Phys. Lett. B **618**, 123 (2005).

[61] S. Sapeta and U. A. Wiedemann, **“Jet hadrochemistry as a characteristics of jet quenching,”** Eur. Phys. J. C **55**, 293 (2008).

[62] R. J. Fries, B. Muller, C. Nonaka and S. A. Bass, **“Hadronization in heavy ion collisions: Recombination and fragmentation of partons,”** Phys. Rev. Lett. **90**, 202303 (2003).

[63] D. J. Kim [ALICE Collaboration], **“Particle Correlation Results from the ALICE Experiment at LHC,”** arXiv:1210.6172 [nucl-ex] (2012).

[64] S. Jeon and V. Koch, **“Event by event fluctuations,”** In *Hwa, R.C. (ed.) et al.: Quark gluon plasma* 430-490,[hep-ph/0304012] and reference therein (2003).

[65] M. A. Stephanov, K. Rajagopal and E. V. Shuryak, **“Event-by-event fluctuations in heavy ion collisions and the QCD critical point,”** Phys. Rev. D **60**, 114028 (1999).

[66] B. Abelev *et al.* [ALICE Collaboration], **“Net-Charge Fluctuations in Pb-Pb collisions at $\sqrt{s_{NN}}$ = 2.76 TeV,”** Phys. Rev. Lett. **110**, 152301 (2013).

[67] M. A. Stephanov, **“Non-Gaussian fluctuations near the QCD critical point,”**Phys. Rev. Lett. **102**, 032301 (2009).

[68] R. D. Pisarski and F. Wilczek, **“Remarks on the Chiral Phase Transition in Chromodynamics,”** Phys. Rev. D **29**, 338 (1984).

[69] F. Karsch, **“O(4) scaling, pseudo-critical temperatures and freeze-out in heavy ion collisions,”** AIP Conf. Proc. **1441**, 901 (2012).

[70] Y. Hatta and T. Ikeda, **"Universality, the QCD critical / tricritical point and the quark number susceptibility,"** Phys. Rev. D **67**, 014028 (2003).

[71] Z. Fodor and S. D. Katz, **"A New method to study lattice QCD at finite temperature and chemical potential,"** Phys. Lett. B **534**, 87 (2002).

[72] Y. Kim and D. Yi, **"Holography at Work for Nuclear and Hadron Physics"**, Review Article, Advances in High Energy Physics Volume 2011, Article ID 259025 (2011).

[73] S. Ejiri, C. R. Allton, S. J. Hands, O. Kaczmarek, F. Karsch, E. Laermann and C. Schmidt, **"Study of QCD thermodynamics at finite density by Taylor expansion,"** Prog. Theor. Phys. Suppl. **153**, 118 (2004).

[74] R. V. Gavai and S. Gupta, **"Pressure and nonlinear susceptibilities in QCD at finite chemical potentials,"** Phys. Rev. D **68**, 034506 (2003).

[75] C. R. Allton, S. Ejiri, S. J. Hands, O. Kaczmarek, F. Karsch, E. Laermann, C. Schmidt and L. Scorzato, **"The QCD thermal phase transition in the presence of a small chemical potential,"** Phys. Rev. D **66**, 074507 (2002).

[76] M. M. Aggarwal *et al.* [STAR Collaboration], **"Higher Moments of Net-proton Multiplicity Distributions at RHIC,"** Phys. Rev. Lett. **105**, 022302 (2010).

[77] A. Bazavov, H. T. Ding, P. Hegde, O. Kaczmarek, F. Karsch, E. Laermann, S. Mukherjee and P. Petreczky *et al.*, **"Freeze-out Conditions in Heavy Ion Collisions from QCD Thermodynamics,"** Phys. Rev. Lett. **109**, 192302 (2012).

[78] P. Braun-Munzinger, K. Redlich, J. Stachel, in Quark-Gluon Plasma, vol. 3, ed. by R.C. Hwa, X.N. Wang (World Scientific, Singapore), (2004).

[79] A. Andronic, P. Braun-Munzinger and J. Stachel, **"Thermal hadron production in relativistic nuclear collisions,"** Acta Phys. Polon. B **40**, 1005 (2009).

[80] B. Friman, F. Karsch, K. Redlich and V. Skokov, **"Fluctuations as probe of the QCD phase transition and freeze-out in heavy ion collisions at LHC and RHIC,"** Eur. Phys. J. C **71**, 1694 (2011).

[81] F. Karsch, **"Determination of Freeze-out Conditions from Lattice QCD Calculations,"** Central Eur. J. Phys. **10**, 1234 (2012).

[82] Armin Hermann et al. **"History of CERN:v1:Launching the European Organization for Nuclear Research"**, ISBN**0444870377**.

[83] Lyndon Evans and Philip Bryant, LHC Machine, JINST, vol. 3, p. S08001 (2008).

[84] J. P. Blewett, 200GeV intersecting storage accelerators,Proceeding of the 8th international Conference on High-Energy Accelerators, CERN, Geneva Switzerland (1971).

[85] H. J. Specht, **"Experimental aspects of heavy ion physics at LHC energies"**, Proceedings of European Committee for Future Accelerators(**https://cds.cern.ch/record/215298/files/CERN-90-10-V-2.pdf**).

[86] The Alice Collaboration, Alice Technical Design Report, JINST, vol-3 (2008), p. S08002(**http://iopscience.iop.org/1748-0221/3/08/S08002**).

[87] F. Carminati et al., ALICE: physics performance report, volume I, J. Phys. G **30**, 1517 (2004).

[88] Alice Technical Design Report on Time Projection Chamber, **https://edms.cern.ch/file/398930/1/ALICE-DOC-2003-011.pdf**.

[89] W.Blum, W. Riegler and L. Rolandi, Particle Detection with Drift Chambers, 2nd Edition. (Springer-Verlag, 2008).

[90] A. Andronic et al.**"Transition radiation spectra of electrons from 1 to 10 GeV/c in regular and irregular radiators"**, Nucl. Instrum. Meth. A **558**, 516 (2006).

[91] A. Andronic et al. **"Energy loss of pions and electrons 1-6 GeV/c in drift chambers operated with Xe,CO_2(15%)"**, Nucl. Instrum. Meth. A **519**, 508 (2006).

[92] ALICE collaboration, ALICE TRD Technical Design Report, CERN/LHCC 2001-021.

[93] ALICE collaboration, ALICE TOF Technical Design Report,CERN-LHCC-2000-012.

[94] ALICE collaboration, ALICE HMPID Technical Design Report, CERN-LHCC-98-19.

[95] ALICE collaboration, ALICE PHOS Technical Design Report, CERN-LHCC-99-4.

[96] ALICE collaboration, ALICE EMCAL Technical Design Report, CERN-LHCC-2008-014.

[97] ALICE collaboration, ALICE PMD Technical Design Report, CERN-LHCC-99-32, PMD ATDR, CERN-LHCC-2003-038.

[98] T. Sjostrand, S. Mrenna and P. Skands, PYTHIA 6.4 physics and manual, JHEP **05** 026 (2006).

[99] Xin-Nian Wang, Miklos Gyulassy, Phys. Rev. D **44**, 3501 (1991).

[100] M. Goossens et al. GEANT detector description and simulation tool,www.http://cds.cern.ch/record/1073159/files/cer-002728534.pdf.

[101] S. Agostinelli et al. GEANT4-a simulation toolkit, Nucl. Instrum. Meth. A **506**, 250-303 (2003).

[102] A. Ferrari, P. R. Sala, A. Fasso and J. Ranft, **"FLUKA: a multi-particle transport code",** CERN-2005-10 (2005), INFNTC0511, SLAC-R-773.

[103] http://mvpprograms.com/help/mvpstats/distributions/SkewnessKurtosis.

[104] A. K. Chaudhuri, **"A short course on Relativistic Heavy Ion Collisions"**, arXiv:1207.7028v1 (2012).

[105] Reviews on lattice QCD by S. R. Sharpe, http://pdg.lbl.gov/2012/reviews/rpp2012revlatticeqcd.pdf.

[106] Keson Huang, **Statistical Mechanics**, 2nd Edition, p152, by John Wiley and Sons Inc.

[107] F. Karsch and K. Redlich, **"Probing freeze-out conditions in heavy ion collisions with moments of charge fluctuations,"** Phys. Lett. B **695**, 136 (2011).

[108] P. Braun-Munzinger, D. Magestro, K. Redlich and J. Stachel, **"Hadron production in Au - Au collisions at RHIC,"** Phys. Lett. B **518**, 41 (2001).

[109] P. Huovinen and P. Petreczky, **"QCD Equation of State and Hadron Resonance Gas,"** Nucl. Phys. A **837**, 26 (2010).

[110] A. Bazavov *et al.* [HotQCD Collaboration], **"Fluctuations and Correlations of net baryon number, electric charge, and strangeness: A comparison of lattice QCD results with the hadron resonance gas model,"** Phys. Rev. D **86**, 034509 (2012).

[111] P. Braun-Munzinger, B. Friman, F. Karsch, K. Redlich and V. Skokov, **"Net-charge probability distributions in heavy ion collisions at chemical freeze-out,"** Nucl. Phys. A **880**, 48 (2012).

[112] T. J. Tarnowsky and G. D. Westfall, **"First Study of the Negative Binomial Distribution Applied to Higher Moments of Net-charge and Net-proton Multiplicity Distributions,"** Phys. Lett. B **724**, 51 (2013).

[113] X. -F. Luo [STAR Collaboration], **"Probing the QCD Critical Point with Higher Moments of Net-proton Multiplicity Distributions,"** J. Phys. Conf. Ser. **316**, 012003 (2011).

[114] X. F. Luo, B. Mohanty, H. G. Ritter and N. Xu, **"Energy Dependence of High Moments for Net-proton Distributions,"** J. Phys. G **37**, 094061 (2010).

[115] B. Efron, R. Tibshirani, **"An introduction to the bootstrap"**, Chapman & Hall (1993).

[116] X. Luo, **"Error Estimation for Moments Analysis in Heavy Ion Collision Experiment,"** J. Phys. G **39**, 025008 (2012).

[117] K. Aamodt *et al.* [ALICE Collaboration], **"Charged-particle multiplicity measurement in proton-proton collisions at $\sqrt{s} = 0.9$ and 2.36 TeV with ALICE at LHC"**, Eur. Phys. J. C **68**, 89 (2010).

[118] J. Jia [ATLAS Collaboration], **"Measurement of the distributions of event-by-event flow harmonics in Pb-Pb Collisions at $\sqrt{s_{NN}} = 2.76$ TeV with the ATLAS detector"**, Nucl. Phys. A**904-905** (2013), 421c (2013) [arXiv:1209.4232 [nucl-ex]].

[119] J. Jia and S. Mohapatra, **"Disentangling flow and nonflow correlations via Bayesian unfolding of the event-by-event distributions of harmonic coefficients in ultra-relativistic heavy-ion collisions"**, Phys. Rev. C **88**, no. 1, 014907 (2013).

[120] P. Garg et al., **"Unfolding of event-by-event net-charge distributions in heavy-ion collision"**, arXiv:1211.2074v1 [nucl-ex] 9 Nov 2012.

[121] G. D'Agostini, **"A multidimensional unfolding method based on Bayes theorem"**, Nuclear Instruments and Methods in Physics Research A **362** 487-498 (1995).

[122] http://hepunx.rl.ac.uk/ adye/software/unfold/RooUnfold.html

[123] Tim Adye, **“Unfolding algorithms and tests using RooUnfold”**, arXiv:1105.1160.

[124] Adam Bzdak, and Volker Koch, **“Acceptance corrections to net baryon and net charge cumulants”**, Phy. Rev. C **86**, 044904 (2012).

[125] Adam Bzdak, and Volker Koch, **“Local efficiency corrections to the higher order cumulants”**, arXiv:1312.4574v1.

[126] ALICE Internal Note ALICE-INT-2005-025, http://cdsweb.cern.ch/record/960438 .

[127] C. Loizides, **“Charged-particle multiplicity and transverse energy in Pb-Pb collisions at** $\sqrt{s_{NN}} = 2.76$ **TeV with ALICE”**, J. Phys. G **38**, 124040 (2011).

[128] B. Abelev *et al.* [ALICE Collaboration], **“Centrality determination of Pb-Pb collisions at** $\sqrt{s_{NN}}$ **= 2.76 TeV with ALICE”**, Phys. Rev. C **88**, 044909 (2013).

[129] ALICE TWIKI page on Hybrid Tracks https://twiki.cern.ch/twiki/bin/ viewauth/ALICE/HybridTracks.

[130] ALICE TWIKI page on AOD Filterbits https://twiki.cern.ch/twiki/bin/ view/ALICE/AddTaskInfoAOD086.

[131] K. Redlich, J. Cleymans, H. Oeschler and A. Tounsi, **“Conservation laws and particle production in heavy ion collisions,”** AIP Conf. Proc. **594**, 318 (2001).

[132] V. V. Begun, M. Gazdzicki, M. I. Gorenstein and O. S. Zozulya, **“Particle number fluctuations in canonical ensemble,”** Phys. Rev. C **70**, 034901 (2004).

[133] E. V Shuryak and M. A. Stephanov, Phys. Rev. C **63**, 064903 (2001).

[134] B. Abelev *et al.* [ALICE Collaboration], **“Pion, Kaon, and Proton Production in Central Pb–Pb Collisions at** $\sqrt{s_{NN}} = 2.76$ **TeV”**, Phys. Rev. Lett. **109**, 252301 (2012).

[135] R. Bellwied, S. Borsanyi, Z. Fodor, S. DKatz and C. Ratti, **“Is there a flavor hierarchy in the deconfinement transition of QCD?”**, Phys. Rev. Lett. **111**, 202302 (2013).

List of Publications

Publications:

- R. Sahoo, A. N. Mishra, **Nirbhay K. Behera**, B. K. Nandi, "Charged Particle and Photon Multiplicity, and Transverse Energy Production in High-Energy Heavy-Ion Collisions", To be published in Advances in High Energy Physics, arXiv:1408.5773.
- N. K. Behera, R. Sahoo and B. K. Nandi, "Constituent Quark Scaling of Strangeness Enhancement in Heavy-Ion Collisions," Adv. High Energy Phys. **2013**, 273248 (2013).
- H. Agakishiev *et al.* [STAR Collaboration], "Event-plane dependent dihadron correlations with harmonic v_n subtraction in Au+Au Collisions at $\sqrt{s_{\rm NN}} = 200$ GeV," arXiv:1404.1070 [nucl-ex].
- B. B. Abelev *et al.* [ALICE Collaboration], "Measurement of quarkonium production at forward rapidity in pp collisions at $\sqrt{s}$= 7 TeV," arXiv:1403.3648 [nucl-ex].
- B. B. Abelev *et al.* [ALICE Collaboration], "Production of charged pions, kaons and protons at large transverse momenta in pp and Pb-Pb collisions at $\sqrt{s_{NN}}$ = 2.76 TeV," arXiv:1401.1250 [nucl-ex].
- B. Abelev *et al.* [ALICE Collaboration], "Measurement of charged jet suppression in Pb-Pb collisions at $\sqrt{s_{NN}}$ = 2.76 TeV," JHEP **1403**, 013 (2014).
- B. B. Abelev *et al.* [ALICE Collaboration], "Two and Three-Pion Quantum Statistics Correlations in Pb-Pb Collisions at $\sqrt{s_{NN}}$ =2.76 TeV at the LHC," Phys. Rev. C **89**, 024911 (2014).
- B. B. Abelev *et al.* [ALICE Collaboration], "J/ψ production and nuclear effects in p-Pb collisions at $\sqrt{S_{NN}}$ = 5.02 TeV," JHEP **1402**, 073 (2014).
- B. B. Abelev *et al.* [ALICE Collaboration], "Multiplicity Dependence of Pion, Kaon, Proton and Lambda Production in p-Pb Collisions at $\sqrt{s_{NN}}$ = 5.02 TeV," Phys. Lett. B **728**, 25 (2014).
- B. B. Abelev *et al.* [ALICE Collaboration], "Multi-strange baryon production at mid-rapidity in Pb-Pb collisions at $\sqrt{s_{NN}}$ = 2.76 TeV," Phys. Lett. B **728**, 216 (2014).
- B. B. Abelev *et al.* [ALICE Collaboration], "K^0_S and Λ production in Pb-Pb collisions at $\sqrt{s_{NN}}$ = 2.76 TeV," Phys. Rev. Lett. **111**, 222301 (2013).

- B. B. Abelev *et al.* [ALICE Collaboration], "Long-range angular correlations of pi, K and p in p–Pb collisions at $\sqrt{s_{NN}}$ = 5.02 TeV," Phys. Lett. B **726**, 164 (2013).
- B. Abelev *et al.* [ALICE Collaboration], "Multiplicity dependence of two-particle azimuthal correlations in pp collisions at the LHC,"JHEP **1309**, 049 (2013).
- B. B. Abelev *et al.* [ALICE Collaboration], "Multiplicity dependence of the average transverse momentum in pp, p-Pb, and Pb-Pb collisions at the LHC," Phys. Lett. B **727**, 371 (2013).
- B. B. Abelev *et al.* [ALICE Collaboration], "Energy Dependence of the Transverse Momentum Distributions of Charged Particles in pp Collisions Measured by ALICE," Eur. Phys. J. C **73**, 2662 (2013).
- B. Abelev *et al.* [ALICE Collaboration], "Directed flow of charged particles at midrapidity relative to the spectator plane in Pb-Pb collisions at $\sqrt{s_{NN}}$=2.76 TeV," Phys. Rev. Lett. **111**, 232302 (2013).
- E. Abbas *et al.* [ALICE Collaboration], "Performance of the ALICE VZERO system," JINST **8**, P10016 (2013).
- B. Abelev *et al.* [ALICE Collaboration], "D meson elliptic flow in non-central Pb-Pb collisions at $\sqrt{s_{NN}} = 2.76$TeV," Phys. Rev. Lett. **111**, 102301 (2013).
- E. Abbas *et al.* [ALICE Collaboration], "Mid-rapidity anti-baryon to baryon ratios in pp collisions at $\sqrt{s}$ = 0.9, 2.76 and 7 TeV measured by ALICE," Eur. Phys. J. C **73**, 2496 (2013).
- E. Abbas *et al.* [ALICE Collaboration], "Charmonium and e^+e^- pair photoproduction at mid-rapidity in ultra-peripheral Pb-Pb collisions at $\sqrt{s_{NN}}$ = 2.76 TeV," Eur. Phys. J. C **73**, 2617 (2013).
- E. Abbas *et al.* [ALICE Collaboration], "Centrality dependence of the pseudorapidity density distribution for charged particles in Pb-Pb collisions at $\sqrt{s_{NN}}$ = 2.76 TeV," Phys. Lett. B **726**, 610 (2013).
- E. Abbas *et al.* [ALICE Collaboration], "J/Psi Elliptic Flow in Pb-Pb Collisions at $\sqrt{s_{NN}}$ = 2.76 TeV," Phys. Rev. Lett. **111**, 162301 (2013).
- B. Abelev *et al.* [ALICE Collaboration], "Centrality dependence of π, K, p production in Pb-Pb collisions at $\sqrt{s_{NN}}$ = 2.76 TeV," Phys. Rev. C **88**, 044910 (2013).
- B. Abelev *et al.* [ALICE Collaboration], "Centrality determination of Pb-Pb collisions at $\sqrt{s_{NN}}$ = 2.76 TeV with ALICE," Phys. Rev. C **88**, 044909 (2013).
- B. Abelev *et al.* [ALICE Collaboration], "Charge correlations using the balance function in Pb-Pb collisions at $\sqrt{s_{NN}}$ = 2.76 TeV," Phys. Lett. B **723**, 267 (2013).

- B. Abelev *et al.* [ALICE Collaboration], "Measurement of the inclusive differential jet cross section in pp collisions at $\sqrt{s} = 2.76$ TeV," Phys. Lett. B **722**, 262 (2013).
- B. Abelev *et al.* [ALICE Collaboration], "Charged kaon femtoscopic correlations in pp collisions at $\sqrt{s} = 7$ TeV," Phys. Rev. D **87**, no. 5, 052016 (2013).
- B. Abelev *et al.* [ALICE Collaboration], "Long-range angular correlations on the near and away side in p-Pb collisions at $\sqrt{s_{NN}} = 5.02$ TeV," Phys. Lett. B **719**, 29 (2013).
- B. Abelev *et al.* [ALICE Collaboration], "Transverse Momentum Distribution and Nuclear Modification Factor of Charged Particles in p-Pb Collisions at $\sqrt{s_{NN}} = 5.02$ TeV," Phys. Rev. Lett. **110**, 082302 (2013)
- B. Abelev *et al.* [ALICE Collaboration], "Pseudorapidity density of charged particles p-Pb collisions at $\sqrt{s_{NN}} = 5.02$ TeV," Phys. Rev. Lett. **110**, 032301 (2013).
- B. Abelev *et al.* [ALICE Collaboration], "Coherent J/ψ photoproduction in ultra-peripheral Pb-Pb collisions at $\sqrt{s_{NN}} = 2.76$ TeV," Phys. Lett. B **718**, 1273 (2013).
- B. Abelev *et al.* [ALICE Collaboration], "Production of $K^{*}(892)^{0}$ and $\phi(1020)$ in pp collisions at $\sqrt{s} = 7$ TeV," Eur. Phys. J. C **72**, 2183 (2012).
- B. Abelev *et al.* [ALICE Collaboration], "Measurement of inelastic, single- and double-diffraction cross sections in proton–proton collisions at the LHC with ALICE," Eur. Phys. J. C **73**, 2456 (2013).
- B. Abelev *et al.* [ALICE Collaboration], "Centrality Dependence of Charged Particle Production at Large Transverse Momentum in Pb–Pb Collisions at $\sqrt{s_{\rm NN}} = 2.76$ TeV," Phys. Lett. B **720**, 52 (2013).
- B. Abelev *et al.* [ALICE Collaboration], "Pion, Kaon, and Proton Production in Central Pb–Pb Collisions at $\sqrt{s_{NN}} = 2.76$ TeV," Phys. Rev. Lett. **109**, 252301 (2012).
- B. Abelev *et al.* [ALICE Collaboration], "D_s^+ meson production at central rapidity in proton–proton collisions at $\sqrt{s} = 7$ TeV," Phys. Lett. B **718**, 279 (2012).
- B. Abelev *et al.* [ALICE Collaboration], "Measurement of electrons from beauty hadron decays in pp collisions at $\sqrt{s} = 7$ TeV," Phys. Lett. B **721**, 13 (2013).
- B. Abelev *et al.* [ALICE Collaboration], "Net-Charge Fluctuations in Pb-Pb collisions at $\sqrt{s}_{NN} = 2.76$ TeV," Phys. Rev. Lett. **110**, no. 15, 152301 (2013).
- B. Abelev *et al.* [ALICE Collaboration], "Charge separation relative to the reaction plane in Pb-Pb collisions at $\sqrt{s_{NN}} = 2.76$ TeV," Phys. Rev. Lett. **110**, 012301 (2013).

- B. Abelev *et al.* [ALICE Collaboration], "$K_s^0 - K_s^0$ correlations in pp collisions at $\sqrt{s} = 7$ TeV from the LHC ALICE experiment," Phys. Lett. B **717**, 151 (2012).
- B. Abelev *et al.* [ALICE Collaboration], "Production of muons from heavy flavour decays at forward rapidity in pp and Pb-Pb collisions at $\sqrt{s_{NN}}$ = 2.76 TeV," Phys. Rev. Lett. **109**, 112301 (2012).
- B. Abelev *et al.* [ALICE Collaboration], "Measurement of prompt J/ψ and beauty hadron production cross sections at mid-rapidity in pp collisions at $\sqrt{s} = 7$ TeV," JHEP **1211**, 065 (2012).
- B. Abelev *et al.* [ALICE Collaboration], "Anisotropic flow of charged hadrons, pions and (anti-)protons measured at high transverse momentum in Pb-Pb collisions at $\sqrt{s_{NN}}$=2.76 TeV," Phys. Lett. B **719**, 18 (2013).
- B. Abelev *et al.* [ALICE Collaboration], "Measurement of electrons from semileptonic heavy-flavour hadron decays in pp collisions at $\sqrt{s} = 7$ TeV," Phys. Rev. D **86** (2012) 112007.
- B. Abelev *et al.* [ALICE Collaboration], "Measurement of charm production at central rapidity in proton-proton collisions at $\sqrt{s} = 2.76$ TeV," JHEP **1207**, 191 (2012).
- B. Abelev *et al.* [ALICE Collaboration], "Transverse sphericity of primary charged particles in minimum bias proton-proton collisions at $\sqrt{s} = 0.9$, 2.76 and 7 TeV," Eur. Phys. J. C **72**, 2124 (2012).
- B. Abelev *et al.* [ALICE Collaboration], "Multi-strange baryon production in pp collisions at $\sqrt{s}$ = 7 TeV with ALICE," Phys. Lett. B **712**, 309 (2012).
- G. Agakishiev *et al.* [STAR Collaboration], "Energy and system-size dependence of two- and four-particle v_2 measurements in heavy-ion collisions at RHIC and their implications on flow fluctuations and nonflow," Phys. Rev. C **86**, 014904 (2012).
- G. Agakishiev *et al.* [STAR Collaboration], "Directed and elliptic flow of charged particles in Cu+Cu collisions at $\sqrt{s_{NN}} = 22.4$ GeV," Phys. Rev. C **85**, 014901 (2012).
- G. Agakishiev *et al.* [STAR Collaboration], "Anomalous centrality evolution of two-particle angular correlations from Au-Au collisions at $\sqrt{s_{\rm NN}}$ = 62 and 200 GeV," Phys. Rev. C **86**, 064902 (2012).
- G. Agakishiev *et al.* [STAR Collaboration], "ρ^0 Photoproduction in AuAu Collisions at $\sqrt{s_{NN}}$=62.4 GeV with STAR," Phys. Rev. C **85**, 014910 (2012).
- G. Agakishiev *et al.* [STAR Collaboration], "Strangeness Enhancement in Cu+Cu and Au+Au Collisions at $\sqrt{s_{NN}} = 200$ GeV," Phys. Rev. Lett. **108**, 072301 (2012).

- H. Agakishiev *et al.* [STAR Collaboration], "Evolution of the differential transverse momentum correlation function with centrality in Au+Au collisions at $\sqrt{s_{NN}} = 200$ GeV," Phys. Lett. B **704**, 467 (2011).
- H. Agakishiev *et al.* [STAR Collaboration], "Observation of the antimatter helium-4 nucleus," Nature **473**, 353 (2011).
- H. Agakishiev *et al.* [STAR Collaboration], "High p_T non-photonic electron production in $p + p$ collisions at $\sqrt{s} = 200$ GeV," Phys. Rev. D **83**, 052006 (2011).
- H. Agakishiev *et al.* [STAR Collaboration], "Studies of di-jet survival and surface emission bias in Au+Au collisions via angular correlations with respect to back-to-back leading hadrons," Phys. Rev. C **83**, 061901 (2011).
- H. Agakishiev *et al.* [STAR Collaboration], "Measurements of Dihadron Correlations Relative to the Event Plane in Au+Au Collisions at $\sqrt{s_{NN}} = 200$ GeV," arXiv:1010.0690 [nucl-ex].

Publication in proceedings:

- Proceedings on "Constituents quarks and enhancement of multi-strange baryons in heavy-ion collisions" Nuclear Physics symposium On Nuclear Phys. **56** (2011) 1012
- Proceedings on "Constituents quarks and multi-strange baryon production in heavy-ion collisions" in International symposium on Nuclear Phys. **54** (2009) 594

Acknowledgements

This journey of six and half years was an exciting and important period of my life. I evolved, I learned, I succeeded in many ways during this period. At this moment, I would like to take an opportunity to thank all of you whose blessing are always with me and made me successful in my PhD career.

First and foremost, I would like to express my gratitude and thanks to my thesis supervisor Prof. Basanta Kumar Nandi, for his sincere guidance and support. I can never forget his constant effort and encouragement to pursue my dream as PhD scholar and helping me developing skill of being an experimentalist and as a researcher. He has inspired me in all ways of my PhD career, broadened my vision and enlightened me on philosophy towards life. Not only in academic life, but also in social life he is always my *Guru* to guide me at each and every step during the stay in IIT Bombay. His friendly manner has helped me to smile, strengthen me to stand tall at every odd moment of life. He is not only my supervisor, but also a teacher, a guardian, a friend for me. In fact I have no words to express his role being my supervisor. Sir, I am grateful to you and I feel graced being a student of you.

I would like to thank Prof. Raghava Varma, for his invaluable advice, his encouragement and help during my PhD. He has motivated and inspired me for hard work and to make my country proud. He is like a guide and mentor for me. I would like to express my gratitude for his constant support and providing me all possible opportunities during my PhD career.

I would also like to thank Prof. Sadhana Dash for her support and providing constructive criticism during my PhD work. Her valuable suggestions and many scientific discussions have helped me to broaden my knowledge on QGP physics.

Being a part of PMD collaboration, I would like to extend my thanks to Dr. Y. P. Viyogi for his advice, constructive criticism, help and support. He will always be an inspiration for me. I would also like to thank Dr. Tapan Nayak for his constant supervision and encouragement during my thesis work. I would also like to express my thanks to other PMD collaborators at IOP Bhubaneswar, Jammu University, Panjab University, Rajasthan University and VECC Kolkata for their supports during my PhD work.

It was really a great opportunity for me to work with Dr. Nu Xu of LBL, Lijuan Ruan of BNL and Frank Geurts of Rice University during my simulation work for Time Of Flight detector. I would also like to thank Michael Weber, CERN for some useful discussion during my thesis work in ALICE.

I would also like to take an opportunity to extend my thanks to my seniors Dr. Bedanga Mohanty, Prof. Raghunath Sahoo, Dr. Dipak Mishara and Prof. Anki Roy for their support and love.

During my stay at IIT Bombay, wonderful lab-mates and friends had accompanied me. I am thankful to Dr. Prabhat Pujahari, Dr. Satyajit Jena and Dr. Ajay Nayak who are like my elder brother and Friend. I would also like to thank Dr. Neha Saha, Dr. Kavita Lalwani, Dr. Himani Bhatt for their help and good wishes. I am also thankful to Anitha, Roshnee, Reetanjali, Amal, Greshma, Sidesh, Manoj, Jitendra, Asuthosh, Shyam, Divhash, Neelima, Bharati for their love, help and good wishes. I would also thank to all my M.Sc. friends for their support and love.

Last but not the least I would like to express my gratitude and respect to my parent for their support and blessings. It is because of them whatever I am today. Indeed, I am short of words to express my love and thanks for their immense love, patience and encouragement. I would also like to thank my wife Shradhanjali for her constant moral support and affection at every step of my PhD life to complete this work. I would like to say that it is only because of my family for which I could make this. My parent are living God for me. Heartiest thanks to them and pray to God for the welfare of everybody.